

2023-08

# Manufacture, Refinement and Low-Speed Flight Testing of a Small-Scale, High-Speed Uncrewed Aerial Vehicle

Gair, Shaun Robert

---

Gair, S. R. (2023). Manufacture, refinement and low-speed flight testing of a small-scale, high-speed uncrewed aerial vehicle (Master's thesis, University of Calgary, Calgary, Canada). Retrieved from <https://prism.ucalgary.ca>.

<https://hdl.handle.net/1880/116863>

*Downloaded from PRISM Repository, University of Calgary*

UNIVERSITY OF CALGARY

Manufacture, Refinement and Low-Speed Flight Testing of a Small-Scale, High-Speed Uncrewed  
Aerial Vehicle

by

Shaun Robert Gair

A THESIS

SUBMITTED TO THE FACULTY OF GRADUATE STUDIES  
IN PARTIAL FULFILLMENT OF THE REQUIREMENTS FOR THE  
DEGREE OF MASTER OF SCIENCE

GRADUATE PROGRAM IN MECHANICAL ENGINEERING

CALGARY, ALBERTA

AUGUST, 2023

© Shaun Robert Gair 2023

# Abstract

This thesis details the mechanical design, manufacture, and flight testing of a sub-2.5kg UAV prototype. While the aircraft configuration is designed for supersonic flight, the goal of this work is to evaluate the low-speed flight characteristics and to prove positive stability and control at low speeds. Low-speed testing will evaluate the applicability of established design techniques—developed for full-scale, crewed aircraft—to small-scale, high-speed UAVs. Review of literature and preliminary results led to a focus on the prediction of lateral stability characteristics, especially vertical tail volume coefficient (VTVC). Flight testing of the prototype did not yield sustained flight; however, data collected during takeoff attempts provide valuable information about the behaviour of the design. These data indicate that the aircraft was laterally unstable, contradicting the vertical tail design determined from VTVC sizing methods. Analysis of VTVC for existing tailless delta-winged aircraft and comparison with the MUFASA aircraft showed that VTVC is insufficient as an early design parameter for small-scale, high-speed designs. A novel parameter, the fuselage-normalized tail volume coefficient, is proposed for use in conjunction with the conventional VTVC. Taken together, these two parameters provide a more complete prediction of lateral stability for small UAVs with supersonic design configurations. Future development work on this project could benefit from a detailed lateral stability study, thorough engine intake design, and improvements to the launch rail used to accelerate the aircraft.

# Preface

Portions of this work are published in the AIAA Aviation conference (Durante et al., 2022).



# Acknowledgements

As the adage goes, it takes a village. The only name on this thesis is my own, but that does not reflect the vital contributions of those around me.

Without my incessantly patient, thoughtful, and clever wife I would never have found the mental strength and strategies to persevere through this marathon task. She understands me far better than I understand myself, her sharing of that knowledge has allowed me to grow in ways I didn't know I could.

The importance of my parents' unwavering support and caring is impossible to overstate. The knowledge that they are on my team provided me the security of knowing that failure need not be catastrophic, and the confidence to push through.

I've had the privilege of sharing the lab with a group of wonderful colleagues with diverse experience. We've learned and grown together, and without collaboration none of us would be where we are now.

Finally, a special thank-you must go to my supervisors, Dr. Chris Morton and Dr. Craig Johansen. They provided the opportunity to work on this project and their depth of experience provided me the tools to succeed.

# Table of Contents

<b>Abstract</b>	<b>ii</b>
<b>Preface</b>	<b>iii</b>
<b>Acknowledgements</b>	<b>iv</b>
<b>Table of Contents</b>	<b>v</b>
<b>List of Figures and Illustrations</b>	<b>vii</b>
<b>List of Tables</b>	<b>ix</b>
<b>List of Symbols, Abbreviations and Nomenclature</b>	<b>x</b>
<b>Epigraph</b>	<b>xii</b>
<b>1 Introduction</b>	<b>1</b>
1.1 The MUFASA Project . . . . .	3
<b>2 Literature Review</b>	<b>7</b>
2.1 Existing High-Speed UAV Projects . . . . .	8
2.2 SSUAV Technical Challenges . . . . .	13
2.2.1 Delta-winged Aircraft . . . . .	13
2.2.2 Small-Scale Effects . . . . .	18
<b>3 Aircraft Design &amp; Construction</b>	<b>21</b>
3.1 Aircraft Control Characteristics . . . . .	25
3.1.1 Pitch Stability . . . . .	25
3.1.2 Calculation of Mean Aerodynamic Chord . . . . .	27
3.1.3 Lateral Stability . . . . .	29
3.1.4 Elevon Sizing . . . . .	32
3.2 Intake Sizing . . . . .	32
3.3 Construction Method . . . . .	34
3.3.1 Division into Structural Elements . . . . .	39
3.3.2 Thin Sections . . . . .	43
3.3.3 3D Printed Components . . . . .	44

3.4	Version 2 Design Refinements . . . . .	45
<b>4</b>	<b>Ground Testing &amp; Results</b>	<b>48</b>
4.1	Electronics Function Checks . . . . .	48
4.2	Engine Thrust Testing . . . . .	49
4.3	Discussion . . . . .	53
<b>5</b>	<b>Flight Testing &amp; Results</b>	<b>56</b>
5.1	Flight Test Plan . . . . .	56
5.1.1	Pre-flight Checks . . . . .	58
5.1.2	Weather Conditions for Flight . . . . .	60
5.2	MUFASA A.1 V1 . . . . .	61
5.2.1	V1 Flight Descriptions . . . . .	62
5.2.2	V1 Flight Data . . . . .	64
5.3	MUFASA A.1 V2 . . . . .	69
5.3.1	V2 Flight Descriptions . . . . .	70
5.3.2	V2 Flight Data . . . . .	72
5.4	Discussion . . . . .	79
5.4.1	Takeoff Speed . . . . .	79
5.4.2	Takeoff Attitude . . . . .	81
5.4.3	Lateral Stability & Vertical Tail Volume Coefficients . . . . .	86
<b>6</b>	<b>Conclusions &amp; Recommendations</b>	<b>92</b>
6.1	Recommendations & Future Work . . . . .	93
6.1.1	Flight Testing Improvements . . . . .	93
6.1.2	Aircraft Improvements . . . . .	94
	<b>Bibliography</b>	<b>95</b>
<b>A</b>	<b>Launch Rail - Description &amp; Operation</b>	<b>117</b>
A.1	Validation Testing . . . . .	121

# List of Figures and Illustrations

1.1	CAD image of the initial aerodynamic shape under consideration. . . . .	6
2.1	SSUAV concepts (not to scale). . . . .	9
2.2	CAD model (top) and Schlieren image (bottom) of the Ohwashi M2011 configuration with narrowed fuselage taken at Mach 1.1, adapted from Yamazaki et al. (2019) . . . . .	10
2.3	Pohox configuration drawing, adapted from Magn and Barbosa (2013). . . . .	11
2.4	Various R-UAV models constructed and tested at the University of Washington, adapted from Nelson et al. (2022). . . . .	13
2.5	Illustration of delta wing vortices critical in lift generation, from Hoerner (1985). .	14
2.6	Experimentally-determined lift curves for delta wings of various aspect ratios, $Re \approx 7 \times 10^5$ , from Truckenbrodt (1954). . . . .	15
3.1	MUFASA A.1 V1 planform and general layout with key dimensions in millimetres.	22
3.2	Side view of MUFASA A.1 showing target CG location and aerodynamic centre for approximately 15% static margin. . . . .	27
3.3	Diagram and equations necessary for MAC calculation of a double-delta planform. Diagram and equations from Gudmundsson (2022b) . . . . .	28
3.4	Historical aileron sizing guidelines, adapted from Raymer (2018). . . . .	33
3.5	Detail of EPS foam machined surface finish and factory surface finish. Contrast enhanced to highlight bead boundaries. . . . .	36
3.6	Post-failure image of bond strength test between EPS foam to 3D printed PETG. .	37
3.7	Exploded view of airframe components. All parts shown are EPS foam except where noted. . . . .	41
3.8	Fuselage and wing components of the Skywalker X8 commercial UAV, showing the wing attachment spars running directly through the fuselage. Image from Spex-Drone (2023) . . . . .	42
3.9	Airframe structure consisting of individually machined EPS foam components and 3D printed trailing edge caps in green and red. . . . .	44
3.10	Comparison of V1 and V2 wing planforms . . . . .	47
4.1	Image of static thrust test setup. . . . .	51
4.2	Video frame from thrust testing using string angular deflection. . . . .	52
4.3	Static thrust test curves for MUFASA A.1 V1, EDF as installed in airframe, 83 mm inlet. . . . .	53

5.1	Photo of V1 airframe before flight testing. . . . .	63
5.2	Photo of V1 airframe condition after flight 1. . . . .	63
5.3	Photo of V1 airframe condition after flight 2. . . . .	64
5.6	Aircraft trajectory during flight V1F1. . . . .	66
5.7	Aircraft trajectory during flight V1F2. . . . .	66
5.4	Analysis of various parameters on takeoff, flight V1-F1. . . . .	67
5.5	Analysis of various parameters on takeoff, flight V1-F2. . . . .	68
5.8	Photo of V2 airframe after repairs from first flight. . . . .	70
5.9	Photo of damage to V2 wing tip after flight 2. . . . .	71
5.10	Photo of damage to V2 wing tip after flight 2. . . . .	72
5.11	Aircraft trajectory during flight V2F1. . . . .	74
5.12	Aircraft trajectory during flight V2F2. . . . .	74
5.13	Aircraft trajectory during flight V2F3. . . . .	75
5.14	Analysis of various parameters on takeoff, flight V2-F1. . . . .	76
5.15	Analysis of various parameters on takeoff, flight V2-F2. . . . .	77
5.16	Analysis of various parameters on takeoff, flight V2-F3. . . . .	78
5.17	Lift curves of a NACA 6-series airfoil with sealed plain flap. Adapted from Roskam and Lan (1997). . . . .	82
5.18	Velocity, heading, and wind direction vectors for V2F2 immediately after takeoff. Corresponding roll angle of $+8.6^\circ$ (right wing down). . . . .	83
5.19	Velocity, heading, and wind direction vectors for V2F2 as the velocity direction and nose heading pass through alignment. Corresponding roll angle of $-13.0^\circ$ (left wing down). . . . .	84
5.20	Velocity, heading, and wind direction vectors for V2F2 at moment of maximum yaw rate to the left. Corresponding roll angle of $-46.0^\circ$ (left wing down). . . . .	85
5.21	Calculated conventional tail volume coefficients based on (Eq. (3.7)). . . . .	87
5.22	Calculated fuselage-normalized tail volume coefficients based on Eq. (5.1)). . . . .	88
5.23	Illustration of chined forebody effects on crossflow for the SR-71, adapted from Rich (1974). . . . .	90
5.24	Geometric mean of conventional and fuselage-normalized tail volume coefficients for various tailless delta aircraft. . . . .	91
A.1	Launch cradle with airframe resting on yokes. . . . .	119
A.2	Bare launch cradle with yokes folded down (after-takeoff condition). . . . .	119
A.3	Diagram of launch rail configuration. . . . .	120
A.4	Video frames from a launch rail test. . . . .	122

# List of Tables

1.1	MUFASA project aircraft versioning scheme. The focus of the present work is highlighted in bold. . . . .	4
2.1	List of existing SSUAV projects and some key parameters. Date ranges are taken from the dates of published works. . . . .	8
3.1	Explanation of NACA 64(0.3)08 a=0.5 airfoil used for MUFASA A.1 . . . . .	24
3.2	Calculation parameters for MAC of MUFASA A.1 . . . . .	29
3.3	Calculation parameters for vertical tail volume coefficient of MUFASA A.1 . . . .	30
3.4	Suggested vertical tail volume coefficients from various authors. Table adapted from Barua et al. (2013) . . . . .	31
3.5	Mass of manufactured airframe components . . . . .	39
3.6	Summary of changes to MUFASA A.1 from V1 to V2. . . . .	47
4.1	Measured static thrust for EDF installed in flight configuration. . . . .	53
4.2	Measured static thrust for small and large intakes compared with manufacturer data. . . . .	55
5.1	Summary of flight computer parameters collected for further analysis. . . . .	57
5.2	Summary of flight computer parameters collected for further analysis. . . . .	59
5.3	Summary of Flight Conditions - MUFASA A.1 V1 Test Flights. . . . .	62
5.4	Summary of Flight Conditions - MUFASA A.1 V2 Test Flights. . . . .	69

# List of Symbols, Abbreviations and Nomenclature

Symbol	Definition
$b$	Wingspan
$c$	Chord
$l$	Length or moment arm
$S$	Surface area
$\bar{X}$	Longitudinal location, measured from nose
$\bar{Y}$	Spanwise location, measured from centreline

Subscript	Definition
$b$	Discontinuity (chord)
$cg$	Centre of gravity
$MAC$	Mean aerodynamic chord
$np$	Neutral point
$r$	Reference (chord)
$t$	Tip (chord)
$VT$	Vertical tail

Abbreviation	Definition
AC	Aerodynamic Centre
AGL	Above Ground Level
AoA	Angle Of Attack, $\alpha$
ARL	Atlantis Research Labs
AUW	All Up Weight
CG	Centre of Gravity
CFD	Computational Fluid Dynamics
CNC	Computer Numeric Control
DOF	Degrees of Freedom
EKF	Extended Kalman Filter
EPS	Expanded Polystyrene
ESC	Electronic Speed Controller
FFF	Fused-Filament Fabrication
HDOP	Horizontal Dilution of Precision

IMU	Inertial Measurement Unit
JAXA	Japan Aerospace Exploration Agency
LiPo	Lithium Polymer
MAC	Mean Aerodynamic Chord
MGC	Mean Geometric Chord
MUFASA	Multipurpose Uncrewed Fixed-wing Advanced Supersonic Aircraft
PETG	Polyethylene Terephthalate-Glycol
PWM	Pulse Width Modulation
SM	Static Margin
SSUAV	Small-scale Supersonic Uncrewed Aerial Vehicle
VTVC	Vertical Tail Volume Coefficient
TVC	Tail Volume Coefficient
UAV	Uncrewed Aerial Vehicle
UAS	Unmanned/Uncrewed Aircraft System
VOCs	Volatile Organic Compounds
RWD	Right Wing Down
LWD	Left Wing Down



# Epigraph

*Takeoffs are optional, but all landings are mandatory.*

- Unknown

# Chapter 1

## Introduction

Ever since the first successful attempts at flight in the early 1900s, engineers and dreamers have pushed the boundaries of speed and altitude. Whether to fulfill a military or scientific mission, or simply because they could, incredible feats of engineering working towards human flight have expanded our knowledge of materials, fluid dynamics, and countless other areas of research (Anderson, 2002). Whether humans as of the 21st century have “mastered” flight is difficult to say with certainty, but the ubiquity of modern air jet transports and their impressive safety records are strong arguments in favour. The next significant challenge it seems is to bring a return to supersonic civil transport in an economically viable way with acceptable environmental impact (Candel, 2004; Weit et al., 2021). To that end, research into low sonic boom technology (Alonso and Colonno, 2012; Maglieri et al., 2014), environmentally sustainable fuels (Blakey et al., 2011; Holladay et al., 2020), and design feasibility (Henne, 2005; Sun and Smith, 2017) has accelerated in recent years. Despite recent advances, the development and production of any commercial aircraft is an extremely costly enterprise, even for the relatively mature commercial jet market (Altfeld, 2016; Rodrigue, 2020). In 2001 Boeing is quoted as stating that the total cost to develop the 777 jetliner approached \$12 billion USD (Altfeld, 2016). The Airbus A380 and Boeing 787 are reported to have cost \$14.4 and \$13.4 billion USD, respectively, to develop (Rodrigue, 2020). The cost of a similar project with the added complexity of supersonic flight is very likely to be greater

(Altfeld, 2016).

The utility of high-speed uncrewed aerial vehicles (UAVs) has them poised to become a crucial tool in the future development of supersonic aircraft (Cai et al., 2014). Inexpensive to produce, quick to modify, and lower risk than crewed aircraft are all attributes that lend well to the development of experimental concepts.

To assist with the development of the technologies required for a new supersonic transport aircraft, the use of UAVs as a research platform shows promise in reducing development costs while advancing the scientific field (Cai et al., 2014). By testing new technologies on a smaller-scale platform with low operating costs, companies can significantly reduce uncertainty in the development cycle and reduce their overall risk (Sobron et al., 2021). Significant challenges must be addressed by researchers before high-speed UAVs can be rapidly and reliably deployed as development tools for larger aircraft concepts and technologies (Hassanalian and Abdelkefi, 2017).

Boom Supersonic, an American company developing a new supersonic passenger jet, is first building a smaller-scale crewed aircraft as a technology demonstrator before completing development of the larger passenger jet (Boom Supersonic, 2022). This demonstrator is scheduled for first flight testing in 2023. As far back as 1974, NASA was using a high-speed drone aircraft termed BQM-34E for research into supersonic flight and the testing components for such aircraft (Eckstrom and Peele, 1974). The BQM-34E was seen by researchers as an intermediate step between wind tunnel testing and full-scale, piloted flight testing. The research also focused on the transonic speed range where wind tunnel testing is difficult (Eckstrom and Peele, 1974). A supersonic UAV capable of performing in-flight experiments has the potential to advance technologies such as novel intake systems while significantly reducing costs (Wilson et al., 2015). While supersonic wind tunnels cannot accurately recreate atmospheric conditions (Surber and Robinson, 1983), an experiment installed in a supersonic UAV is by definition exposed to atmospheric conditions. At the time of writing, there are no documented UAV flights achieving supersonic speeds in the open literature. This gap in research capabilities is the motivation behind the present work.

## 1.1 The MUFASA Project

The Multi-purpose Uncrewed Fixed-wing Advanced Supersonic Aircraft (MUFASA) project is a joint effort between the University of Calgary and Atlantis Research Labs Inc. (ARL). The project intends to develop and fly a small-scale supersonic uncrewed aerial vehicle (SSUAV). This SSUAV will be used as a research platform for advanced propulsion and intake technologies. Research work to date includes initial conceptual design with scaling and feasibility analysis (Dalman, 2021; Dalman et al., 2021), partial detailed design of a sub-25 kg model (Gair et al., 2020), and a controllability evaluation of the aerodynamic shape using simulation tools (Durante, 2023; Durante et al., 2022). Initial layout and sizing was performed by a collaborative team of faculty, undergraduate, and graduate level students. A comprehensive study examining the feasibility of a supersonic UAV was completed using SUAVE to determine an appropriate aircraft scale (Dalman, 2021; Dalman et al., 2021). Mission profiling was completed to determine maximum range and top speed at various scales. The aerodynamic shape studied by Dalman (2021) has been termed “MUFASA A”. Future versions with significant aerodynamic changes will be given subsequent letters, “MUFASA B”, etc. The team performed detailed design of this shape and completed the first stages of fabrication in the 2019-2020 academic year. This partially-constructed first prototype has been termed “MUFASA A.2”. Further analysis led to the decision to create a smaller, low-cost version to accelerate the development cycle and achieve first flight as soon as feasible. MUFASA A.1 (referred to informally as Simba) is a scaled-down version of MUFASA A.2 constructed as conventionally as possible using CNC-cut foam and readily-available hobby-grade electronics and electric propulsion. This construction method closely mimics hobbyist remote control (R/C) aircraft in an effort to reduce risk by using proven methods.

MUFASA A.1 and A.2 are intended to prove the aerodynamic shape at lower speeds and identify challenges as early as possible to mitigate the risk of building a large-scale, expensive aircraft of an unproven configuration. Figure 1.1 shows the external shape of the MUFASA A aircraft. Table 1.1 provides an overview of existing and future MUFASA versions. The overall configuration and shape of the airframe is based on early concepts and direction from the project sponsor,

Atlantis Research Labs (ARL). Future work will explore the use of composite materials at a larger scale to further increase speed and range performance. Data and experience gained from manufacturing and flying MUFASA A versions will inform the development of MUFASA B. This will be the first version intended to achieve supersonic speeds.

Table 1.1: MUFASA project aircraft versioning scheme. The focus of the present work is highlighted in bold.

Version	Description
MUFASA A	Aerodynamic shape evaluated for scaling and feasibility
<b>MUFASA A.1</b>	<b>0.62-scale low-speed demonstrator, 2.5kg maximum</b>
MUFASA A.2	1.0-scale, aluminium airframe, 25kg maximum
MUFASA B	Aerodynamic shape optimized for performance (future work)
MUFASA B.1	1.0-scale, carbon fibre airframe (future work)

The present work is focused on the construction of the simplest possible version of the MUFASA A shape in an attempt to assess the low-speed performance and general viability of the aircraft. At this early stage of the development program it is also desirable to gain experience with flight testing and data collection for effective analysis. To that end, the following research question is posed: are early-stage design methodologies for aircraft configuration and basic stability suitable for a first prototype SSUAV with a delta-winged planform?

To answer that question, the following research objective was formulated: experimentally assess the effectiveness of early-stage design methodologies for aircraft when applied to delta-winged SSUAV configurations. Specifically, the design methodologies related to propulsion and aerodynamic stability will be targeted. To achieve this research objective, the following research methodology will be used:

1. Apply conceptual design guidelines for aircraft control configuration and stability.
2. Complete manufacturing design of the provided aerodynamic shape to incorporate all required components such as flight control electronics and propulsion systems.
3. Fabricate a low-cost, rapidly-iterable prototype aircraft for flight testing.

4. Create and execute a low-speed flight test plan to enable validation of the design tools used to develop the aircraft.
5. Perform initial analysis of the collected flight data to assess low-speed stability and handling characteristics and provide recommendations for future work.

Chapter 2 summarizes a number of recent projects in the open literature with an experimental focus and stated goals of flight testing high-speed or supersonic UAVs. In the same chapter a selection of background knowledge is introduced with emphasis on challenges pertinent to delta-winged aircraft and small scale flight. The design and construction methods for the aircraft are described in Chapter 3 along with a number of design calculations relevant to stability parameters which are affected by the detailed design and manufacture of the aircraft. Ground testing of the propulsion system is detailed in Chapter 4. Then, Chapter 5 details flight test attempts and presents the results of initial data analysis collected from flight attempts. Although sustained flight was not achieved, critical lessons were learned in flight testing and from data analysis which will help guide the future of the project. Finally, conclusions of the present work and recommendations for the future of the project are discussed in Chapter 6. The launch rail system developed for use with MUFASA A.1 is described in Appendix A.

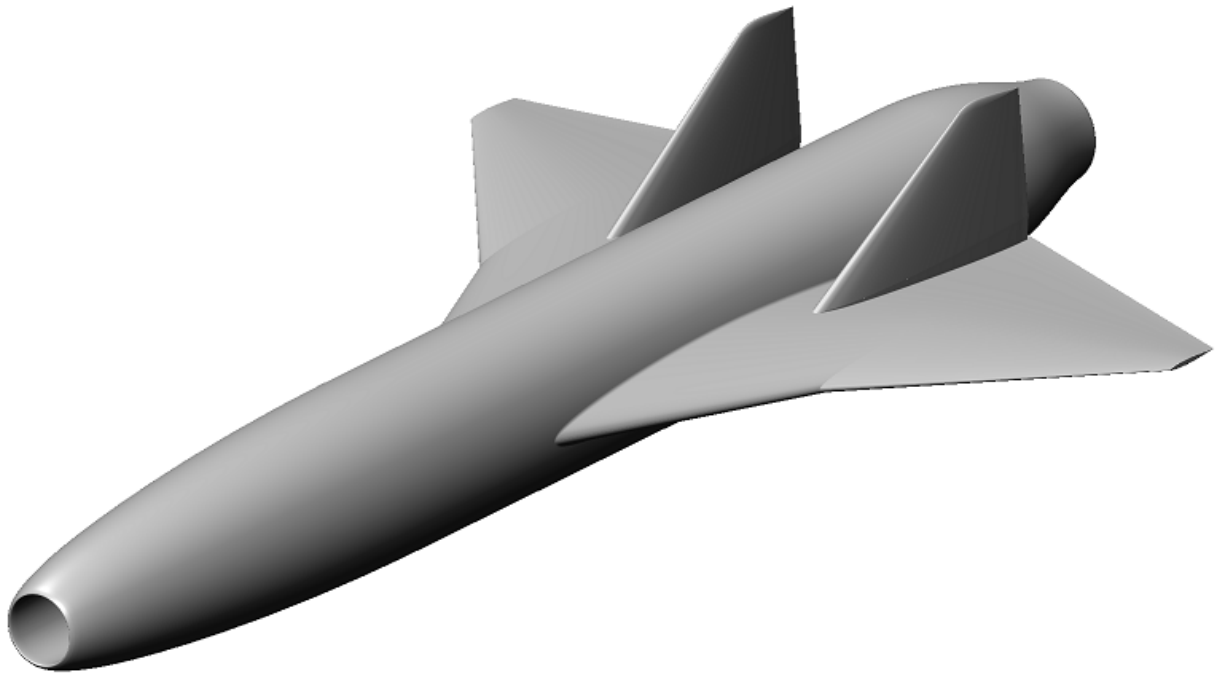


Figure 1.1: CAD image of the initial aerodynamic shape under consideration.

# Chapter 2

## Literature Review

Scientific progress and outcomes of similar high speed UAV projects are reviewed here to identify challenges and inform solutions important to the MUFASA project. A selection of challenges significant to MUFASA and other SSUAVs are then presented and their importance highlighted. Known issues including roll reversal and diminished lateral stability experienced by delta-winged aircraft at low speeds are discussed. Challenges related to small-scale aerodynamics including the reduced effectiveness of control surfaces and flow separation over wings at low speeds are also presented.

Despite the current ubiquity of UAVs, there is still debate among researchers on how to properly define and categorize them (Stöcker et al., 2017; Stansbury et al., 2015; Hassanalian and Abdelkefi, 2017). The precise definition of “small-scale” is also open to interpretation (US Joint Chiefs of Staff, 2019). To maintain consistency within the MUFASA project, the definition of a UAV set forth by Franke (2015) and used by Durante (2023) will also be used here:

“An airborne vehicle which does not carry a human operator, which may be piloted remotely, follow a pre-programmed flight path, fly autonomously, or a combination of all three. It is designed to be recoverable and carries a lethal or non-lethal payload. Nonrecoverable vehicles and projectiles such as ballistic vehicles, cruise missiles, and artillery projectiles are not considered UAVs.” (Franke (2015), p. 54)



In JP 3-30 *Joint Air Operations* the US military attempts to class “Unmanned Aircraft Systems” into groups by gross takeoff weight, normal operating altitude, and speed (US Joint Chiefs of Staff, 2019). The present work falls into the class including UAVs under 20 lbs (9.1 kg) and slower than 100 kts (51.7 m/s). This classification covers a large portion of possibilities including MUFASA A.1. The planned MUFASA B would fall into a high category given that its flight speed is projected to exceed 100 kts. As with many attempts to classify technology, it seems unlikely that a single, universal system for UAVs will be widely adopted (Stansbury et al., 2015).

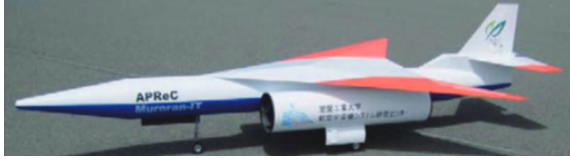
## 2.1 Existing High-Speed UAV Projects

There are relatively few published SSUAV or high-speed UAV projects in the open literature. Table 2.1 presents a sample of those in the open literature which are reviewed here. Only two of the projects include powered flight testing in the published work. None have achieved supersonic flight. Figure 2.1 shows images of the UAVs discussed here.

Table 2.1: List of existing SSUAV projects and some key parameters. Date ranges are taken from the dates of published works.

Project	Lead Organization	Outcome	Dates
NEXST	Japan Aerospace Exploration Agency	Glide flights to Mach 2.66	1998 - 2019
Ohwashi	Muroran Institute of Technology	Powered flight to 58 m/s	2005 - 2021
Pohox	Federal University of Minas Gerais	Conceptual only	2013 - 2017
GOJETT	University of Colorado-Boulder	Constructed, never flown	2011 - 2012
R-UAV	University of Washington	Low speed flights performed	2012 - 2016
SCALOS	NASA	Ongoing	2021 - 2023

One of the earliest SSUAV research projects was first published in 1998 by the National Aerospace Laboratory in Japan (Sakata, 1998). Titled the National EXperimental Supersonic Transport (NEXST), it was intended to develop and establish advanced design tools for the next generation of supersonic transport aircraft (Sakata, 2002). The group published multiple works on CFD tools and other computational design studies for supersonic transport aircraft (Ito and



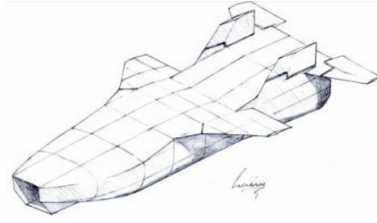
(a) Ohwashi, adapted from Mizobata et al. (2014).



(b) R-UAV in 2021, adapted from Nelson et al. (2022).



(c) NEXST-1, adapted from Machida et al. (2007).



(d) Pohox, adapted from Barbosa et al. (2014).



(e) GOJETT, adapted from Livne et al. (2017).

Figure 2.1: SSUAV concepts (not to scale).

Nakahashi, 2002; Iwamiya, 2002; Chiba et al., 2012, 2008). They also conducted a number of experimental tests starting with wind tunnel testing in 1999 (Yoshida et al., 2002) on the unpowered NEXST-1 with natural laminar flow (NLF) wings. NEXST-1 was launched by a solid rocket booster and allowed to glide while collecting data at approximately Mach 2 (Ohnuki et al., 2006). The NEXST program investigated aircraft weighing approximately 2000 kg with a wingspan of 4.7 m (Ohnuki et al., 2006). After a failed test flight of glider NEXST-1 in 2002, resources planned for the jet-powered NEXST-2 were reallocated to rebuild NEXST-1 (Yoshida, 2009). NEXST-2 was never built and the program was replaced by other work focused on demonstrating other supersonic technologies, primarily drag reduction and sonic boom minimization (Yoshida, 2009). The D-SEND (Drop test for Simplified Evaluation of Non-symmetrically Distributed sonic boom) project was part of these efforts (Honda and Yoshida, 2012). The majority of the published work relates to the guidance and control of the UAV which was dropped from a balloon to reach supersonic speeds in the test phase (Kawaguchi et al., 2012, 2017; Ninomiya et al., 2016, 2018). This work is closely related to the S3TD (Silent Supersonic Technology Demonstrator) by the same group (Chiba et al., 2012). The D-SEND#2 UAV achieved an unpowered flight speed of Mach 1.3.

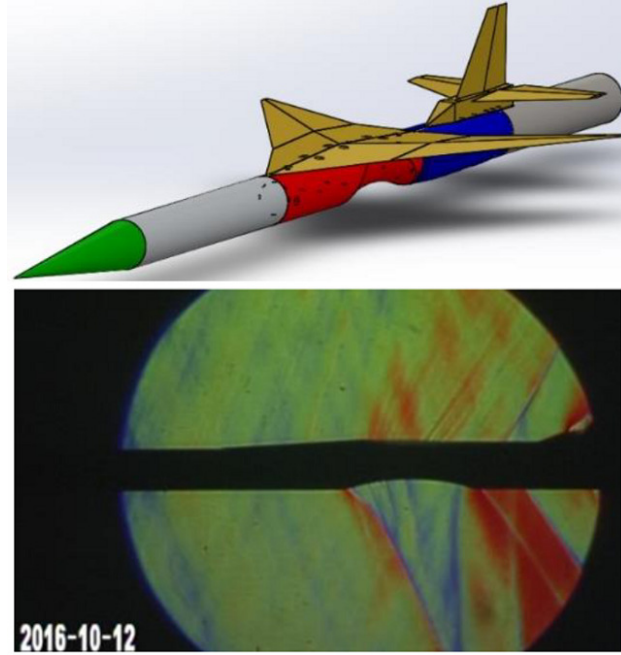


Figure 2.2: CAD model (top) and Schlieren image (bottom) of the Ohwashi M2011 configuration with narrowed fuselage taken at Mach 1.1, adapted from Yamazaki et al. (2019)

Another relevant project in Japan is the result of work by the Muroran Institute of Technology in collaboration with the Japan Aerospace Exploration Agency (JAXA). One of the goals was to address the short supersonic flight time limitation of the NEXST program by adding air-breathing propulsion. Nicknamed “Ohwashi”, the project began with the development of a counter-rotating axial turbofan engine (Minato et al., 2007) and followed with a constructed prototype which flew successfully in August 2010 (Mizobata et al., 2011). It reached a maximum speed of 58 m/s, less than Mach 0.2, but was shown to have adequate stability and control characteristics in low speed flight (Mizobata et al., 2014). The model flown, dubbed M2006, had a wingspan of 1.6 m and a total mass of 27 kg. The latest published work (Ueba et al., 2021) focused on fully autonomous control including takeoff and landing sequences. The control scheme was tested on a 3 kg purchased RC aircraft with an airspeed of approximately 20 m/s (Ueba et al., 2021). Another publication from the group is focused on reducing transonic drag by modifications to the fuselage using the area rule for supersonic wave drag minimization (Yamazaki et al., 2019). The narrowing or “bottlenecking” of the fuselage near the largest wingspan area had a positive impact but was

less positive than predicted. Figure 2.2 shows the Ohwashi geometry and a Schlieren image from a Mach 1.1 wind tunnel test, confirming the presence of shocks at the abrupt geometry changes where the fuselage narrows. Smoother transitions in the bottleneck region are planned to reduce drag due to shocks and separation in this region (Yamazaki et al., 2019).

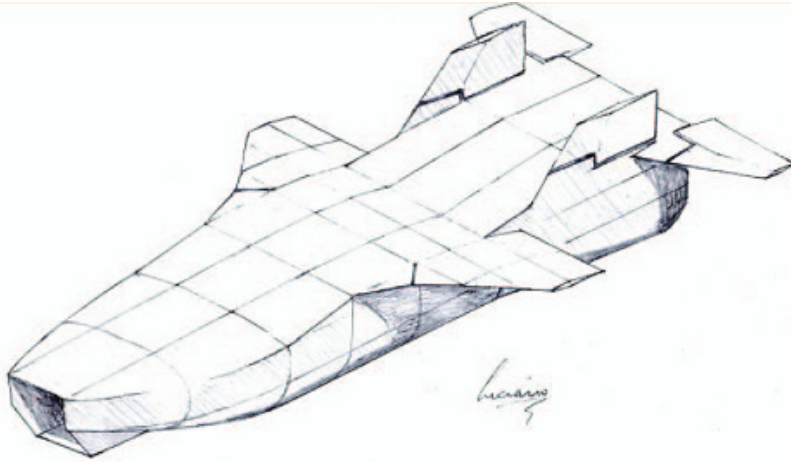


Figure 2.3: Pohox configuration drawing, adapted from Magn and Barbosa (2013).

A team in Brazil first published work in 2013 describing the configuration of a supersonic UAV dubbed “Pohox” (Magn and Barbosa, 2013) with the stated purpose of being a flying test bed for an experimental multi-cycle engine (Gabaldo et al., 2016). The group makes reference to the X-15 experimental aircraft as a reference for validation of prediction techniques, in particular drag performance. While the roles of the Pohox and the X-15 are similar, the scale is vastly different. The X-15 had a wingspan of 6.8 metres (Thompson, 2003) compared with the proposed 0.44 m wingspan of the Pohox (Magn and Barbosa, 2013). To the best knowledge of the author, only two publications on the Pohox are available in the open literature, with a handful more related to the experimental engine (Gabaldo et al., 2016, 2017). The early configuration drawings of the Pohox concept show a relatively thick fuselage with extremely short wings. Figure 2.3 shows an early drawing of the Pohox concept. No other images of the design were found in the published works.

The Graduate Organization Jet Engine Technology Team (GOJETT) at the University of Colorado Boulder first published a paper in 2012 introducing work towards a supersonic UAV (Walter and Starkey, 2012a). Their stated goal was to “build the worlds fastest 50kg unmanned aerial sys-

tem (UAS)” while incorporating an afterburner, variable area nozzle, and fluidic injection thrust vectoring. The project intended to make use of the resulting aircraft as a research test bed for topics such as sonic boom minimization, storm penetration, thrust vectoring and control algorithms (Walter and Starkey, 2012b). Controls analysis by Wienke (2011) suggests that the GOJETT aerodynamic shape is laterally unstable without a vertical tail. Since 2012, no further published work has been made available on the GOJETT project. No successful flight tests were documented.

The University of Washington has a program led by Dr. Eli Livne aimed at the rapid development of small research UAVs by undergraduate students aided by experienced mentors and the Boeing Company (Livne et al., 2017). This program, termed R-UAV, led to the publication of a thesis by Langston (2015) on the low-speed stability and control of a tailless supersonic configuration. The work began as a full-scale aircraft designed for Mach 1.8 flight with 10 passengers and was subsequently scaled down to 1/16th size to study subsonic characteristics, in particular the low-speed handling (Langston, 2015). That work showed that a combination of angled canards in conjunction with trailing edge flaps and drag devices can effectively control a supersonic-configured aircraft at low speeds with no vertical tail. Active control was required to maintain lateral stability (Langston et al., 2016). The R-UAV project has produced nearly a dozen different models of the aircraft since work began, some build by undergraduate teams and some by researchers. Images of some of these models are shown in Fig. 2.4.

Results and lessons from the R-UAV project at the University of Washington are contributing to a NASA-led initiative called SCALOS (Supersonic Configurations A LOw Speed) (Nelson et al., 2022). Wind tunnel testing at the University of Washington was conducted on a large number of supersonic transport aircraft configurations (Nelson et al., 2022). The understanding and accurate prediction of low-speed handling of supersonic configurations has been identified as a critical design point for supersonic transport aircraft and is a stated research focus of the project (Livne et al., 2017). As this project is relatively new, the published research is minimal; only papers on model geometry and aerodynamic results (Ting et al., 2022) and correlation studies between test and simulation results (Mavriplis et al., 2022) are available at the time of writing.



Figure 2.4: Various R-UAV models constructed and tested at the University of Washington, adapted from Nelson et al. (2022).

## 2.2 SSUAV Technical Challenges

Certain documented technical challenges appear in literature which are critical to the present work and the development of SSUAVs in general. Section 2.2.1 discusses aerodynamic features of delta wings. Their method of vortex lift production is introduced along with challenges experienced in low-speed flight. Roll reversal and lateral instability of delta-wing configurations is of particular importance to the present work. Challenges surrounding aerodynamics at smaller scales compared to conventional supersonic aircraft are treated in Section 2.2.2. The reduced effectiveness of control surfaces in low-Reynolds flight and the increased friction drag component at small scale are discussed.

### 2.2.1 Delta-winged Aircraft

Delta-winged aircraft rely on a fundamentally different aerodynamic principle for lift generation than conventional-winged aircraft. Conventional wing lift is described well by the Kutta-Joukowski theorem using inviscid, incompressible flow (Schlichting and Truckenbrodt, 1979). The intricacies are not subject to detailed treatment here, but it is sufficient to understand that airflow incident on an airfoil shape results in a pressure differential between the upper and lower

surfaces. This pressure difference acting on the surface area of the airfoil results in the lift force. By contrast, a delta wing generates lift by the formation of a pair of vortices extending from the leading-edge root downstream to the trailing edge (Hoerner, 1985). This “vortex lift” is a viscous phenomenon not predicted in linear potential flow such as the Kutta-Joukowski theorem (Gudmundsson, 2022b). Hoerner (1985) goes on to state that “these vortices exert a large influence on the lift characteristics of the delta wing, especially at high angles of attack”. Figure 2.5 shows an illustration of the vortices present on the upper surface of a delta wing at sufficient speed and angle of attack (AoA) to generate vortex lift (Hoerner, 1985).

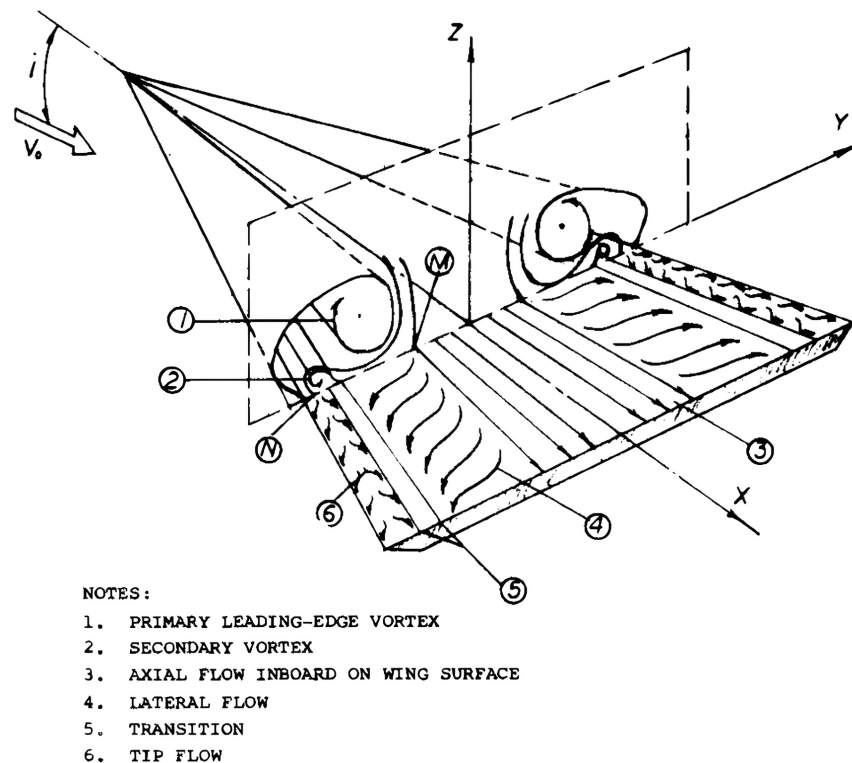


Figure 2.5: Illustration of delta wing vortices critical in lift generation, from Hoerner (1985).

As delta wings generate lift differently than conventional wings, they also experience “stall” differently. A stall is defined for a conventional wing as a loss of lift due to flow separation (Hoerner, 1985). A delta wing stalls when the vortices present on the upper surface break down or “burst” and cause a loss of lift (Schlichting and Truckenbrodt, 1979). The vortices first break down aft of the trailing edge, moving forward towards the trailing edge as AoA increases. This gradual



break down results in a more gradual loss of lift than the abrupt loss characteristic of conventional wings (Truckenbrodt, 1954). Figure 2.6 shows experimentally determined lift curves for various aspect ratio planforms. The delayed stall of the 0.83 and 1.61 aspect ratio models is due to vortex lift.

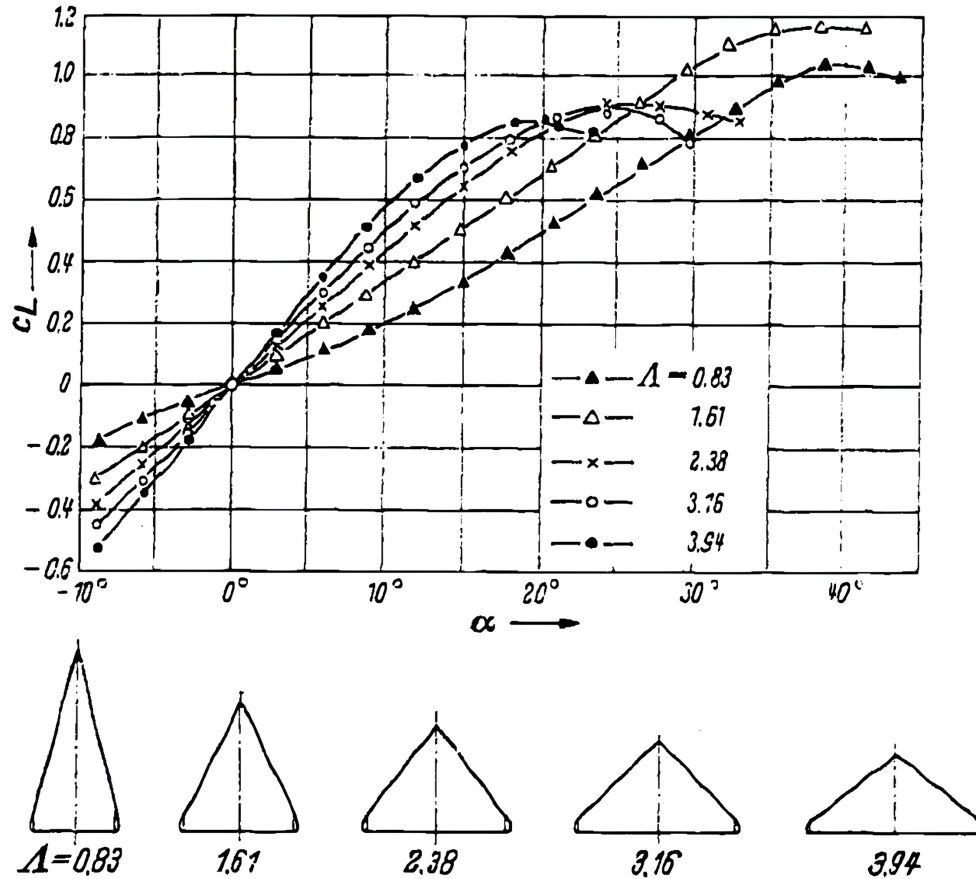


Figure 2.6: Experimentally-determined lift curves for delta wings of various aspect ratios,  $Re \approx 7 \times 10^5$ , from Truckenbrodt (1954).

A feature of the vortex lift generated by delta wings is a significantly expanded range of angles of attack which generate usable lift; the stall angle for a given speed is much larger than for conventional wings. Where a non-delta planform with a typical NACA airfoil might stall between  $15\text{-}20^\circ$  AoA (Selig, 1995), a delta-wing planform can exhibit a stall angle greater than  $35^\circ$  (Earnshaw and Lawford, 1964). It is important to note that the stall angle is influenced by more than just planform shape; airfoil profile, Reynolds number and other factors also play a role (Anderson,



1999). Delayed (high AoA) stall is important for allowing delta winged aircraft to fly at reduced speeds during takeoff and landing sequences in particular. Without this delayed stall characteristic, aircraft such as fighter jets would have unreasonably high takeoff and landing speeds and require much longer runways.

## **Roll Reversal**

On a delta wing at a high AoA, there exist regions of unsteady flows with varying degrees of separation which are asymmetric between the two wings (Gursul, 1994; Lorinz, 1980). These unsteady flows can contribute to the reduced effectiveness of conventional control surfaces (Greenwell and Wood, 1994). In this condition a delta wing is still producing lift (i.e. it is not fully stalled) but the vortices are beginning to break down near the trailing edge, creating unstable and unpredictable lift characteristics. Consider a roll-right command where the left aileron deflects downward. On a delta with a partially burst vortex this deflection further disrupts the vortex and can exacerbate the loss of lift (Maines et al., 2009). This wing then drops, causing an uncommanded roll-left or “reversing” the commanded roll. Various methods of controlling vortical flows are under investigation in search of ways to improve stability and control of delta wing aircraft (Gursul, 2004; Pfnur et al., 2020; Polhamus, 1986). Research related to roll reversal of delta wings is important to the development of future supersonic aircraft; improvements to stability through flow control could reduce the required size of tail surfaces, thereby reducing drag and improving performance and efficiency.

The F-14 is an example of an aircraft with known roll reversal and lateral stability issues (Gera et al., 1981). Aircraft carrier landings are an extreme situation demanding precise control at very low speeds. A flow visualisation study of the F-14 by Lorinz (1980) showed vortex asymmetries and instabilities at high AoA conditions with no sideslip. Vortex flow was present over the highly-swept inboard wing section, even with the wings extended as in landing configuration. The addition of a sideslip or crosswind component will further destabilize the vortex flow field, exacerbating the control and stability challenge. In a single engine landing where the thrust imbalance causes a

yaw towards the inoperative engine, airflow over that same wing is disrupted by the nose and by “adverse sidewash from the windward vortex” (Lorinz, 1980). In this situation the Navy flight manual for the F-14A instructs pilots to control roll using rudder input instead of aileron input (US Naval Air Command, 2004). An aileron deflection down on the wing with already disturbed airflow can cause a further loss of lift and thus a roll reversal.

Reports also show that researchers were developing stability augmentation systems targeted at low speed, high-AoA flight using the F-14 as a demonstrator (Gera et al., 1981). Other, potentially simpler methods of improving low speed handling were explored, including an aileron-rudder interconnect system (Kelley and Enevoldson, 1981). The aileron-rudder interconnect system showed significantly improved control in landing configuration (Bihle and Meyer, 1976). The research was motivated by reports from pilots of excessive adverse yaw following lateral stick (aileron) inputs on final approach (Kelley and Enevoldson, 1981). Earlier research also explores the challenges of roll reversal and directional control with delta-winged aircraft (White and Innis, 1959; Johnson and Boisseau, 1953). Both of those studies discuss adverse sideslip and poor roll control at high AoA.

### **Lateral Stability Challenges**

Connected to the challenge of roll reversal is the issue of lateral stability for delta wings. The F-14 case demonstrated the disastrous effects of excessive adverse sideslip at low speeds. Much earlier, in the 1950s, Convair was developing some of the earliest delta-winged aircraft for supersonic flight (Mendenhall, 1983). Engineers at Convair spent significant resources investigating low speed handling characteristics and attempting to improve controllability (Tempelmeyer and Osborne, 1955). In particular, free-flight wind tunnel studies using scaled models of the YF-102 were performed (Johnson and Boisseau, 1953) to evaluate low-speed handling and stability at various angles of attack approaching stall. They found that near stall (conditions typical of a carrier takeoff or landing) the model became laterally unstable and directionally divergent. Various configuration changes were tested. A configuration with leading-edge slats and a vertical tail 40% larger than the

original design resulted in satisfactory stability (Johnson and Boisseau, 1953). At the same time however, the adverse sideslip characteristics remained potentially “objectionable at high angles of attack” (Johnson and Boisseau, 1953). The information gained from this study informed the design of the F-102A model. Compared with the YF-102, the F-102A had a longer fuselage, longer tail moment arm, drooped leading edge, and chordwise wing fences near the semispan of each wing (Boisseau, 1955). The results were a significant improvement in the directional stability of the aircraft at high angles of attack. Once again, the researchers experimented with increased vertical tail sizes and found increased stability with the larger tail, particularly near stall conditions. Previously produced F-102 aircraft were modified to include some of the improved stability features that resulted from these wind tunnel studies (Mendenhall, 1983).

This issue of lateral stability with delta-winged aircraft is not limited to the early days of supersonic flight, but is a topic of significant current research (Colgren and Loschke, 2008). The control of tailless aircraft and delta wings is the subject of many recent publications (Stenfelt and Ringertz, 2009; Ciliberti et al., 2017; Goodman, 2014). Tailless aircraft are typically seen as advantageous for sonic boom minimization and improvement of stealth characteristics. Challenges remain with the accurate prediction of stability and control characteristics, and flight testing either outdoors or in a wind tunnel remains the most effective way to determine these characteristics (Morelli, 2012).

### **2.2.2 Small-Scale Effects**

Comparison of flight conditions across aircraft of varying size and speed is facilitated by Reynolds number, the ratio of momentum to viscous effects on the fluid flow (Gerhart et al., 2016). Aircraft are typically characterized by the mean aerodynamic chord length (MAC, described in Section 3.1.1). MAC is used because flow over the wings to produce lift is of primary concern for aircraft designers (Hoerner, 1985). Reynolds number increases linearly with aircraft speed and the chord of the wings. It follows that aircraft such as UAVs operate at Reynolds numbers multiple orders of magnitude lower than crewed aircraft. Takeoff speeds for a full-scale fighter jet are already considered low-Reynolds conditions (Polhamus, 1986), thus UAVs experience an extreme

example of low-Reynolds flight.

High performance military jets with wide operating envelopes are known to suffer performance degradation in low-Reynolds-number flight (Gera et al., 1981; Luckring, 2010). Their requirements dictate that design be focused on high-speed performance, however they must still reliably fly slow enough to take off and land. Significant research has been conducted in search of ways to delay flow separation on jet aircraft in particular (Maines et al., 2009; Luckring, 2002; Hummel, 2004). One counter to the effects of flow separation in low Reynolds flight is an airfoil profile optimized for performance at those conditions. Targeted airfoil profiles have been explored and developed for use at low Reynolds numbers, notably by Selig and Guglielmo (1997), and Drela (1989). Data indicates that very large performance improvements have been obtained from such design work. Unfortunately, these airfoils are typically optimized for high-lift, low-speed flight to optimize efficiency, endurance, and stability (Selig and Guglielmo, 1997). This makes them less applicable to the development of SSUAVs. A trade-off decision must therefore be made between low-speed stability and high-speed performance.

An extension of the reduced performance of airfoils in low Reynolds flight is a loss in effectiveness of control surfaces. Results from Prudente and Cavalieri (2007) show that, for UAVs operating in a lower Reynolds number regime, the relative effectiveness of trailing edge flaps is significantly reduced compared to larger aircraft. For a number of reasons, this change in aerodynamic behaviour is significant. Experimental results from wind tunnel tests conducted on a flapped wing model at Reynolds numbers between  $5.9 \times 10^4$  and  $2.13 \times 10^5$  showed reduced efficiency compared with methods developed for full-scale aircraft (Prudente and Cavalieri, 2007; Prudente, 2005). In addition to the reduced efficiency, the wing at low Reynolds numbers exhibited earlier stall characteristics than would be expected for larger-scale aircraft. At a neutral AoA, Prudente and Cavalieri report boundary layer separation (visible with wool tufts) for flap deflections of  $-15^\circ$ ,  $15^\circ$ , and  $30^\circ$  throughout the investigated range of Reynolds numbers. The authors also investigated the reduction in lift curve slope of airfoils at reduced Reynolds numbers. Their results are said to agree with statements made by Schlichting and Truckenbrodt (1979) and at-

tribute the reduction in lift to the increased displacement thickness associated with boundary layer flow at reduced Reynolds numbers. This reasoning is aligned with other available reports (Mueller and DeLaurier, 2003). Increased displacement thickness on the upper airfoil surface effectively reduces the camber of the airfoil due to the increased dominance of viscous forces over inertial forces. Schlichting and Truckenbrodt (1979) also show increased friction drag at lower Reynolds numbers, again indicating that smaller-scale UAVs have greater drag and viscous effects relative to their size.

The effects of both the reduced lift slope and reduced flap effectiveness are important the development of SSUAVs. The reduced lift slope disproportionately affects the vertical stabilizers responsible for lateral stability. Initial vertical tail sizing done using conventional early-stage methods could result in an undersized tail and marginal lateral stability. Reduced effectiveness of vertical stabilizers should lead a designer to increase the size of the verticals, move them aft to increase moment arm, or a combination of the two.

Reduced flap effectiveness has a particularly large impact on the MUFASA shape; the trailing edge flaps are responsible for two axes of control. Both roll and pitch control are provided by trailing edge plain flaps acting as “elevons”. As with the vertical tail, early-stage sizing methods for ailerons/elevators are targeted to full-scale, crewed aircraft (Raymer, 2018). The significantly reduced effectiveness could lead to an aircraft with insufficient pitch and roll authority. Additionally, the flow separation characteristics of the deflected plain flap are cause for concern. Flow separation indicates a stalled airfoil condition (Anderson, 1999) and a loss of lift. When a trailing edge flap, designed for control authority, enters a stall under deflection a loss of controlled flight is likely to follow. It is known that flow separation over airfoils occurs more readily at low-Reynolds numbers (Hoerner, 1985), making this condition more common and more detrimental with small-scale aircraft such as MUFASA.

## Chapter 3

# Aircraft Design & Construction

The MUFASA aerodynamic shape was predetermined before the present work began. The focus of this work was the completion of detailed mechanical and manufacturing design while preserving the overall shape to produce a rapidly manufacturable prototype for early flight testing. The shape of MUFASA A is intended to balance performance against the manufacturability of a prototype design. In a field where early development tools are imprecise and potentially unsuitable at the present scale of aircraft, a rapid development cycle with an emphasis on testing of non-optimized designs is desirable to avoid wasting resources fine-tuning a design that could be fundamentally flawed. By testing a prototype that shows promise and represents a step in the right direction it is possible to validate existing design processes and provide feedback early in the development timeline where significant changes are less costly and easier to execute. MUFASA A.1 is a scaled-down, low-speed demonstrator sized to accommodate commercially-available electric propulsion and flight controllers.

The aerodynamic design with respect to stability, control surface sizing, propulsion requirements, and related parameters was not examined further by the author in the interest of prioritizing experimental testing. Section 3.1.1 gives a basic description of the stability considerations affected by the manufacture of the aircraft, primarily related to the location of the centre of gravity (CG) and the effects on longitudinal stability. A review of early-stage vertical tail sizing methods is pre-

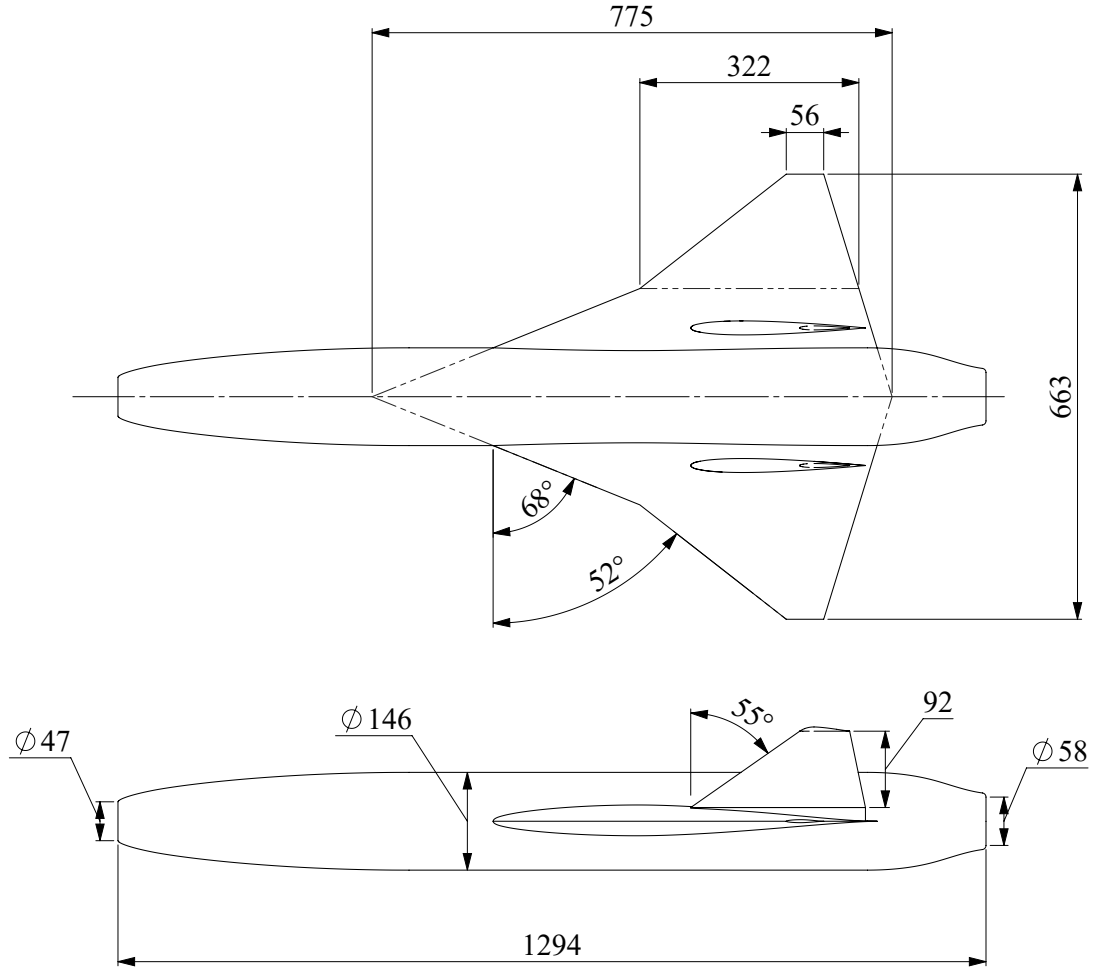


Figure 3.1: MUFASA A.1 V1 planform and general layout with key dimensions in millimetres.

sented in Section 3.1.3. Vertical tail sizing has a substantial effect lateral stability and adverse roll. This review was conducted after the completion of the second day of unsuccessful flight attempts in an effort to understand the behaviour of the aircraft. A description of the minor design refinements made to the aircraft after the first day of unsuccessful flight attempts follows in Section 3.4. Section 3.3 gives a detailed description of the method of construction and other design decisions made in the manufacture of the prototypes. Section 3.4 details the changes made to the aircraft following the first set of test flight attempts. The versions are referred to as MUFASA A.1 V1 and V2, respectively.

The MUFASA aircraft is a single-engine, double-delta wing design with a single pitot air intake

on the nose. Pitch and roll control comes from twin elevons on the trailing edges of the wings acting as both elevators and ailerons. Yaw control and stability is provided by twin, all-movable vertical tail surfaces located on the upper wing surfaces. Takeoff is facilitated by a launch rail to eliminate the weight and drag penalty of landing gear and the need for a runway. The belly of the fuselage is reinforced with a glass-fibre composite to facilitate a belly landing on a grass surface. Figure 3.1 shows the layout of the original design (V1) with some key dimensions.

The electric ducted fan (EDF) selected and used for flight testing consists of a 12-blade, 70 mm-diameter fan with a brushless DC motor rated for a power of 1700 watts (Turbines-RC, 2021). The fan and motor were purchased as a kit manufactured by JP Hobby. Manufacturer specifications claim a thrust output of 2.35 kg (23.0 N) (discussed further in Section 4.2). At full power the fan rotates at approximately 50 000 rpm, powered by an electronic speed controller (ESC) at 22.2 volts. The minimum required thrust for the aircraft was determined to be 10.5 N from simulations performed by Dalman (2021) and by Durante (2023). With a target all up weight (AUW) of 2.5 kg maximum, the selected EDF would give a thrust to weight ratio of slightly less than unity. This is similar to fighter jet aircraft with supersonic cruise capabilities (Crosby, 2020). Estimates by Dalman (2021) and simulations by Durante (2023) indicate that the stall speed is approximately 20 m/s for an engine thrust of 10.5 N. Thrust significantly affects stall speed as the vertical component of thrust contributes to lift at high AoA. Takeoff speed was set at 22 m/s, or 1.1 times the stall speed (Raymer, 2018).

The control electronics for the aircraft were selected after discussion among team members to ensure that the appropriate features were available and that all accessory interfaces were compatible. It was also important to ensure that the appropriate data parameters could be collected for further analysis of the flight tests. These data parameters are discussed in Section 5.1. The controller also needed to be compatible with the Ardupilot open-source autopilot software suite (ArduPilot Dev Team, 2023). A Holybro Durandal flight controller was selected for data collection and autopilot control as it contains a wide array of sensors including redundant gyroscope/accelerometers, magnetic compass, barometer, and onboard processing capabilities (Holybro, 2021). The Durandal



has a separate GPS module located away from other electronics for accuracy and configurable ports for interfacing with air data, 900 MHz telemetry and radar altimeter modules. The pulse-width modulation (PWM) servo ports are sufficient for the present controls configuration with room for future expansion. A final deciding factor for selecting the Durandal over other options was the package shape; the lower profile shape was much easier to fit in the available space compared with other controllers having a cube-shaped exterior.

The chosen airfoil profile belongs to the NACA 6-series set of airfoils. NACA 6-series airfoils were developed with a focus on maximizing laminar flow in the design operating envelope to minimize drag for a small range of lift coefficients (Abbott and von Doenhoff, 1959). This low drag at design conditions makes them well-suited to high-speed flight. Some drawbacks exist including poor stall behaviour, large pitching moments, and large drag in off-design flight conditions (Cantwell, 2013). The complete designation for the airfoil used here is NACA 64(0.3)08 a=0.5. A breakdown of the meaning of each term is given in Table 3.1.

Table 3.1: Explanation of NACA 64(0.3)08 a=0.5 airfoil used for MUFASA A.1

Design Parameter	NACA Digit	Meaning
Location of Maximum Thickness	4	40% along chord
Design Lift Coefficient (AoA=0)	0.3	$c_l = 0.03$
Thickness/Chord Ratio, Max	08	8%
Design Laminar Flow Percentage	a=0.5	50%

The bulk of the present design work focused on the structure and build method for the airframe. A number of engineering design requirements were taken into account when detailing the structure. The following points represent the key requirements of the manufacturing design. Further discussion of the specific design decisions made is presented in Section 3.3.

- Weight must be kept to a minimum while maintaining sufficient strength to handle flight loads.
- The final airframe must be an accurate representation of the aerodynamic shape being studied.

- Vulnerable parts should be field replaceable in the event of a crash.
- Electronics must be protected from impact and arranged to minimize interference between sensors, antennas and high-current wires.
- The CG must be adjustable and within acceptable margins for static pitch stability.

## 3.1 Aircraft Control Characteristics

Despite receiving a complete aerodynamic shape as an input to the project, it was necessary to gain a general understanding of flight stability parameters before completing the detailed design of the aircraft. Aircraft textbooks define the stability of any system as the tendency of the system to return to an equilibrium state either at rest or in uniform motion (Etkin and Reid, 1996; Roskam, 1998; Anderson, 1999). Review of the literature makes it clear that aircraft flight dynamics is a dedicated speciality with extremely complex and interconnected or “coupled” parameters. An entire thesis by Durante (2023), conducted in parallel with the present work, is dedicated to the controllability and handling of the MUFASA shape. A simplified treatment of aircraft stability is found in Raymer’s “Aircraft design: a conceptual approach”. This thesis examines portions of the early stages of the design process and includes methods based in part on past, flight-proven aircraft for verification (Raymer, 2018).

### 3.1.1 Pitch Stability

For the purposes of manufacturing design, and within the author’s scope of work, the primary concern is stability in pitching motion or “longitudinal stability”. The reasons for this are two-fold:

- Overall static stability is most significantly influenced by longitudinal (pitch) stability (Etkin and Reid, 1996)
- Aircraft CG location is the primary factor affecting static pitch stability (Roskam, 1998)

The static longitudinal or pitch stability of an aircraft is governed primarily by the relative location of the centre of gravity and the neutral point or aerodynamic centre. The neutral point is the chordwise location of the center of gravity which results in neutral stability (Hoerner, 1985). However, the neutral point location can change with changing AoA, making it an inconvenient reference point. The preferred reference point is the aerodynamic center (AC), defined as the chordwise location where pitching moment is constant with respect to AoA (Schlichting and Truckenbrodt, 1979). Positive static stability is achieved by locating the centre of gravity of the aircraft ahead of the aerodynamic centre (Roskam and Lan, 1997). The distance forward from the AC to the CG is known as static margin (SM) and is typically expressed as a percentage of MAC. An aircraft is considered to have positive static pitch stability if the aircraft returns to nose-level flight after a momentary disturbance pushing the nose up or down is applied and removed. Static margin can be expressed by equation 3.1, presented here as defined by Raymer (2018):

$$SM = \bar{X}_{np} - \bar{X}_{cg} = -\frac{C_{M\alpha}}{C_{L\alpha}} \quad (3.1)$$

where  $\bar{X}_{np}$  and  $\bar{X}_{cg}$  are the longitudinal positions of the neutral point and centre of gravity, respectively.  $C_{M\alpha}$  and  $C_{L\alpha}$  are the coefficients of pitching moment and lift with respect to AoA, respectively. The negative ratio of the two coefficients requires that the pitching moment acts to restore equilibrium as opposed to diverge from equilibrium. Static margin is normally expressed as a percentage of MAC. 10-15% is often given as the typical static margin for general aviation aircraft (Raymer, 2018; Nelson, 1998). In general, a larger static margin will serve to increase longitudinal stability at the expense of control responsiveness (Newman and Swaim, 1986). Excessive static margin must be overcome by large elevator inputs to maintain control authority, resulting in flight at the edge of control and with large trim drag effects (Kroo, 1994; Cook and de Castro, 2004).

A transport jet at its aftmost allowable CG (least stable condition) typically has at least 5-10% static margin (Jenkinson et al., 1999); safety is the primary concern in this case. Where extreme maneuverability is required (i.e. fighter jets), zero or even negative static margin can drastically increase turn rates, however advanced stability computers are required to compensate

for the statically unstable configuration (Loschke, 2003). 15% static margin was used as the target value for MUFASA A.1 to provide the best chance of successful flight, balancing stability with control authority. The approximate relative locations of the aerodynamic center and centre of gravity are shown in Fig. 3.2.

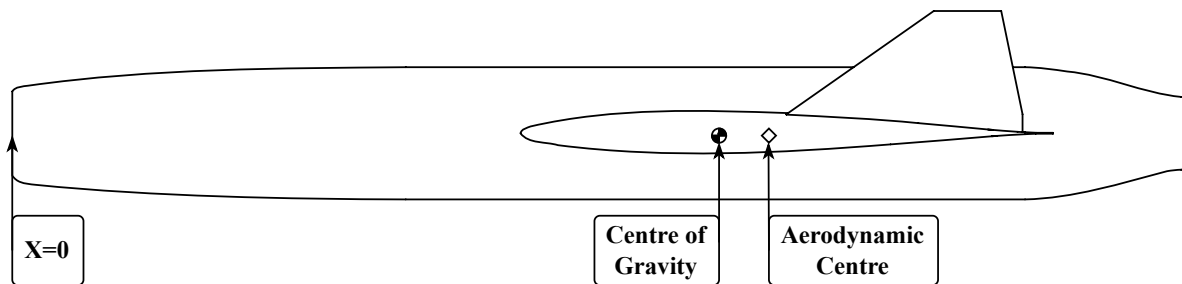


Figure 3.2: Side view of MUFASA A.1 showing target CG location and aerodynamic centre for approximately 15% static margin.

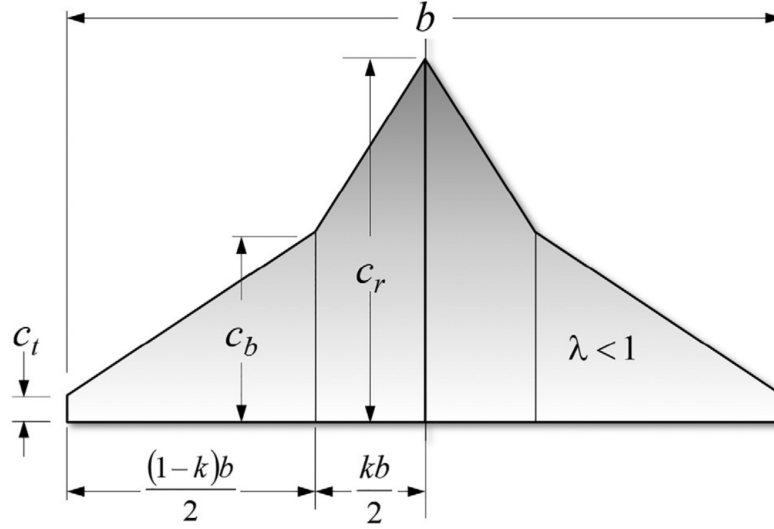
### 3.1.2 Calculation of Mean Aerodynamic Chord

The mean aerodynamic chord of a wing is a convenient parameter that is used to represent the behaviour of a complete wing. As noted by Raymer (2018), “What makes the MAC special is that it somehow acts as if all the area of the wing is concentrated on that chord.”

Aerodynamically, MAC is defined as the chord length which yields the aerodynamic moment about the aerodynamic centre when multiplied by the wing area, dynamic pressure, and moment coefficient (Anderson, 1999). This length is important for longitudinal wing positioning; the subsonic aerodynamic centre is located at approximately the quarter-chord point of the MAC, typically known as 0.25MAC (Raymer, 2018). This is the neutral point used for locating the centre of gravity to ensure static pitch stability.

Gudmundsson (2022b) uses the term mean geometric chord (MGC) in place of MAC. MGC is a more accurate description of the term derived from the planform geometry. The MGC is fundamentally the chord length at the geometric centroid of the planform area (Yates, 1952). MAC is the dominant term used in literature, even where authors are using MGC. The present work follows the same convention of using MAC throughout.

The calculation of mean aerodynamic chord for a double-delta wing aircraft such as MUFASA is more complex than a typical tapered wing with moderate sweep angle. Detailed equations and diagrams are found in Gudmundsson (2022b) and partially reproduced in Fig. 3.3.



$$\bar{Y}_{MAC} = \frac{2}{S}[A + B + C + D] \quad S = \frac{b}{2}(k(c_r - c_t) + c_b + c_t) \quad a = \frac{c_t - c_b}{b/2 - \bar{Y}_b} \quad (3.2)$$

$$A = \frac{1}{2}(c_r - c_b)\bar{Y}_b^2 \quad B = \frac{1}{3}\left(\frac{c_b - c_r}{\bar{Y}_b} + \frac{1}{2}a\right)\bar{Y}_b^3 \quad (3.3)$$

$$C = \frac{1}{2}(c_b - a\bar{Y}_b)\left(\frac{b}{2}\right)^2 \quad D = \frac{1}{3}a\left(\frac{b}{2}\right)^3 \quad (3.4)$$

Figure 3.3: Diagram and equations necessary for MAC calculation of a double-delta planform. Diagram and equations from Gudmundsson (2022b)

The equations shown in Fig. 3.3 are the result of integrating over the planform area to determine the spanwise location of the geometric centroid. Intermediate coefficients  $a, A, B, C, D$  are used to simplify the final equation. Parameter  $k$  is a ratio defining the spanwise location of the

discontinuity in planform.  $S$  is the planform area,  $b$  is the full wingspan, and  $c_r, c_b, c_t$  are the chord lengths at the reference line, discontinuity, and wingtip respectively. These equations are used to calculate first the spanwise location of the geometric centre  $\bar{Y}_{MAC}$ . Then the appropriate equation from Eq. (3.5) & Eq. (3.6) is used to determine mean aerodynamic chord  $c_{MAC}$ .

$$\text{if } \bar{Y}_{MAC} \leq \bar{Y}_b \quad \text{then} \quad c_{MAC} = c_r(c_b - c_r) \frac{\bar{Y}_{MAC}}{\bar{Y}_b} \quad (3.5)$$

$$\text{if } \bar{Y}_{MAC} > \bar{Y}_b \quad \text{then} \quad c_{MAC} = c_b + \left( \frac{c_t - c_b}{b/2 - \bar{Y}_b} \right) (\bar{Y}_{MAC} - \bar{Y}_b) \quad (3.6)$$

Table 3.2 lists the parameters used to calculate MAC for MUFASA A.1 following the method described above. Changes to the planform from V1 to V2, fully described in Section 3.4, decrease the MAC length and shift its location further outboard on the wing. The primary effect of this change is a shift in the location of 0.25MAC further aft by 35 mm. This shortens the vertical tail moment arm (Section 3.1.3) and changes the target location for the centre of gravity to achieve static pitch stability (Section 3.1.1).

Table 3.2: Calculation parameters for MAC of MUFASA A.1

Dimension	MUFASA A.1 V1	MUFASA A.1 V2
Wingspan, $b$	663 mm	760 mm
Planform Area, $S$	0.241 m <sup>2</sup>	0.274 m <sup>2</sup>
Reference Chord, $c_r$	775 mm	775 mm
Discontinuity Chord, $c_b$	322 mm	355 mm
Tip Chord, $c_t$	55.8 mm	54.5 mm
Discontinuity Span, $\bar{Y}_b$	161 mm	163 mm
Calculated MAC Span, $\bar{Y}_{MAC}$	112 mm	128 mm
Calculated MAC, $c_{MAC}$	461 mm	443 mm

### 3.1.3 Lateral Stability

The lateral stability of an aircraft is governed primarily by the effects of the vertical tail. Acting similar to a weathervane, the vertical tail surface is designed to provide a side-force (yawing moment) to turn the nose of an aircraft into the wind (Gudmundsson, 2022a). A larger vertical

tail situated further aft of the centre of gravity will provide greater stability than a smaller surface further forward. Initial sizing of the vertical tail is typically performed using the tail volume coefficient method. The same method is used for horizontal tail sizing on conventional aircraft; with no distinct horizontal tail the analysis does not apply to MUFASA. Equation 3.7 is used to calculate the dimensionless vertical tail volume coefficient. The product of vertical tail moment arm  $l_{VT}$  and surface area  $S_{VT}$  is non-dimensionalized by the wingspan  $b$  and planform area  $S$ . Raymer (2018) states that wingspan and planform are used as they are most directly related to the wing yawing moments which must be countered by the vertical tail to achieve directional stability.

$$V_{VT} = \frac{l_{VT}S_{VT}}{bS} \quad (3.7)$$

Table 3.3 shows the calculated values of vertical tail volume coefficient for MUFASA A.1. Changes to the aircraft from V1 to V2 had the effect of moving the 0.25MAC point and neutral point further aft. This shortened the vertical tail moment arm used in calculating tail volume coefficient, indicating reduced vertical tail effectiveness. The tail was not enlarged for V2 to maintain the low-drag design and because simulations indicated that the aircraft remained laterally stable. A complete discussion of lateral stability for the MUFASA shape and other tailless delta-winged aircraft can be found in Section 5.4.3.

Table 3.3: Calculation parameters for vertical tail volume coefficient of MUFASA A.1

Dimension	MUFASA A.1 V1	MUFASA A.1 V2
Wingspan, $b$	663 mm	760 mm
Planform Area, $S$	0.241 m <sup>2</sup>	0.274 m <sup>2</sup>
Vertical Tail Moment Arm, $l_{VT}$	188 mm	133 mm
Vertical Tail Area, $S_{VT}$	0.0398 m <sup>2</sup>	0.0398 m <sup>2</sup>
Vertical Tail Volume Coefficient, $V_{VT}$	0.0468	0.0254

The value of vertical tail volume coefficient does not singularly predict the lateral stability of an aircraft. It is used extensively by designers as a first-approximation of tail size in the conceptual design phase (Nicolosi et al., 2017). The tail sizing process is described by Anderson (1999) as “one of the most empirical and least precise aspects of the airplane design process”. A helpful

review of tail sizing statistics and methods, focused on the vertical tail, was published in 2013 by Barua et al.. Table 3.4 compiles suggested vertical tail volume coefficients given in various texts for the categories most relevant to the present work. Despite differences across aircraft types, it is clear that there are established guidelines known to lead to stable and controllable aircraft. However, no establish guidelines specific to the design of SSUAVs are available in the open literature.

Table 3.4: Suggested vertical tail volume coefficients from various authors. Table adapted from Barua et al. (2013)

<b>Aircraft Type</b>	<b>Raymer</b>	<b>Roskam</b>	<b>Howe</b>	<b>Schaufele</b>
General Aviation, Single Engine	0.040	0.043	0.050	-
Transport Jet	0.090	0.079	0.090	0.038-0.120
Supersonic Cruise Aircraft	-	0.062	0.065	-
Military Fighter	0.070	0.077	-	0.041-0.130

While these suggested coefficient values are a useful starting point, more can be learned from comparison to specific aircraft with similar configurations to MUFASA. Tail volume coefficient is not typically published as a specification of an aircraft. Wingspan and wing surface area are generally published, while vertical tail area and moment arm can be obtained from geometric analysis of scaled, three-view drawings of aircraft. In *The Anatomy of the Tail*, Gudmundsson (2022a) presents a table of tail parameters for nearly 80 aircraft of various transport roles. Unfortunately, no measurements of supersonic or delta-winged aircraft were included. A cursory review of tail volume coefficients from Gudmundsson (2022a) indicates a positive correlation between increased tail volume coefficient and the potential for thrust imbalance and differential drag due to engine failure. Twin-engine turboprops appear to have the largest vertical tail volumes, along with the BAE-146. The BAE 146 is a quad-engine regional jet (Barua et al., 2013); clearly a large thrust imbalance is possible with an outboard engine shut off and adding to drag. This thrust imbalance is countered by the larger vertical tail of these aircraft, relative to other transport planes.

As with any design decision, tail sizing is a trade-off. The larger the vertical tail or longer the tail moment arm the greater the inherent stability of the aircraft (Ciliberti et al., 2017). An excessively large tail can lead to reduced handling quality for the pilot by over damping any lateral



motion (Nelson et al., 2022). A larger tail also incurs a significant drag penalty. Designers must choose the optimal point which creates adequate stability without excessively penalizing speed and efficiency.

### **3.1.4 Elevon Sizing**

MUFASA derives both roll and pitch control from a single pair of elevons. The detailed sizing of elevons for roll control is a complex endeavour requiring dynamic analysis of forces and moments from control surface deflection (Raymer, 2018). Final sizing in large aircraft must even consider wing stiffness to avoid roll reversal due to wing twisting under elevon/aileron deflection (Pearson and Aiken, 1944). This form of roll reversal is not of concern here due to the short wingspan of MUFASA and the small elevon forces required to roll the low-inertia aircraft. Initial sizing of the elevon surfaces follows historical guidelines, shown in Fig. 3.4, to obtain a first estimate. Further analysis, performed by Dalman et al. (2021) in advance of the present work, was used to obtain the sizes used for manufacture.

The elevons as installed in both versions of MUFASA A.1 are identical in size to reduce the design change work required. On V1 this corresponds to a 9.8% chord ratio (based on MAC) and a 72% span ratio. Changes to the planform kept chord ratio largely unchanged (10.2%) and reduced the span ratio to 61%. Historical sizing guidelines in Fig. 3.4 suggest that these elevons are somewhat undersized, particularly based on chord ratio. Simulations performed indicate that MUFASA A.1 maintains adequate roll authority regardless of the comparison to historical guidelines (Durante et al., 2022). One possible explanation is that the very small roll inertia of the aircraft reduces the need for large ailerons to maintain adequate roll authority (Durante, 2023).

## **3.2 Intake Sizing**

The design of the intake for any aircraft is an important task that can have a large effect on performance (Imfeld, 1974). The intake is by necessity a large frontal surface area to ensure adequate

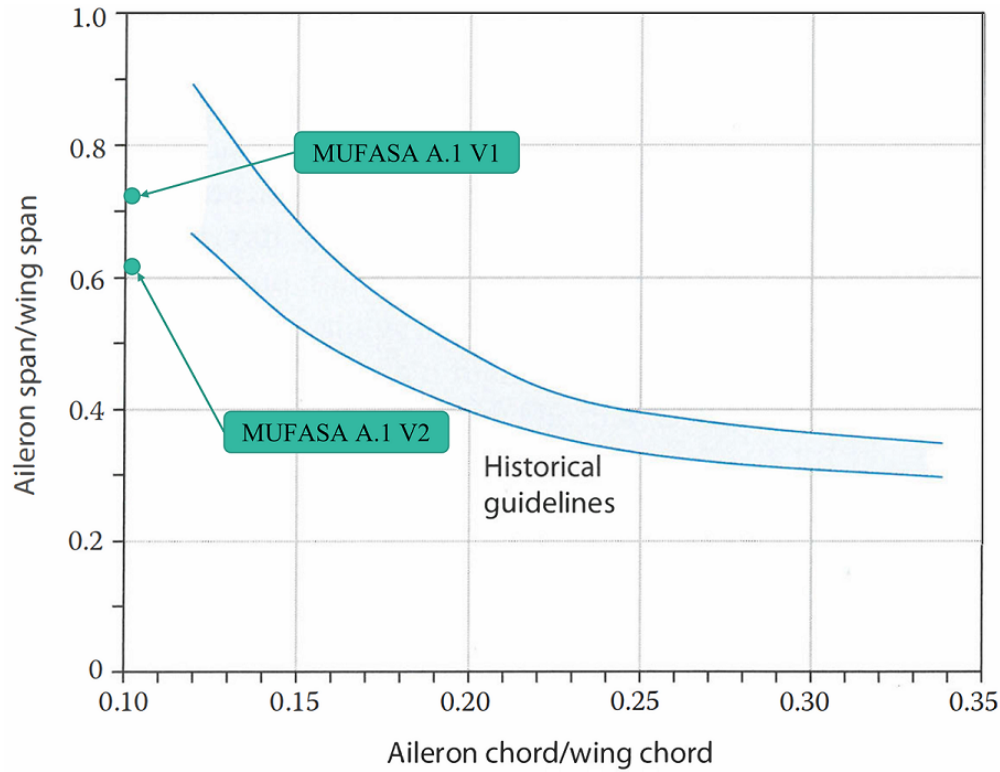


Figure 3.4: Historical aileron sizing guidelines, adapted from Raymer (2018).

air delivery to the engine; this area must also be minimized to avoid an excessive drag penalty. As always, a trade-off must be made to find the optimal performance level. When a gas turbine engine is the propulsion source, consideration must be given to a condition known as a compressor stall (Greitzer, 1980). Compressor stall occurs when an instability in the engine airflow “stalls” all or some of the inlet compressor blades and starves the engine of airflow, resulting in a partial or total loss of power (Sams, 1975). Advances in compressor design have significantly reduced the occurrence of compressor stall in modern engines, however interactions between the intake system and the engine are critical to the performance of the system (Smith, 1996). In the case of an EDF, power to rotate the fan blades is not dependent on sufficient airflow to sustain combustion; the electric motor only requires airflow for cooling. The blades of an EDF can still experience stall and lose the majority of their efficiency if upstream static pressure drops too low (Zhang and Barakos, 2020). As the present aircraft is limited to low subsonic speeds, refinement of the intake design for performance is not completed here. In future, significant effort will be necessary to efficiently

couple a turbojet engine to the pitot intake system and minimize risks such as compressor stall (Cole, 1974).

For conventional jet engines speeds a simple ratio of intake capture area to engine air mass flow rate is provided by Raymer (2018). At subsonic speeds below approximately mach 0.85 this is a constant value of approximately  $0.0051 \frac{\text{m}^2}{\text{kg/s}}$  (square metres of capture area per kilogram of airflow required). Using Rankine-Froude momentum theory formulated for a ducted fan (Gudmundsson, 2022c) the mass flow rate of air in the EDF is estimated to be 0.298 kg/s. Combined with the capture area ratio from Raymer, a circular capture diameter of 44 mm is suggested. Subsequent thrust testing using a nose cone with this inlet diameter showed significant thrust losses that were unacceptable for flight testing. Thrust tests were then performed both with the nose cone removed and with a straight length of pipe to approximate a larger inlet diameter with a similar length to the actual pitot inlet. This testing made it clear that the small inlet diameter was the source of a large portion of the losses. A redesigned nose cone with an inlet diameter equal to the diameter of the bell mouth on the front face of the EDF was manufactured to increase available thrust. This new nose cone would certainly come with a sacrifice to the top speed of the aircraft, however maintaining a rapid development cycle was prioritized over optimization and the larger drag penalty was accepted in order to continue to flight testing as soon as possible. Details of the thrust testing data analysis methods and results are described in Chapter 4.

### **3.3 Construction Method**

MUFASA A.1, the small scale demonstrator of the MUFASA shape, was scaled to minimize the cost and time to manufacture. The method of construction is selected for the same purpose. A rigid foam airframe mimics the construction of hobbyist remote-controlled (R/C) aircraft. By emulating such an established build method, the intent was to remove as much uncertainty as possible from the build process, and to allow for quick changes to the design. The material used to manufacture the airframe is an expanded polystyrene (EPS) foam typically used for insulation

purposes (Plastifab, 2019). This material was chosen for a number of reasons, largely related to availability and material performance:

- Readily available in custom-sized blanks for CNC milling of components.
- Locally manufactured to minimize lead time and uncertainty due to global supply chain challenges.
- Highly machinable with quality CNC router tooling.
- Readily accepts a variety of adhesives and coating options for finishing operations.
- Extremely lightweight and durable.

The highly machinable nature of the EPS foam was confirmed by a series of test cuts in a sample block provided by the supplier. Cuts were made on a CNC router with extremely sharp tooling, a high rotational speed, and sufficient feedrate to cut thicker chips instead of shavings. The machining strategy is informed by the structure of EPS foam, and the mechanisms of material removal. EPS foam consists of small beads of polystyrene packed together; mathematical models typically approximate these beads as hexagonal cells (Jose Angel et al., 2013). Two methods of removal exist when machining the foam: bead removal and bead transsection (Gote et al., 2022). Bead removal occurs when sufficient friction is present on the cutting implement to tear the bead away from its neighbours. From simple test cuts with both used and new tooling it was observed that new tooling left a significantly smoother surface finish and effectively eliminated bead tear-out. Worn tooling with a less keen edge tended to tear beads away from the parent material instead of cutting cleanly through. It was also observed that higher rotational speeds and a higher feedrate (resulting in thicker cut chips) left a smoother surface finish. Figure 3.5 illustrates the achievable surface finish of a machined EPS component with the selected machining parameters. Feed rate and surface speed are shown, 1375 ft/min surface speed corresponding to 21000 rpm with a 0.25 inch tool diameter fed at a rate of 0.004 inches per flute. The depth of cut (axial engagement) was set to match the length of flutes on the tool to maximize material removal rate (MRR); the soft EPS foam results in very small spindle loads and poses no risk of tool breakage. Material removal rates

up to 60 cubic inches per minute were achieved. For comparison, an MRR of 9 cubic inches per minute is typical for mild steel (Kalpakjian and Schmid, 2009).

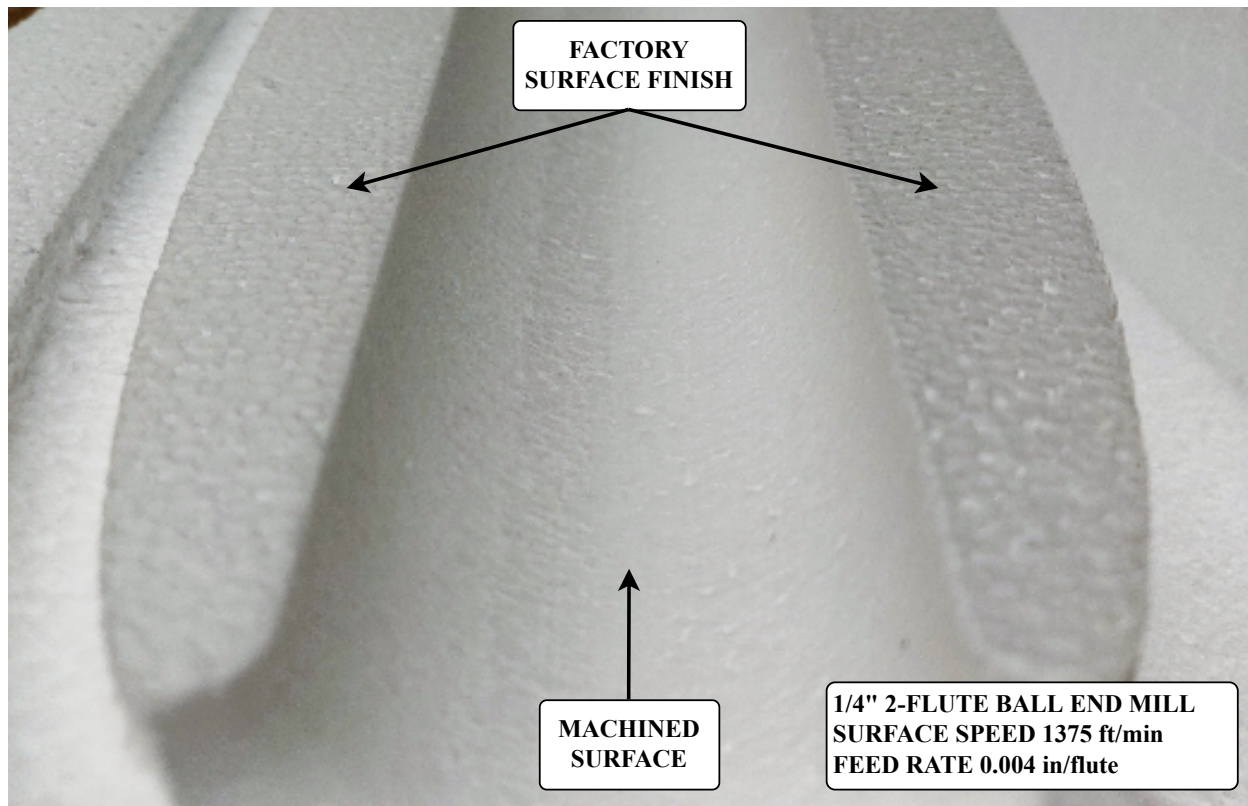


Figure 3.5: Detail of EPS foam machined surface finish and factory surface finish. Contrast enhanced to highlight bead boundaries.

The ease of bonding and finish-coating the foam was also considered when selecting the material. Water-based clear polyurethane (PU) coatings proved ideal for finishing exposed surfaces. The PU product was very easy to apply with no runs or drips, posed no environmental or safety hazard, and sanded smooth with minimal effort. The very low viscosity of the coating allowed it to impregnate a short distance below the surface of the component, increasing hardness and durability. Attempts with epoxy coatings typically resulted in runs and drips in the finish, and the epoxy was too viscous to penetrate into the porous EPS surface. The epoxy required significantly more effort to sand away imperfections, and added significantly more weight to the assembly than the thinner PU coating. Similarly, the ability to adhesively bond foam components to each other

and to 3D printed plastics was important to consider. Adhesive bonding with many thermoplastic materials is particularly difficult due to their non-porous nature and the poor wettability of plastics (Chawla, 2012; Kalpakjian and Schmid, 2009). This issue was more critical when considering the 3D printed plastic side of the bond as the strength of the epoxies exceeded the strength of the EPS parent material. A qualitative test of a bond between EPS foam and a 3D printed PETG component was conducted early in the material selection process. Using only moderate surface cleaning and a plastic-specific epoxy, the resulting bond was significantly stronger than the EPS. As shown in Fig. 3.6, the joint did not fail at the bond line, rather it tore away a layer of the foam parent material. This bonding characteristic, coupled with the performance and ease of application of the water-based PU coating, supported the foam construction method as optimal for this prototyping application.



Figure 3.6: Post-failure image of bond strength test between EPS foam to 3D printed PETG.

Rapid implementation of design changes in the final assembly was a key factor in choosing EPS foam construction. Where a more typical UAV prototype might use carbon fibre composites for the airframe, CNC-carved foam does not require a complete new set of lay-up moulds when a small design change is made. The cost of manufacturing a prototype from carbon fibre or similar composite materials is significantly higher than the foam construction used here. The cost of the foam is approximately the same for both options; a composite airframe requires negative-space moulds of the same size as the positive-space components. An early estimate concluded that the materials cost for a carbon fibre airframe would be approximately \$2000, assuming minimal wasted material and the use of existing equipment such as vacuum bagging pumps (Gair et al., 2019). By contrast, the foam cost for a single airframe was approximately \$100. While a carbon fibre airframe would be significantly more durable than the chosen foam option, the additional cost and manufacturing lead time outweighed the durability advantage. The overall project would benefit most from a rapid development cycle.

A final key factor in selecting EPS foam construction for the prototype was airframe weight. Initial estimates of the mass of a carbon fibre airframe were calculated from basic surface area parameters. Assuming a hollow carbon fibre airframe with no internal reinforcement, the airframe can be broken into components of fuselage and wings to estimate the amount of carbon fibre fabric required to form a skin. Using typical values for the areal weight of CF fabric, fabric-epoxy ratio, and a common quasi-isotropic 4-ply layup (Chawla, 2012) the airframe would have an estimated mass of 1.68 kg. With a goal 2.5 kg for the takeoff mass of the aircraft it is simply not feasible for the empty airframe to consume more than two-thirds of the mass budget. By comparison, the foam-only airframe has an estimated weight of just 0.58 kg from the computer-aided design (CAD) model with appropriate material properties applied. This extreme lightweight construction is critical to the present prototyping phase. A lower weight translates into a lower takeoff and stall speed (Anderson, 1999) and thus a greater chance of a successful flight test. Table 3.5 shows the mass and construction method of each airframe structural component. The following section describes how the aerodynamic shape was divided into elements for manufacture.

Table 3.5: Mass of manufactured airframe components

Component	Material	Mass
Nose Cone	EPS	149.5 g
Fuselage Assembly	EPS	302.3 g
Avionics Panel	EPS	14.3 g
Main Panel	EPS	104.2 g
Trailing Edge Caps (each)	PETG	56.2 g
Elevons (each)	PETG	14.7 g
Vertical Stabilizers (each)	EPS	13.2 g
Verticals Servo Mounts (each)	PETG	8.3 g
EDF Mount	PETG	7.0 g

### 3.3.1 Division into Structural Elements

When considering options for material and manufacturing method it is important to think ahead to the limitations of the methods under consideration. The most obvious limitation of the chosen foam construction is the 3-axis CNC router available for use. The cutting tool is constrained to a vertical orientation and can only remove material from the top of the workpiece. Additionally, the length of commercially available cutting tools is limited. Considering the long internal channel and pockets making up the pitot intake and battery compartments, it was clear that a single component construction was not possible. The 3-axis movement and tooling length limitations were resolved by bisecting the airframe into upper and lower halves for machining separately. This allows the internal features to be machined in the first operation, then the stock flipped over and located on the flat mid-plane surface for machining of external features.

The requirement for easily replaceable parts posed a more significant challenge. Ideally, both the wings and the nose cone would be field-replaceable. The nose cone is split from the main fuselage body where the taper of the nose cone meets the straight cylinder of the fuselage (see Fig. 3.7). A step is cut into the foam to locate the two parts together with a friction fit to ensure accurate alignment. Thus, the nose cone is manufactured in upper and lower halves to permit machining of the internal features and then attached to the fuselage with a friction fit and tape for field-replaceability. By making the nose cone so easy to replace and quick to manufacture, the



nose cone can be considered a deliberately sacrificial part. In the event of a loss of power in-flight it would be preferable to guide the aircraft in nose-first. The nose cone would deform to absorb the impact energy, thereby protecting the majority of the airframe and the fragile electronics and batteries. The fuselage is likewise split on the mid-plane for machining in the same manner as the nose cone. Upper and lower halves are then permanently mated together with a foam-safe spray adhesive to form a solid component with all necessary internal features. Included in the machined fuselage halves are dowel holes to assist in accurately locating the two pieces relative to each other. The general process for creating, splitting, and machining the foam components is laid out below. The components are shown in Fig. 3.7 in an exploded view and Fig. 3.9 as-assembled.

1. Generate complete airframe 3D model including internal features in CAD program.
2. Split model into upper and lower halves on the mid-plane in CAD model.
3. Split apart nose cone, avionics access panel, and main access panel.
4. Machine internal features of the component.
5. Flip stock with cut internals over, locating the part on the mid-plane surface.
6. Re-reference CNC machine to align internal and external component features.
7. Machine component external features to completion.
8. Permanently bond together upper and lower nose cone halves and fuselage halves.

The concept of field-replaceable wings was explored early in the design maturity. With thin cross-sections near the tips, the wings are clearly vulnerable to damage in the event of a crash or even a rough landing. A typical aircraft with wings made separately from the fuselage features a carry-through spar to transmit loads between the two wings (Megson, 2007). In the case of MUFASA A.1, a standard spar would inevitably interfere with airflow in the intake. The addition of a non-straight spar to work around the intake while also carrying loads between wings would have added significant complexity to the design, both in analysis and manufacture. Assuming that a sufficiently strong and manufacturable spar was designed to accommodate the intake, the

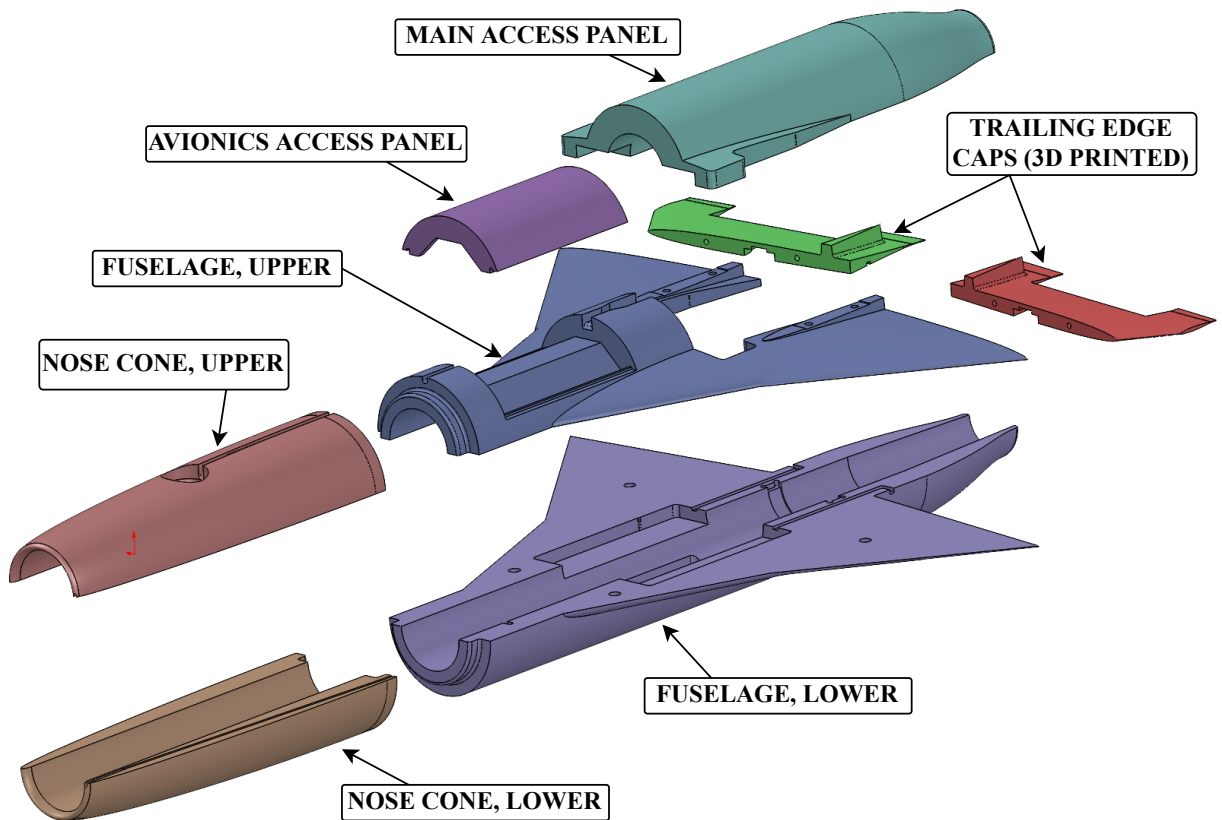


Figure 3.7: Exploded view of airframe components. All parts shown are EPS foam except where noted.

challenge of rigidly and accurately affixing the wings to the fuselage remains. A minimum of two attachment points is necessary to fully constrain the wing, three would be preferable given the long chord length where the wing root meets the fuselage. A simple method can be found on large-wingspan UAVs such as the Skywalker X8 (UAV Systems International, 2022) used by the author and colleagues for avionics testing and flight test training. Shown in Fig. 3.8, two carbon fibre tubes pass through the fuselage and into each wing. The spars mate to reinforced holes in the wings; inserting the spars into bare foam holes repeatedly would cause the foam to compress and the holes to become oversized, resulting in wing misalignment.

Already the removable wing system has taken the fuselage structure from two machined components (upper and lower fuselage halves) to six; upper and lower halves of both wings and the

fuselage. Then a system must be designed to retain the wings on the spars, tight to the fuselage. To preserve the aerodynamic shape being tested there should not be any mounting features exposed to the airflow over the wings, an added constraint which further increases complexity. After considering the options for potential structural designs for removable wings it was decided that the additional challenges stemming from the design, manufacture, and validation testing of the removable wing concept were not worth the increased cost, time, and uncertainty. The simplicity of only two fuselage halves with integral wing sections was chosen as the preferred option.



Figure 3.8: Fuselage and wing components of the Skywalker X8 commercial UAV, showing the wing attachment spars running directly through the fuselage. Image from SpexDrone (2023)

### 3.3.2 Thin Sections

While the EPS foam material is a strong choice for the bulk of the airframe, it has limitations near the trailing edge where the wings become extremely thin. In this area there are additional stresses placed on the structure from the attachment of the elevon servo, elevon hinge, and vertical stabilizer servo. There is the additional challenge of mounting the servos to the foam wings, along with the hinge line of the elevons. The hinge line is not located directly on the surface nor on the mid-plane of the wing (Gair et al., 2020), further complicating the installation. These features make the parts very difficult to manufacture manually or with CNC-cut foam. 3D printing was an obvious solution for accurate manufacture of components with complex geometry. Fused-filament fabrication (FFF) 3D printing is a technology enables fast, accurate manufacture of complex geometries including thin sections (Dudek, 2013). It is relatively inexpensive, simple to learn, and can incorporate all of the required geometries into a single component. The trailing edge caps are 3D printed from polyethylene terephthalate glycol-modified (PETG) as a single piece then permanently bonded to the main fuselage/wing assembly with epoxy. Dowel holes are incorporated in the design to assist in maintaining alignment while the epoxy cures. See Fig. 3.7 for an illustration of the 3D printed trailing edge caps.

The choice of PETG for 3D printed parts was informed by discussion with experienced individuals and basic research into the mechanical properties of common 3D printing materials. The most common and least expensive material is polylactic acid (PLA). It prints easily with relatively low temperatures, but is relatively brittle and prone to cracking under deformation (Ngo et al., 2018). Two similarly available and inexpensive alternatives were available, PETG and acrylonitrile butadiene styrene (ABS). ABS is commonly found in plastic automotive panels and water/sewer pipes (Olabisi and Adewale, 2016). PETG is similar to the PET used in disposable plastic water bottles, but with chemical alterations to lower melting temperature and crystallization to improve performance in heated operations such as thermoforming and 3D printing (Guessasma et al., 2019). ABS is known to be more difficult to print from its tendency to warp (Ramian et al., 2021), and carries potential health hazards from volatile organic compounds (VOCs) and particulates emitted during

printing (Ryan and Hubbard, 2016). Hazards associated with 3D printing of PETG are significantly lower (Wojnowski et al., 2022). For these reasons, PETG was chosen as the preferred material for the trailing edge caps and other small airframe components.

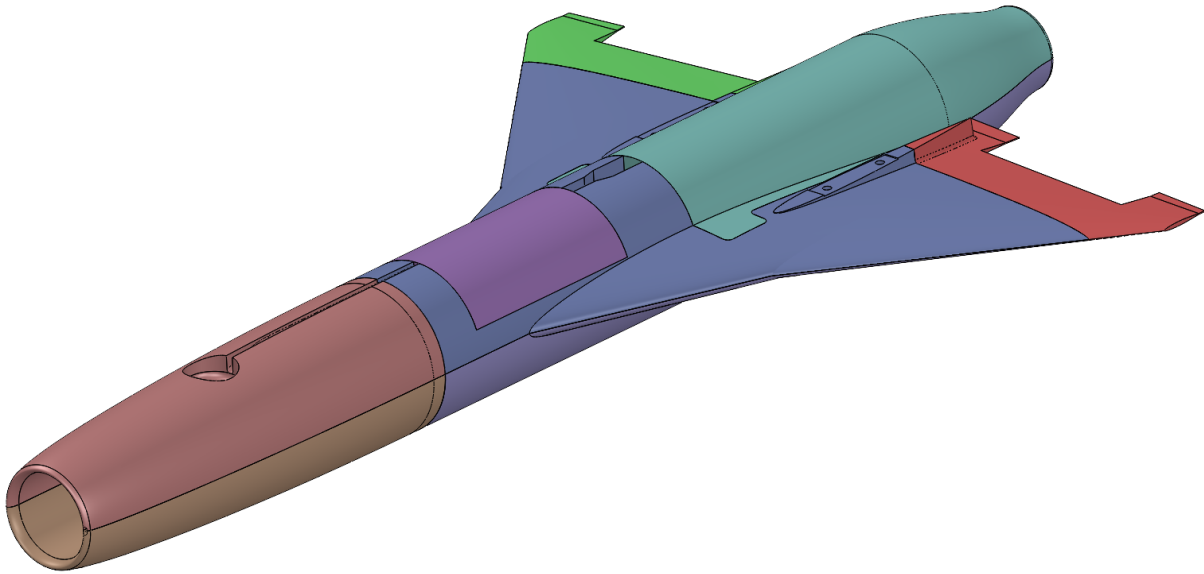


Figure 3.9: Airframe structure consisting of individually machined EPS foam components and 3D printed trailing edge caps in green and red.

### 3.3.3 3D Printed Components

In addition to the thin sections described above, certain components of the airframe were 3D printed. Any components attached with threaded fasteners (i.e. control servos) would be difficult to secure directly to the foam airframe. In these locations a 3D printed bracket was designed to provide a large surface area for adhesive bonding to the airframe while accepting the threaded fasteners necessary to attach the component. The EDF and vertical tail servos were both mounted in this manner. The elevon servos were also attached with threaded fasteners, but their mount was integrated directly into the 3D-printed trailing edge caps and not a separate component.

### 3.4 Version 2 Design Refinements

Following the first set of flight attempts, described in Section 5.2, it was clear that the present state of the design was not likely to lead to sustained, stable flight. Analysis of video recordings and flight computer data prompted the conclusion that the required takeoff speed was too high. Most of the changes made were intended to reduce the minimum flight speed. For clarity, the airframe first flight tested in March 2022 is known as MUFASA A.1 V1. After design refinements were made the second airframe manufactured for flight testing became known as MUFASA A.1 V2. For brevity they will simply be referred to as 'V1' and 'V2' in this document.

One of the main challenges experienced related to the relatively high required takeoff speed. Estimates of the minimum control speed provided by Dalman et al. (2021) and Durante (2023) show that the aircraft should be able to maintain steady, level flight at  $10^\circ$  AoA at a speed of approximately 22 m/s. Potentially lower speeds could be achieved with additional power given the delayed stall characteristics of the delta wings; simulations showed that the EDF used here did not have enough thrust to maintain speed at AoA greater than  $10^\circ$ . This high takeoff speed is exacerbated by any increase in aircraft weight (see equation 3.8 below). Given the known challenges of controllability at low speeds (see Section 3.1.3) minimizing takeoff speed became an important goal.

$$L = C_L(0.5\rho V^2)S \quad (3.8)$$

For steady flight, the lift  $L$  generated by the aircraft must equal its weight, governed by the lift coefficient  $C_L$ , air density  $\rho$ , square of the velocity  $V$  and wing area  $S$ . For a given aircraft at a given AoA both lift coefficient and wing area are fixed; only reducing mass can reduce velocity required.

The first change made was to decrease the weight of the aircraft. Since ballast was required to locate the CG for suitable static margin, eliminating the need for ballast was an obvious goal. Feedback from the pilot suggested that active yaw control was not necessarily required for this air-

craft. Review of commercially available R/C aircraft and published literature agreed that sufficient control was possible with fixed vertical stabilizers and no rudder (Mitikiri and Mohseni, 2018; Stenfelt and Ringertz, 2009). Fixing the verticals in place eliminated the servo motor controlling each of the verticals, a total of 132 grams for approximately 5% weight savings. The location of these servos, aft of the neutral point of the aircraft, served to shift the centre of gravity forward at the same time, further reducing the need for ballast.

To further reduce the required takeoff speed and shift the neutral point aft, some minor changes were made to the planform. The wingspan was increased by approximately 15% from 663 mm to 760 mm and the trailing edge forward sweep angle reduced from  $-17^\circ$  to  $-6^\circ$ . This has the dual effect of increasing planform area for lift generation and shifting the aerodynamic centre of the planform further aft. The planform area increased by 13.7% as a result of these changes. A simple approximation of lift, holding all other values constant in Eq. (3.8), indicates that the larger planform should reduce velocity required by 7%. These planform changes can be seen in Fig. 3.10.

The change in location of the aerodynamic centre can be approximated using the change in mean aerodynamic chord. In subsonic flight, the aerodynamic centre can be reasonably approximated as one-quarter of the way along the MAC, usually termed 0.25MAC (Gudmundsson, 2022b). The MAC for V2 is shorter than for V1 by 15.7 mm, however it is located further outboard on the wing and therefore further aft, moving the aerodynamic centre aft by 35.2 mm. This affects longitudinal stability by altering the reference point for calculating static margin - the aftmost allowable CG location moves with the aerodynamic centre.

The final change made to the airframe to assist with CG location was to shift the battery mount location. Some minor geometry changes were made to the model which allowed the batteries to be mounted 5 mm closer to the nose of the aircraft. The batteries are the single heaviest component in the aircraft, each one weighing nearly as much as the bare fuselage assembly. They can be mounted anywhere in a range of locations along the longitudinal axis of the aircraft to help with positioning the CG.

A summary of the changes made for the V2 aircraft is provided in Table 3.6. The result-

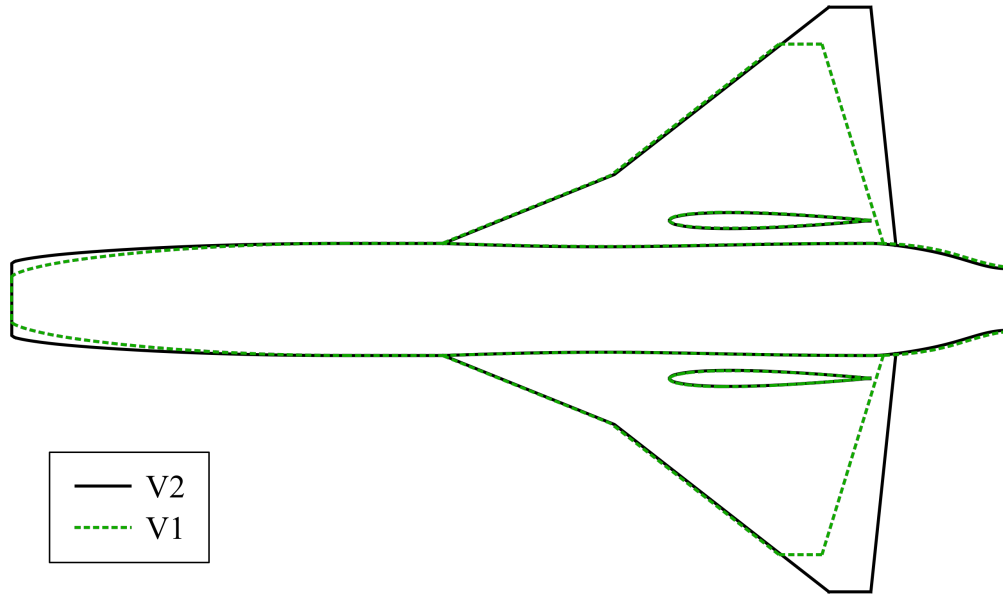


Figure 3.10: Comparison of V1 and V2 wing planforms. Note that the V1 planform is shown with the original small intake not used in flight testing.

Table 3.6: Summary of changes to MUFASA A.1 from V1 to V2.

Parameter	V1	V2
Wingspan	663 mm	760 mm
Trailing Edge Sweep	-17°	-6°
Planform MAC	461 mm	443 mm
Planform Area	0.241 m <sup>2</sup>	0.274 m <sup>2</sup>
Vertical Stabilizers	Active Movable	Fixed
Minimum Control Speed (est)	22 m/s	19 m/s
Battery Mount	Shifted 5 mm forward	
Flyaway Weight	2480 g	2281 g

ing aircraft with these changes implemented was approximately 8% lighter despite increasing the wingspan and planform area. The weight savings came from removing the ballast weight (131 g) required and removing the two servos driving the vertical tails. With the increased wing area, lighter aircraft and thus reduced minimum flight speed, the refined V2 aircraft has an improved chance of successfully achieving stable flight.



# **Chapter 4**

## **Ground Testing & Results**

Ground testing of aircraft systems prior to flight is a key step in building towards first flight. The relative simplicity of the MUFASA A.1 systems and use of commercially-available components reduces the complexity of the testing required. Quantitative testing was conducted on the engine to ensure that adequate thrust was available for flight. Function checks were conducted on all electronics and control servos as the components were received to verify their operation. These minor checks were conducted as part of the engine thrust testing campaign as most components to be checked were also required for thrust testing.

### **4.1 Electronics Function Checks**

Function checks of the avionics systems on the aircraft ensured that each component was correctly installed and configured. Prior to thrust testing the electronics were all installed in the airframe as if for flight testing. The batteries were connected and the 900 MHz wireless connection established to the ground station computer. The wireless connection between the aircraft and ground station enabled real-time monitoring and adjustment of all sensors and parameters. Once established, the remaining function checks could be performed.

The air data sensor was connected to the pitot tube in the nose cone and compressed air blown across the pitot port to ensure that the pressure change was registered by the software. Without

in-flight calibration the pitot tube will not accurately measure airspeed; a check of the function is all that can be completed at this stage. Alternative methods of airspeed sensor calibration were not considered as airspeed is not required for early controllability evaluations.

Moving the completed assembly outside allowed the GPS module to establish a satellite signal. GPS accuracy level is quantified by the horizontal dilution of precision (HDOP) (Specht, 2022). HDOP is a measure of the quality of a GPS location signal dependent on many factors, with a lower number indicating a better position fix. Ardupilot documentation specifies that an HDOP less than 2 is sufficient for flight (ArduPilot Dev Team, 2023).

Control servos were connected to the Durandal flight controller for range of motion and orientation checks. Because the elevon servos are installed in mirrored orientations, the command signal to one must be reversed in the software configuration. In the V1 aircraft with movable vertical tails the range of motion of the vertical stabilizer servos was electronically limited to  $\pm 5^\circ$  to prevent contact with the fuselage. Control commands from the pilot's transmitter were compared with control surface deflections for orientation and range of travel. The elevons demonstrated a range of  $\pm 40^\circ$ , varying linearly with PWN signals from 1250-1750  $\mu\text{s}$ .

The radar altimeter was tested simply by holding the airframe level at a known distance above the ground and comparing the actual distance to that measured by the sensor. Measurements at close range ( $<1$  m) and medium range ( $<10$  m) both showed sufficient accuracy to deem the radar altimeter to be functioning as expected.

With the completion of electronics function checks, quantitative thrust testing of the EDF could then be completed to experimentally determine available thrust for flight testing.

## **4.2 Engine Thrust Testing**

Following the selection and purchase of the EDF (electric ducted fan) for propulsion of MUFASA A.1 it was necessary to complete baseline performance testing. Testing of the actual thrust output of the EDF is useful for comparison to the manufacturers claimed data, as well as for improving

estimates of in-flight drag. Results can also be used to inform future EDF selection decisions; if the present model of EDF produces only a certain percentage of the claimed thrust it is reasonable to conclude that other models from the same manufacturer are likely to similarly under-perform.

Any differences between the claimed or rated thrust and measured thrust are could be the result of various factors. The first is the air density where tests were conducted; at local altitude air density in Calgary is approximately 12% lower than at sea level. If manufacturer tests were conducted at or close to sea level the additional air density will result in a higher thrust rating (Gudmundsson, 2022c). The use of different control electronics from the manufacturer when testing was performed could affect the power available to the motor. Varying conditions such as temperature of the batteries and ambient air density could impact performance. Geometry affecting airflow at the inlet and outlet of the fan would also have a substantial effect on thrust output. It was observed early in the testing cycle that significant losses were occurring due to the long intake of the aircraft. Analysis of these data prompted the increase in the nose cone inlet diameter discussed in Section 3.2.

In lieu of a more conventional approach to a thrust test setup using a hanging or floating frame with load cells, a simple hanging pendulum was used to measure engine thrust (Runyan et al., 1992). Cost and complexity were minimized by eliminating measurement electronics with the exception of a digital camera to record video. The aircraft and engine test rig were suspended from a frame using brightly coloured string. The string used was light and flexible enough to impose no restriction on the movement of the hanging test setup and therefore introduce as little error as possible. For a test rig of a known mass, calculation of thrust produced is simple when the deflection angle of the string is measured. Thrust produced is the weight of the test rig in Newtons multiplied by the tangent of the deflection angle of the string relative to vertical as shown in Fig. 4.2. In Fig. 4.1 the pair of strings in a V-shape at the front of the aircraft are visible, providing stability, while the single rear string is vertical and used to measure angular deflection.

Using the video recording from each test run it was possible to obtain a continuous measurement of the thrust produced throughout. A Matlab program was written to process the video frame-by-frame. In each frame the pixels containing the string were identified by RGB colour

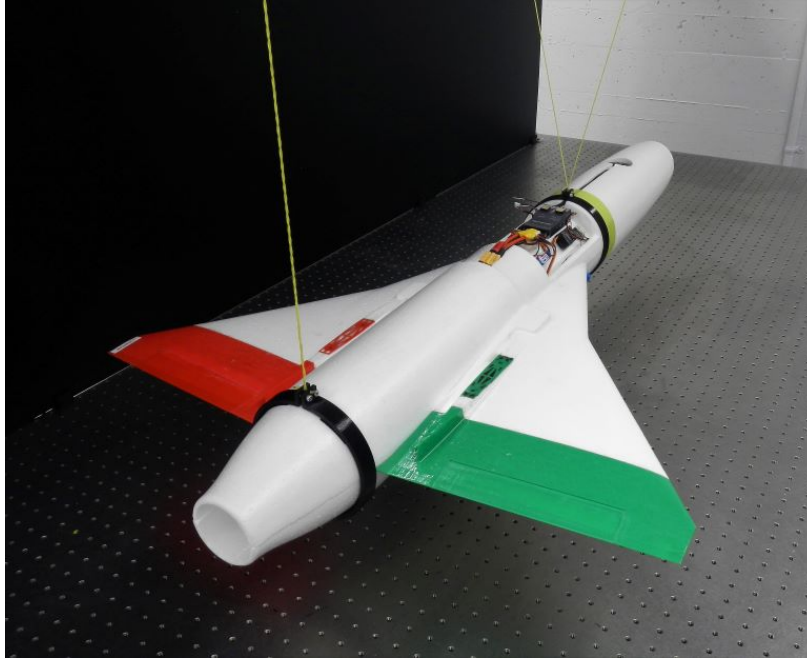


Figure 4.1: Image of static thrust test setup showing strings suspending the aircraft.

values and a linear line was fit to those pixel locations. The slope of that line gave the angle of deflection and thus the thrust produced. Continuous monitoring of thrust was advantageous in that small variations over a long period of time could be observed. For example, whether thrust remained constant over the life of the batteries was of interest. Lithium-polymer (LiPo) batteries typically maintain a relatively constant voltage during discharge with a sharp decline near complete discharge, however efficiency can vary with temperature (Salameh and Kim, 2009). Heating of the batteries during discharge could cause a decline in power over the duration of a flight.

While not indicative of in-flight thrust where there is a non-zero forward airspeed, static thrust curves are useful for flight simulations and can assist with estimating aircraft drag and maximum airspeed (Durante, 2023). Two main tests were conducted related to engine thrust. First, the EDF was set to throttle levels from 0 to 100% in defined increments to develop a basic thrust curve correlating throttle setting in PWN (pulse width modulation) signal to static thrust. The second test was a maximum run time test while measuring peak thrust. This was used to ensure that the aircraft's peak available thrust would not diminish significantly near the end of a flight. If, as batteries neared empty the available thrust were substantially reduced the pilot may not have

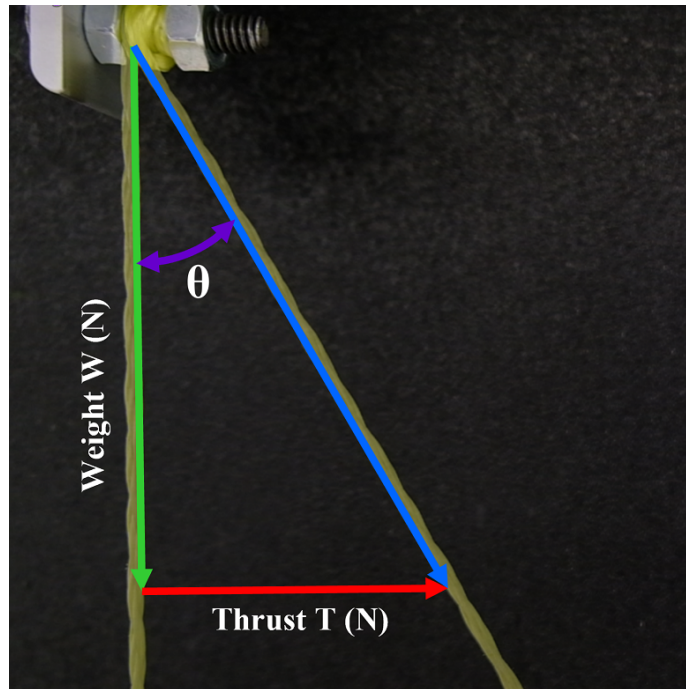


Figure 4.2: Video frame from thrust testing using string angular deflection.

the ability to safely abort a landing. Battery temperature was monitored for a number of rapid discharge tests to ensure that temperatures did not exceed manufacturer specifications.

Figure 4.3 shows the thrust curves for each test. Thrust values for each step of the ramp-up to full throttle are given in Table 4.2. The thrust curve of test 2 shows the overall loss of thrust due to decreasing battery level and temperature build-up in the electronics. Over the course of 135 seconds the static thrust output dropped by 0.75 N. The batteries reached a maximum of 48°C; maximum operating temperature for LiPo batteries is typically given as 60°C (Common Sense RC, 2017). The test was ended with approximately 10% battery remaining to protect the batteries from an under-voltage condition. The ramp up to maximum throttle for each test shows good consistency between the two test runs; repeating the same throttle setting reliably reproduces the same amount of thrust. Initial overshoot at each throttle level is due to momentum carrying the plane past equilibrium on the string. After each throttle increase the plane was steadied by hand to give the most stable reading possible. A 100-point moving average was applied to the raw data thrust data to remove excessive high-frequency noise from vibrations and inaccuracies in determining string

position.

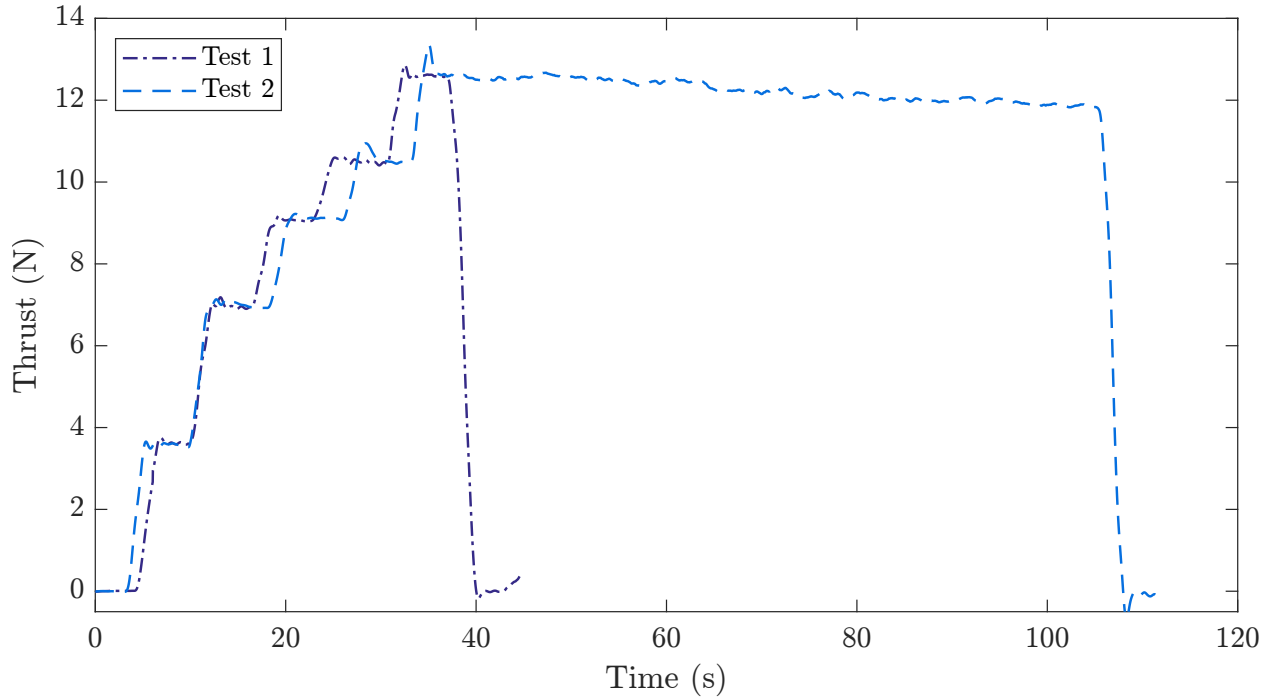


Figure 4.3: Static thrust test curves for MUFASA A.1 V1, EDF as installed in airframe, 83 mm inlet.

Table 4.1: Measured static thrust for EDF installed in flight configuration.

Throttle Setting [%]	Thrust Measured [N]	
	Test 1	Test 2
0	0.01	0.00
20	3.65	3.58
40	6.93	7.01
60	9.06	9.12
80	10.50	10.49
100	12.59	12.60

## 4.3 Discussion

Static testing performed on the EDF showed a significant measured thrust deficit when compared with manufacturer claimed values. There is no remedy to this issue apart from purchasing a larger

EDF with the understanding that it will likely underperform manufacturers expectations. Analysis here is instead focused on the losses incurred by the long pitot intake used in the aircraft design.

Thrust test results in Table 4.2 compare each tested configuration with the bare engine and the manufacturer's claims. As the thrust losses due to the pitot intake are of interest, values are shown with a percent difference to the bare engine instead of to manufacturer's specifications. The original nose cone had a 45 mm diameter inlet, sized using capture area methods from Raymer (2018) and detailed in Section 3.2. Thrust losses of 40.5% were observed in this configuration with a maximum of 9.7 N thrust produced. A nose cone with a larger capture area was manufactured and tested with an 83 mm-diameter inlet. This inlet size matches that of the bell mouth of the EDF. Thrust losses of 22.7% were observed with a maximum recorded thrust of 12.6 N. This marks a significant improvement over the original nose cone design, but remains a large source of lost thrust.

The measured maximum thrust gives the aircraft a thrust to weight ratio ( $T/W$ ) of 0.52-0.56, depending on takeoff weight. While lower than initially intended, this ratio falls between values for a typical transport aircraft ( $T/W = 0.25$ -0.3) (The Boeing Company, 2019) and a typical fighter jet such as the F-22 Raptor ( $T/W = 0.62$ ) (Malloy et al., 2002). Simulations showed that the thrust deficit resulted in a reduced top speed but minimum control speeds remained acceptable (Durante, 2023). The decision was made to proceed with flight testing and leave a comprehensive pitot intake design to future work.

The precise cause of losses in the intake has not been positively identified. Possible sources of loss for a subsonic intake condition include inlet separation and duct friction (Goldsmith and Seddon, 1993). Inlet lip separation occurs when an incident flow must turn sharply around a thin-lipped inlet into the diffusing section (Goldsmith and Seddon, 1993). Separation is unlikely at the lip of the MUFASA intake as there is no diffuser section. Approximately halfway along the intake, where the batteries are located, separation is almost certain to occur. Where the geometry opens up to provide space for wiring and battery installation there is effectively a step diffuser on the sides of the inlet (see Fig. 3.7. Separation occurring at this location accounts for a portion of the inlet

losses.

The second source, duct friction, is unavoidable for any intake design. Friction along the walls of the inlet duct is mainly dependent on the mass flow rate of the air and the surface roughness of the inlet (Seddon and Goldsmith, 1999). For a short inlet with a large fan diameter (e.g. nacelle-mounted engines on transport jets) frictional losses will be much lower than for an intake that is many fan diameters long. These frictional losses could be reduced for the present design with careful treatment of the inlet components to improve surface roughness.

Importance was placed on the continued timely build of the aircraft for flight testing. Future work to more closely examine and mitigate thrust losses in the pitot intake will be essential to maximizing performance in future flights. A design with more available space could provide a pitot intake uninterrupted by wiring and battery components. Changes to construction methods could also improve the surface roughness of the inlet, significantly reducing frictional losses. A series of experiments using various inlet lengths with differing surface finishes could be used to isolate the sources of loss for the present configuration and inform future development.

Table 4.2: Measured static thrust for small and large intakes compared with manufacturer data.

<b>Configuration</b>	<b>Inlet diameter [mm]</b>	<b>Inlet length [mm]</b>	<b>EDF thrust [N]</b>	<b>Difference to adjusted value</b>
Manufacturer claimed	-	-	23.0	14.1%
Manufacturer, adjusted for altitude	-	-	20.2	-
Bare engine (bell inlet)	83	0	16.3	-19.3%
Original nose cone	45	964	9.7	-52.0%
Enlarged inlet mouth	83	964	12.6	-37.6%



# **Chapter 5**

## **Flight Testing & Results**

The culmination of the design and prototype-build process of any aircraft is the first flight. Two flight days with five total flight attempts make up the testing completed with MUFASA A.1. Version 1 (V1) attempts occurred in late March 2022 with two launches. Version 2 (V2) attempts occurred in early October 2022 with three launches. None of the attempts resulted in sustained, stable flight. Data collected in flight nonetheless provides valuable insight into the behaviour and controllability of the aircraft. Insufficient lateral stability and asymmetric wing stall exacerbated by control surface deflection are discussed in detail in Section 5.4 as key outcomes of the flight test data.

### **5.1 Flight Test Plan**

The flight test plan for the MUFASA A.1 aircraft was developed to ensure that data gathered would inform future work in developing design procedures for SSUAVs and refining the MUFASA aircraft in particular. The challenges associated with SSUAV development discussed in Section 2.2.1 help to guide the goals of the testing plan with respect to data collection and flight maneuvers. As the onboard flight controller automatically records all sensor data and parameters for each flight, careful selection of the specific analysis variables was not required prior to flight. The main requirement was determining which flight maneuvers were necessary to collect as much relevant data

as possible.

Before completing data gathering maneuvers, the autopilot system requires tuning to enable it to accurately and reliably fly the aircraft. Tuning flights in general consist of the pilot repeatedly oscillating the plane about a single axis of motion while the autopilot module “listens” to the response relative to the inputs provided. It uses this time to adjust the PID (Proportional-Integral-Derivative) controller gains to match the system (aircraft) being controlled. Table 5.1 lists the tuning flights required to correctly calibrate the autopilot for control of MUFASA A.1, drawn from the Ardupilot documentation (ArduPilot Dev Team, 2023). A significant challenge in tuning MUFASA A.1 stems from the very short flight time. To ensure adequate remaining battery life for landing, each flight is limited to 3 minutes. Where a more typical R/C aircraft with 20-30 minutes of endurance could complete tuning in a single flight, MUFASA A.1 requires a minimum of six flights. The final flight listed is a complete test of the autopilot system additional to what is recommended; a successful return to launch (RTL) command with the aircraft circling overhead is considered the end of tuning according to the the Ardupilot documentation (ArduPilot Dev Team, 2023).

Table 5.1: Summary of flight computer parameters collected for further analysis.

Flight	Tuning Purpose	Description
1	No tuning	Pilot feedback - controlability
2	Calibrate airspeed sensor	Fly circles
3	Autotune, roll	Rock wings
4	Autotune, pitch	Porpoising (nose up-down)
5	Autotune, yaw	Side to side inputs
6	Verify tuning	Activate RTL - plane to circle overhead
7	Complete autopilot test	Execute autonomous mission - T/O to landing

From the list of hundreds of parameters and variables that the autopilot system records (ArduPilot Dev Team, 2022), the twelve listed in Table 5.2 are of primary interest. They include the inputs from the pilot’s controller, outputs to the servos, GPS data, and various parameters related to aircraft attitude and speed. The data rate varies by parameter. GYR and ACC are gyroscope and accelerometer raw signals, respectively. They capture minute changes in aircraft attitude but are

also susceptible to high frequency noise, mainly from engine vibration. For this reason the Duralandal unit is supplied with specialized mounting pads which limit vibrations transmitted from the airframe to the inertial measurement unit (IMU). Collected GYR and ACC raw signals at 2000 Hz are also filtered internally by the IMU chip (TDK InvenSense, 2021) to remove sensor noise. Filtered gyroscope and accelerometer outputs are then passed to the extended Kalman filter (EKF) at a rate of 50 Hz. A thorough treatment of the operation of an EKF is outside the scope of this work (Ribeiro, 2004). In general, a Kalman filter is a mathematical formulation that combines information from multiple sources to determine the state of a system, also called a linear estimator. An *extended* Kalman filter is a version used to apply similar techniques to a nonlinear system such as an aircraft in flight (Kobayashi et al., 2005). The EKF combines data from the IMU, GPS, airspeed, magnetic compass, and barometric pressure sensor to provide the best possible prediction of the state of the aircraft at a rate of 21 Hz. EKF methods have the advantage of being resistant to the failure of individual sensors. Sensor readings which differ from their expected value by more than a defined margin are rejected as sensor error and are not permitted to contribute to the estimation of aircraft state (ArduPilot Dev Team, 2020).

For the purposes of this analysis, the estimated state of the aircraft recorded in parameter XKF1 is used for plotting the flight path.

### **5.1.1 Pre-flight Checks**

As part of the larger planning process for flight testing, checklists were created to guide the procedure to ensure that (1) the aircraft is ready for flight and (2) the required parameters and data are recorded for analysis later on. The first checklist is termed the “maintenance log” and is completed by the flight controller before power is applied to the aircraft and after the aircraft has been recovered. The second checklist is termed the “flight log” and is largely completed after power has been applied to the aircraft by the base station attendant.

The maintenance log ensures that the aircraft is mechanically fit for flight. The aircraft is first inspected for damage and any deficiencies noted and corrected. The aircraft is then weighed with

Table 5.2: Summary of flight computer parameters collected for further analysis.

Parameter	Data Rate	Purpose
ACC	2000 Hz	Accelerometer outputs, raw accelerations along XYZ axes
AETR	25 Hz	Normalised control surface outputs, pre-mixing
ARSP	10 Hz	Airspeed data
ATT	21 Hz	Attitude, internally calculated from gyro data
BAT	10 Hz	Battery data including measured voltage and current draw
CTUN	25 Hz	Controller tuning parameters (e.g. desired and achieved roll, pitch, yaw)
GPS	5 Hz	GPS status, location, and speed data
GYR0/GYR1	2000 Hz	Gyroscope outputs, rotations about XYZ axes
IMU	50 Hz	Inertial Measurement Unit, combines data from multiple sensors to determine position & orientation
RCIN	25 Hz	Inputs from RC controller (pilot) to flight controller
RCOU	25 Hz	Outputs from flight controller to servos
XKF1	21 Hz	Estimated position & orientation from extended Kalman filter

all components installed and the centre of gravity measured. Ballast weights are added to the nose cone as required to place the centre of gravity in the appropriate location. CG measurements are taken using a special fixture which rests the tail of the aircraft (at the wing trailing edge) on a fulcrum and places the forward fuselage of the aircraft on a scale. Since the mass of the aircraft and the distance between fulcrum and scale are known, calculation of the CG location trivial. A chart, indicating the scale reading for optimal and aftmost allowable CG locations for a range of aircraft weights, is used for quick reference to remove calculation error in the field and keep time between flights to a minimum.

The serial number of each component used is recorded prior to each flight. Each individual manufactured piece (nose cone, fuselage, avionics panel, main panel, and vertical stabilizers) is serialized. Battery numbers, sides (left or right), and voltages are also recorded. Each checklist records flight date, flight number, and the name of the individual completing the check to maintain accountability.

The flight log is completed separately by the base station attendant. This person is in control of the flight control software via high-frequency (HF) radio link to the aircraft along with the weather station and the plans/goals for each flight. The base station attendant records the Ardupilot software

version, weather conditions including pressure and wind readings, the flight mode in use, and the condition of the GPS signal. As a double check due to the importance of the location of the CG, the base station attendant also records the centre of gravity as measured. A one-line summary of the flight goal is recorded in the flight log along with any notes/feedback called out by the pilot or other observations. Immediately prior to launch the bungee tensions and launch rail pull distances are called out and recorded.

To assist with correlating flight data with particular maneuvers in post-analysis, the precise time that the flight controller is powered on is recorded. Other events such as the arming of the propulsion system, ground checks of flight control movements, and any changes to flight mode are also recorded. After flight the general result of the test is recorded in each log, in particular the observed flight path and a description of any damage incurred.

### **5.1.2 Weather Conditions for Flight**

The current work resulted in two days of attempted flights, one with each version. MUFASA A.1 V1 was first tested on March 26th, 2022. After the design refinements and rebuild, MUFASA A.1 V2 was tested on October 5th, 2022. The main criteria for selecting an acceptable flight day was wind conditions. Selecting a day with low winds provides the best chance of achieving successful flight.

A review of relevant published works did not reveal a concrete rule for determining allowable crosswind conditions for flight operations, particularly for small-scale aircraft. Despite the maturity of commercial aviation technology, criteria for defining crosswind component limits and mitigation techniques for large aircraft are still being studied and revised to improve safety (Krüs, 2016). With full-scale aircraft, the limiting factor in a crosswind takeoff or landing situation is known to be pilot skill rather than airframe limitations (Cessna, 1972; Cashman, 2014). Regardless of pilot skill, both American FAA and European EASA regulations require that commercial airliners have a demonstrated safe crosswind component of 20 knots at 90-degrees for both takeoff and landing (FAA, 2022; EASA, 2021). Knowing that small-scale aircraft such as MUFASA A.1

are more sensitive to wind conditions than their full-scale counterparts (Etele, 2006; Mohamed et al., 2014), a stricter crosswind limit was imposed for the present work. Absent published data to inform specific limits, the decision was made to rely primarily on the experience of the test pilot. Their significant experience flying similarly configured hobbyist R/C jets was the best source available to determine acceptable flying conditions. Discussions with the pilot and other project members resulted in a limit of approximately 15 km/h (4.2 m/s) and a target of less than 10 km/h (2.8 m/s) (B. White, personal communication, February 2022).

Temperature limitations were primarily considered based on the comfort of individuals assisting with flight testing days and the requirement for fine motor skills and manual dexterity. Some pre-flight and repair operations cannot be performed with gloves on, thus days forecast with below-freezing temperatures were not considered for flight testing. The performance of electronics in cold weather was also considered in planning test days. Manufacturer recommendations for management of batteries at low temperatures were followed and the batteries were pre-warmed to room temperature before flight. The inertial measurement units in the flight controller are factory-calibrated at a particular temperature and have heaters to maintain accuracy. The IMU heater was able to maintain optimal temperature during each flight attempt; the reported IMU temperature never deviated from the target of 45°C by more than 0.1°C. Other parameters, such as airspeed data, are calculated by the flight controller taking ambient temperature into account and need not be so tightly controlled.

## **5.2 MUFASA A.1 V1**

The first flight testing day for V1 was the first day of acceptable weather conditions following completion of the airframe build. The as-flown condition of the airframe is shown in Fig. 5.1. Wind forecasts were within the chosen acceptable range for flight. Temperature conditions were colder than ideal but deemed acceptable to minimize delays in project timeline. Potentially negative effects on the batteries were limited by ensuring that they were kept at room temperature and

installed in the plane as late as possible, after all other pre-flight checks were completed. As part of the pre-flight checks, ballast was added to the forward-most point of the nose cone to locate the centre of gravity within acceptable limits for pitch stability. Details on the conditions for flights 1 & 2 can be found in Table 5.3. Descriptions of the flight attempts are given below with analysis to follow. Wind directions are shown as the direction from which the wind is incident; a  $0^\circ$  wind would be blowing directly from the north. For example, a headwind launch into a west ( $90^\circ$ ) wind requires a launch rail heading of  $90^\circ$ .

Table 5.3: Summary of Flight Conditions - MUFASA A.1 V1 Test Flights.

Flight Number	V1-F1	V1-F2
Flight Mode	Manual	Manual
Ardupilot Version	4.1.7	4.1.7
Launch Time	09:53	10:32
Air Temperature ( $^\circ\text{C}$ )	-1.9	0.5
Station Pressure (kPa)	92.69	92.63
Wind, Speed Heading Gust (m/s)	3.7 116 $^\circ$ 5.4	4.8 135 $^\circ$ 5.4
Launch Rail Heading	70.7 $^\circ$	74.8 $^\circ$
Launch Rail Inclination	10 $^\circ$	10 $^\circ$

### 5.2.1 V1 Flight Descriptions

At the moment of launch for flight V1F1, the pilot imparted a significant elevator-up command in an effort to gain altitude and thereby time to recover should the plane become unstable. The aircraft responded quickly to the pitch input but immediately lost airspeed. At the peak of climb, approximately 5 m above ground level, the nose attitude leveled off before continuing into an unrecoverable dive. The aircraft rolled while diving and struck the ground nose first. Despite this violent landing, damage was limited to a fracture of the nose cone (see Fig. 5.2). There was minor ingestion of dirt and grass by the intake requiring cleaning of the EDF blades. The nose cone was replaced and the remainder of the plane inspected and cleaned prior to the next flight.

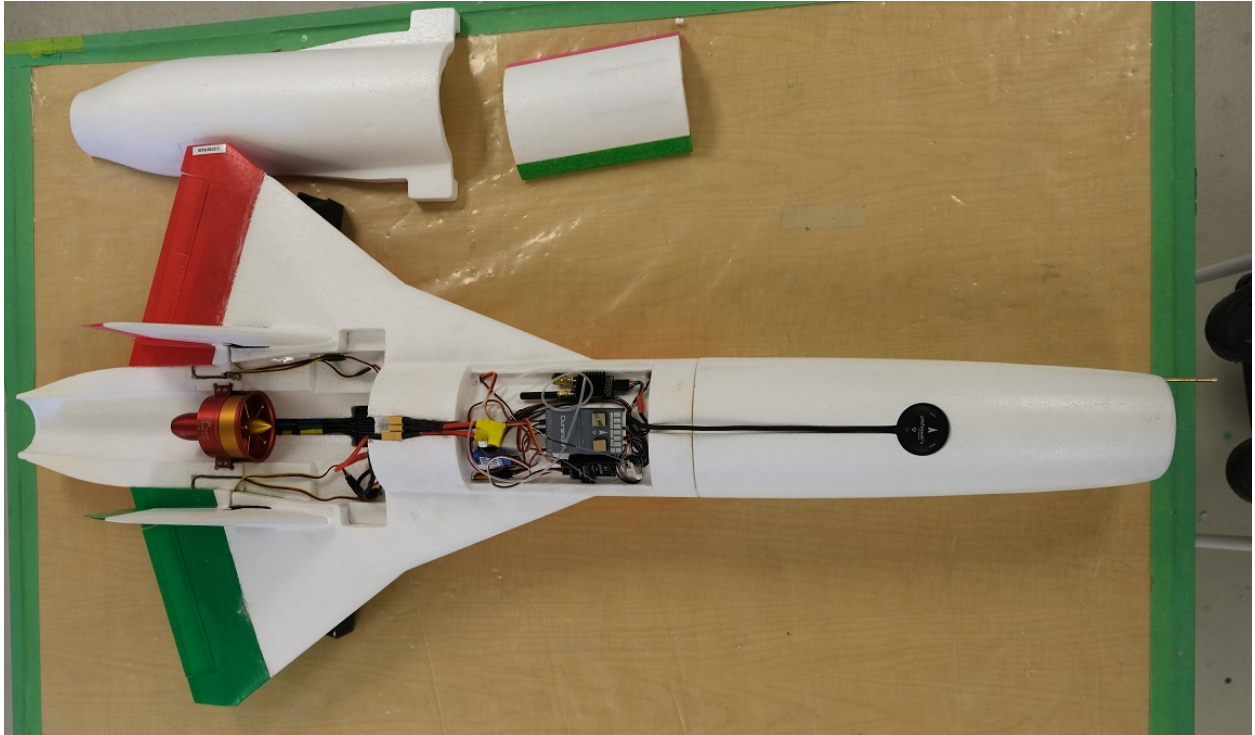


Figure 5.1: Photo of V1 airframe before flight testing. Main and avionics access panels removed to show internal components.

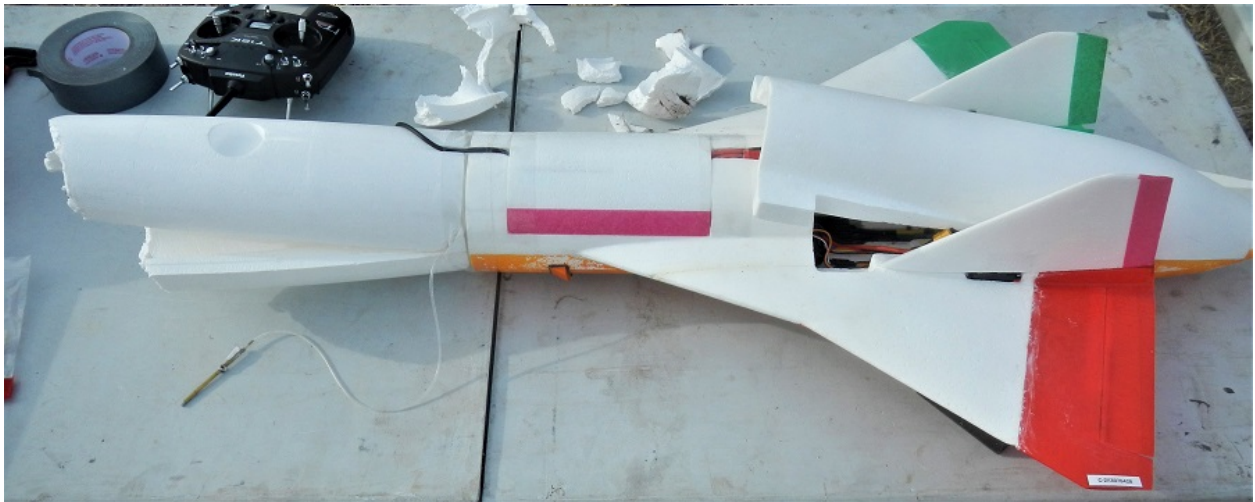


Figure 5.2: Photo of V1 airframe condition after flight 1. Note the split along the nose cone bond line with no damage to the remainder of the airframe.

For the next flight it was decided to that the pilot would maintain a more level flight attitude



off the launch rail. This would allow the aircraft to gain additional speed before attempting to gain significant altitude, reducing the possibility of losing airspeed and stalling the aircraft as in flight V1F1. Flight V1F2 was launched approximately 40 minutes after flight V1F1. The configuration of the aircraft for flight V1F2 was the same as that of the previous flight with the exception of the replaced nose cone (both nose cones were identical). At the moment of launch the aircraft remained nose-level but started to roll almost immediately to the left. After entering a steep bank to the left, the aircraft began to lose airspeed and stall. It rolled inverted before striking the ground, snapping off the starboard wing trailing edge cap and both vertical stabilizers. The green trailing edge cap is visible on top of the EDF in Fig. 5.3. The servo mount for the starboard vertical was torn out of the wing assembly. Damage to the aircraft was deemed beyond feasible repair and the testing day ended.

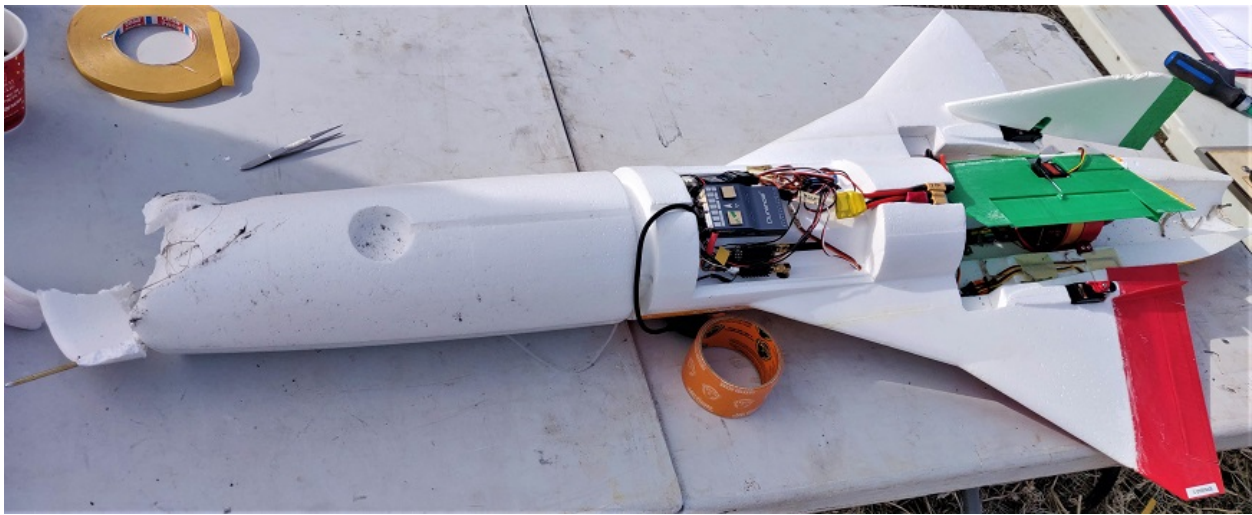


Figure 5.3: Photo of V1 airframe condition after flight 2.

### 5.2.2 V1 Flight Data

The lack of a successful, sustained flight shifts the analysis focus from general flight characteristics to a breakdown of the takeoff sequence to determine the cause of the mishap. Despite a total of less than 5 seconds in the air, the data collected during initial flight attempts provides valuable insight

into the characteristics of the aircraft. Careful review of the flight data alongside video recordings is first used to verify that the data collected aligns with the physical behaviour of the aircraft.

Flight V1F1 data are plotted in Fig. 5.4. The same plots are shown for all flights for direct comparison. Figure 5.6 shows the aircraft trajectory as a series of video frames superimposed on a base image. flight times are shown to aid in correlating the aircraft position to the data plot. The aircraft attitude and speed are plotted in the upper graph while control commands and roll rate are plotted in the lower graph. The moment of release is easily established from both the roll rate and measured pitch parameters. A pull sideways on the launch rail is required to release the cradle for launch. This sideways pull imparts some minor oscillations in roll ( $t=0.35-0.8$  s). At the same moment, the initial jerk of acceleration from the bungee imparts an additional 6 degrees of nose up attitude while still on the cradle. The initial spikes in roll rate settle out during launch and the pitch attitude returns to match the launch rail angle immediately after the aircraft clears the cradle at  $t=0.8$  s. At this point the aircraft reaches its maximum speed of 18.4 m/s for the flight. As is visible from the speed plot, the aircraft steadily slows down immediately after leaving the launch rail. Two factors contribute to create this result: the immediate and steep pitch-up after launch and the significant delay in the onset of maximum throttle. A delay of 0.72 seconds occurs between the first throttle command to the onset of maximum power. By the time maximum thrust is reached at  $t=1.3$  s the aircraft has slowed to 15.3 m/s. The delayed throttle response is due to the starting delay of brushless DC motors such as the one used in the EDF (Matsui, 1996). This starting delay can be minimized by setting the EDF to a non-zero rotational speed before launch.

Flight V1F2 data are plotted in Fig. 5.5 the the aircraft trajectory images shown in Fig. 5.7. V1F2 shows a more moderate initial trajectory with no major elevator input to cause an initial climb. The same throttle delay exists as was present in the first flight - the issue was not identified and addressed until video footage and flight data were reviewed in the days following testing. After launching ( $t=0.69$  s) at 19.0 m/s and before the power reaches maximum the aircraft slows to 18.8 m/s as the pitch attitude levels off. Once full thrust is reached at  $t=1.11$  s the aircraft appears to accelerate slightly with the nose  $1-2^\circ$  above horizontal; this indicates that there is enough thrust

to accelerate in a gentle climb. As the aircraft pitches up further ( $\geq 3^\circ$  at  $t=1.29$ s) the EDF is unable to produce enough thrust to maintain speed. The data also show a significant roll to the left immediately after leaving the launch rail ( $t=0.69$  s). This roll was uncommanded and likely a result of the wind incident from right of the nose at  $135^\circ$ . The uncommanded roll is discussed in detail in Section 5.4.

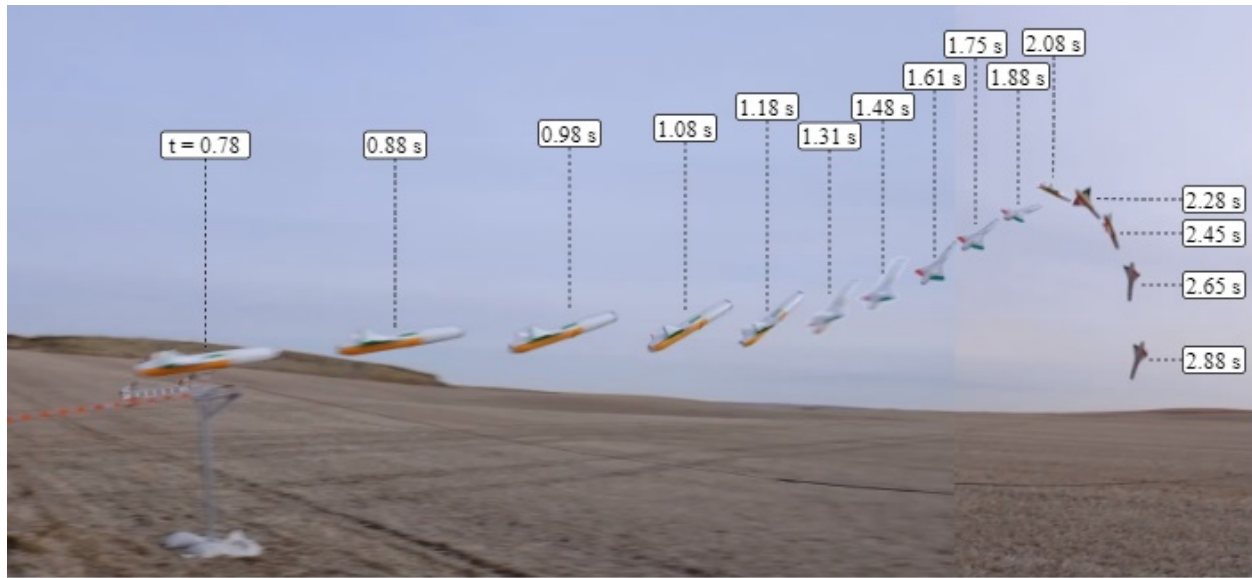


Figure 5.6: Aircraft trajectory during flight V1F1.

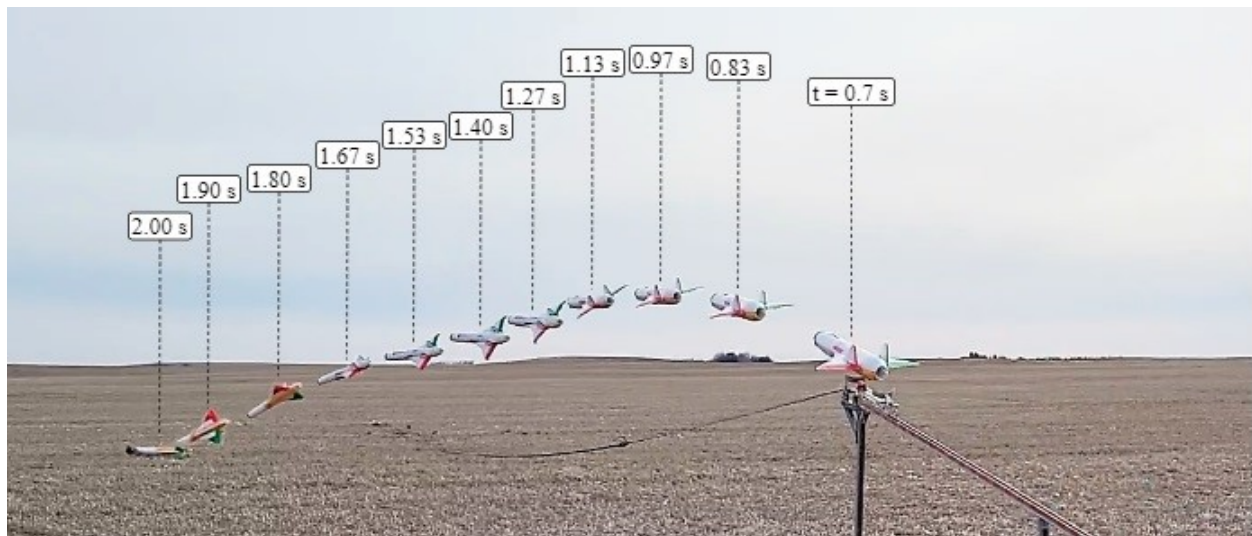


Figure 5.7: Aircraft trajectory during flight V1F2.

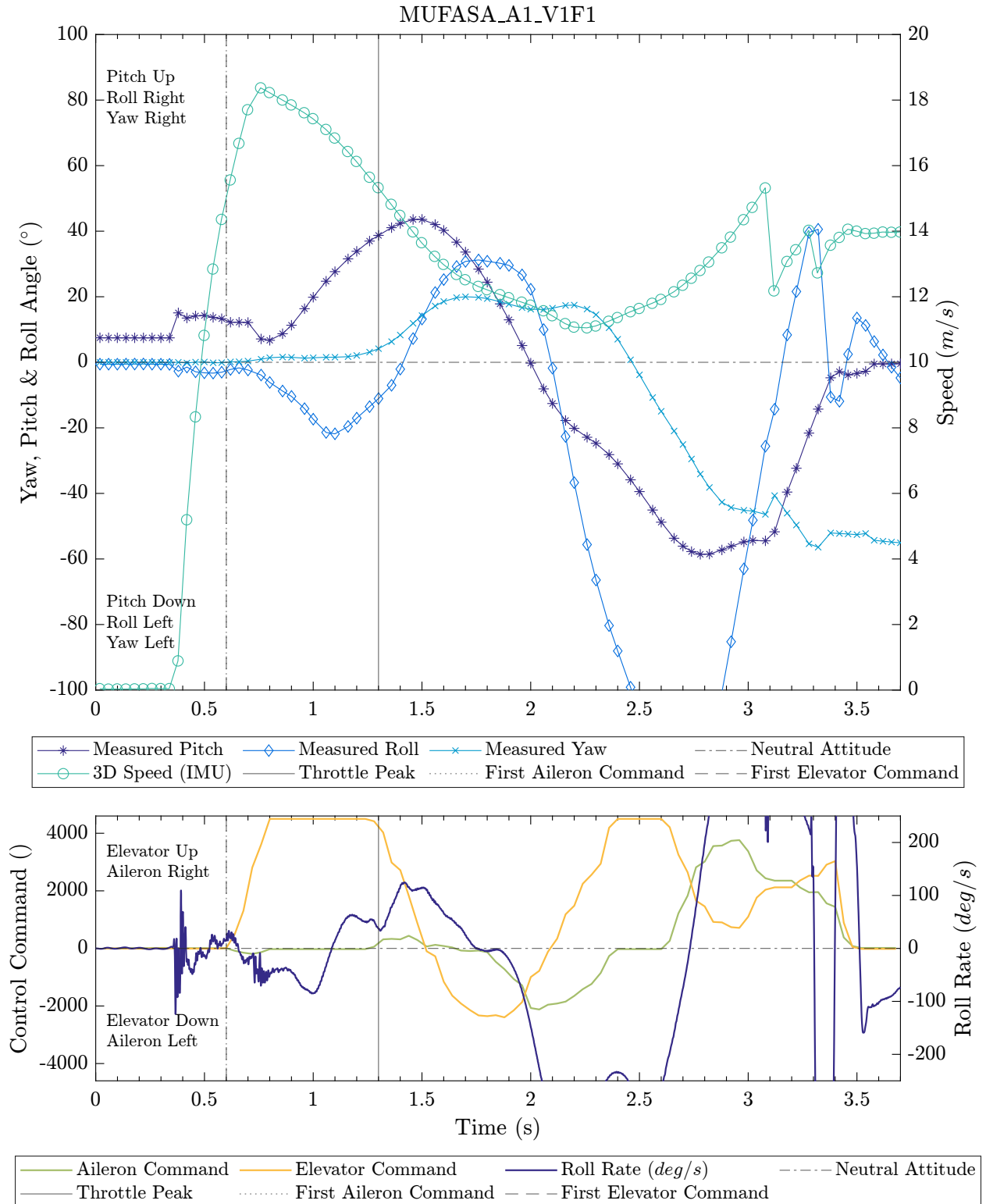


Figure 5.4: Analysis of various parameters on takeoff, flight V1-F1. Roll Rate scale deliberately omits extreme peaks in favour of showing early, moderate values before loss of control.

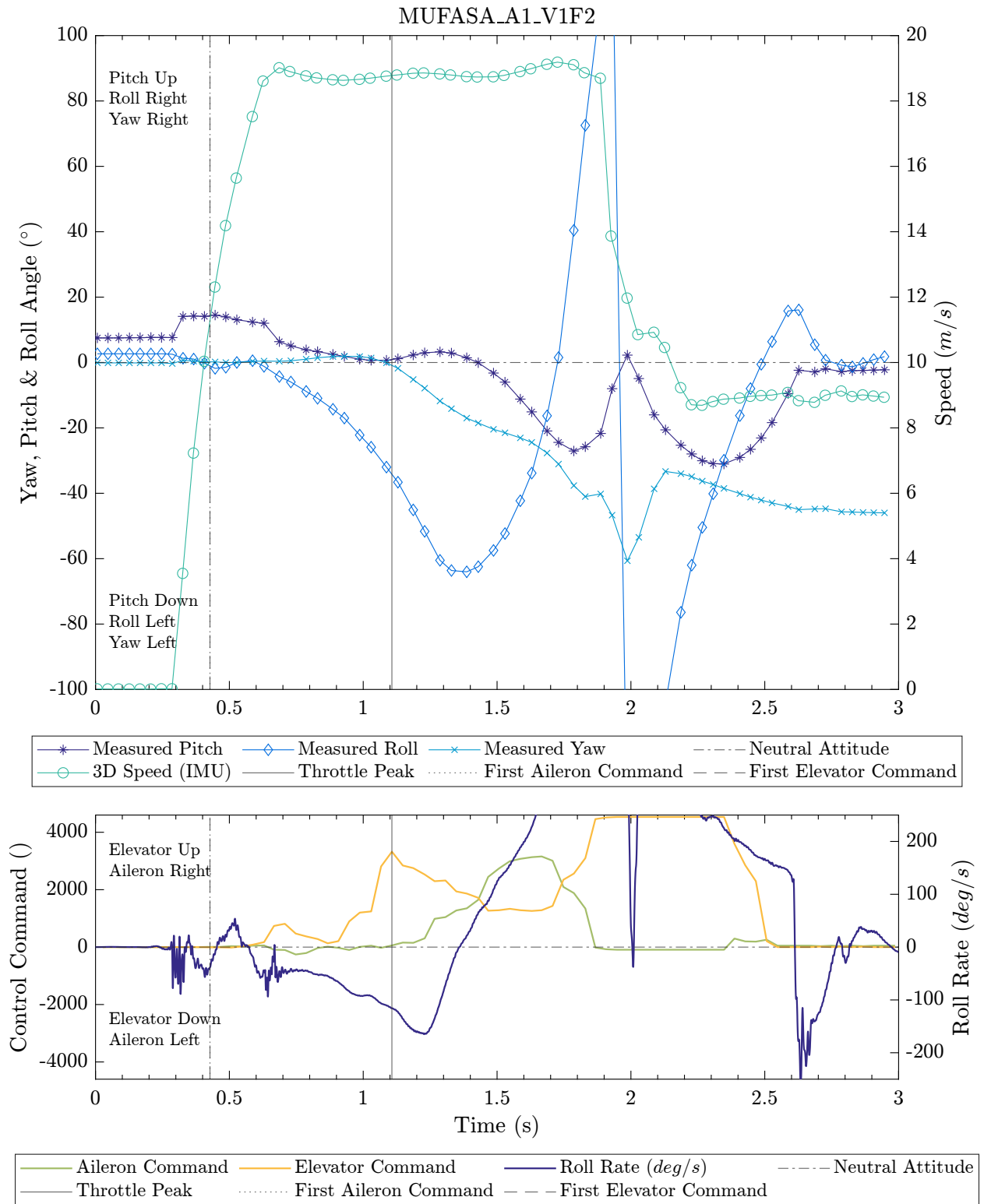


Figure 5.5: Analysis of various parameters on takeoff, flight V1-F2. Roll rate scale deliberately omits extreme peaks in favour of showing early, moderate values before loss of control.

## 5.3 MUFASA A.1 V2

Flight attempts for MUFASA A.1 V2 occurred on October 5th, 2022 following the completed rebuild of the aircraft incorporating design refinements discussed in Section 3.4. Moderate temperatures and very low morning winds made for a good opportunity for flight attempts. The week prior, on September 29th, a trip was made to the flight testing site and the launch rail was set up. The team made it so far as to arm the throttle for the aircraft but eventually canceled the test as winds picked up and it began to rain. Delays had been incurred earlier as the wind direction shifted dramatically by more than 120° and the launch rail had to be re-oriented. Table 5.4 provides a summary of the conditions for each V2 flight attempt.

The previous issue encountered with the long delay in thrust onset after advancing the throttle was addressed with a refined launch procedure. As the countdown begins, the pilot advances the throttle to approximately 50%, then rapidly to 100% at the moment of release. At 50% throttle there is sufficient friction to retain the aircraft's position on the cradle. The previously experienced throttle delay was effectively eliminated, with the aircraft reaching full power at or before the end of the launch rail in each test.

The Durandal flight controller as installed in the V2 airframe was misaligned by 3.5°. All yaw angles have been adjusted to show the correct headings. There was no measurable misalignment in V1.

Table 5.4: Summary of Flight Conditions - MUFASA A.1 V2 Test Flights.

<b>Flight Number</b>	<b>V2-F1</b>	<b>V2-F2</b>	<b>V2-F3</b>
Flight Mode	Manual	Manual	Stabilize
Ardupilot Version	4.1.7	4.1.7	4.1.7
Launch Time	08:44	11:20	12:18
Air Temperature (°C)	5.8	16.2	17.8
Station Pressure (kPa)	93.32	93.37	93.39
Wind, Speed Heading Gust (m/s)	0.3 83.6° 2.6	4.2 117.1° 6.8	4.8 120.0° 6.5
Launch Rail Heading	43.8°	100.2°	95.3°
Launch Rail Inclination	10°	6.5°	6.5°

### 5.3.1 V2 Flight Descriptions

Flight V2F1 began with a large nose-up command before reaching the end of the launch rail, causing a brief, rapid ascent and a significant loss of velocity. The loss of airspeed proved unrecoverable. The aircraft rolled aggressively to the right, then over-corrected to the left and became inverted. The aircraft had very little airspeed at this point and fell belly-first to the ground. Both wings broke away from the fuselage on impact. Figure 5.8 shows a photo of the airframe after field repairs; note the black seams of epoxy near the wing root. The remainder of the aircraft was largely intact and ready for further testing without substantial repair. Video footage of V2F1 with a telltale (hanging ribbon) in the background shows that there was effectively zero wind at the time of flight.



Figure 5.8: Photo of V2 airframe after repairs from first flight.

Flight V2F2 occurred after repairs were completed and the launch rail re-oriented to more closely match the wind direction. The launch rail inclination angle was reduced from  $10^\circ$  to  $6.5^\circ$  to provide the aircraft with a lower AoA on launch with the goal of gaining more speed after leaving the rail. For this flight the pilot was instructed to allow the aircraft to fly with as little control input as possible. Leaving the control surfaces undeflected and observing behaviour can be valuable in evaluating the inherent stability of the aircraft, and it was speculated that smaller control inputs



would minimize the likelihood of an over-correction and inversion similar to flight V2F1. The aircraft nose remained relatively level after leaving the launch rail. A slow, uncommanded roll to the left started immediately after clearing the cradle. This was accompanied by a yaw to the left. Despite roll inputs to level the wings, the aircraft continued to roll to the left. After reaching a roll angle of approximately  $45^\circ$  and a sideslip angle greater than  $10^\circ$  the aircraft was unrecoverable and struck the ground nose first before rolling over the right wingtip. Figure 5.9 shows the damage to the wingtip. The nose cone was also damaged and required replacement before further testing.



Figure 5.9: Photo of damage to V2 wing tip after flight 2.

Flight V2F3 required significant field repairs to the right wingtip in particular. Effectively all of the wing outboard of the elevon had been snapped off in the previous crash. The missing piece was recovered and re-attached using tape with wooden stir sticks for alignment and reinforcement. The right vertical stabilizer also required replacement. While the wing alignment was likely imperfect, it was decided that collecting imperfect data was preferable to ending the testing day at that point. The flight mode was also changed from MANUAL to STABILIZE. STABILIZE mode does not attempt to maintain a particular flight attitude, rather it attempts to limit the maximum attitude rate



of the aircraft. It is intended to prevent over-correction by the pilot where an excessively fast roll or pitch input might become unrecoverable. The flight path observed in flight 3 was remarkably similar to that of flight 2. The aircraft started a slow, uncommanded roll to the left immediately after leaving the launch rail. Despite control inputs commanding roll right, the uncommanded roll left continued, accompanied by a yaw to the left. Once the wings reached approximately  $40^\circ$  roll left the aircraft inverted and struck the ground. This crash snapped the right wing in half, including the right elevon and hinge line (see Fig. 5.10). This damage was deemed beyond feasible repair and the testing day ended.



Figure 5.10: Photo of damage to V2 wing tip after flight 2.

### 5.3.2 V2 Flight Data

Flight data collected from V2 attempts is plotted in Fig. 5.14 and is limited to the launch sequence and one to two seconds of motion before the aircraft strikes the ground in each case. Images displaying the trajectory are shown in Fig. 5.11. Flight V2F1 is very similar in trajectory to flight

V1F1 with the short climb immediately off the launch rail ( $t=0.91-1.27$ s), loss of forward airspeed, and roll to inversion before the ground strike. The obvious difference is the much larger roll experienced in V2F1 at the peak of the climb near  $t=1.3$  s. The aircraft rolled past  $90^\circ$  to the right ( $t=1.77$  s), then reversed in response to aileron input from the pilot and rapidly over-corrected to a complete inversion in the opposite direction at  $t=2.52$  s. This roll response with the elevons deflected upwards indicates that some measure of roll authority exists. Section 5.4.2 discusses the importance of elevon deflection with respect to roll control.

Flights V2F2 and V2F3 show remarkably similar trajectories. Both are displayed in image series' in Fig. 5.12 and Fig. 5.13. The primary difference from a control standpoint is that V2F2 was fully manual, while V2F3 had STABILIZE mode enabled. Flight V2F2 data show positive acceleration with a steady nose up attitude ( $t=0.80-1.42$  s), plotted in Fig. 5.15. An uncommanded roll to the left is present beginning immediately after leaving the launch rail. The aircraft leaves the launch rail at 21.6 m/s ( $t=0.77$  s) with an  $11.7^\circ$  nose up attitude. 0.7 seconds after leaving the rail the pitch attitude stabilizes at  $5.3^\circ$  nose up with a speed of 23.0 m/s. Past this point the uncommanded roll to the left accelerates and surpasses  $26^\circ$  left wing down (LWD). Control commands to counter the roll are ineffective and the aircraft inverts ( $t=1.8$  s) and strikes the ground.

Flight V2F3 in STABILIZE mode shows a similar trajectory, plotted in Fig. 5.16. The aircraft leaves the launch rail at 21.9 m/s with a  $10.1^\circ$  nose up attitude ( $t=0.74$  s). It accelerates to a maximum of 23.3 m/s at  $t=1.25$  s as the nose steadily drops to  $3^\circ$  above horizontal. The same uncommanded roll left is present as in other flights. The roll rate plot shows that the aircraft responds to the autopilot attempt to maintain the wings level; roll rate approaches zero at around  $30^\circ$  LWD ( $t=1.1-1.2$  s). As yaw angle exceeds approximately  $15^\circ$  nose left (exacerbating the crosswind component) the roll accelerates again and the aircraft inverts ( $t=1.76$  s) before striking the ground.

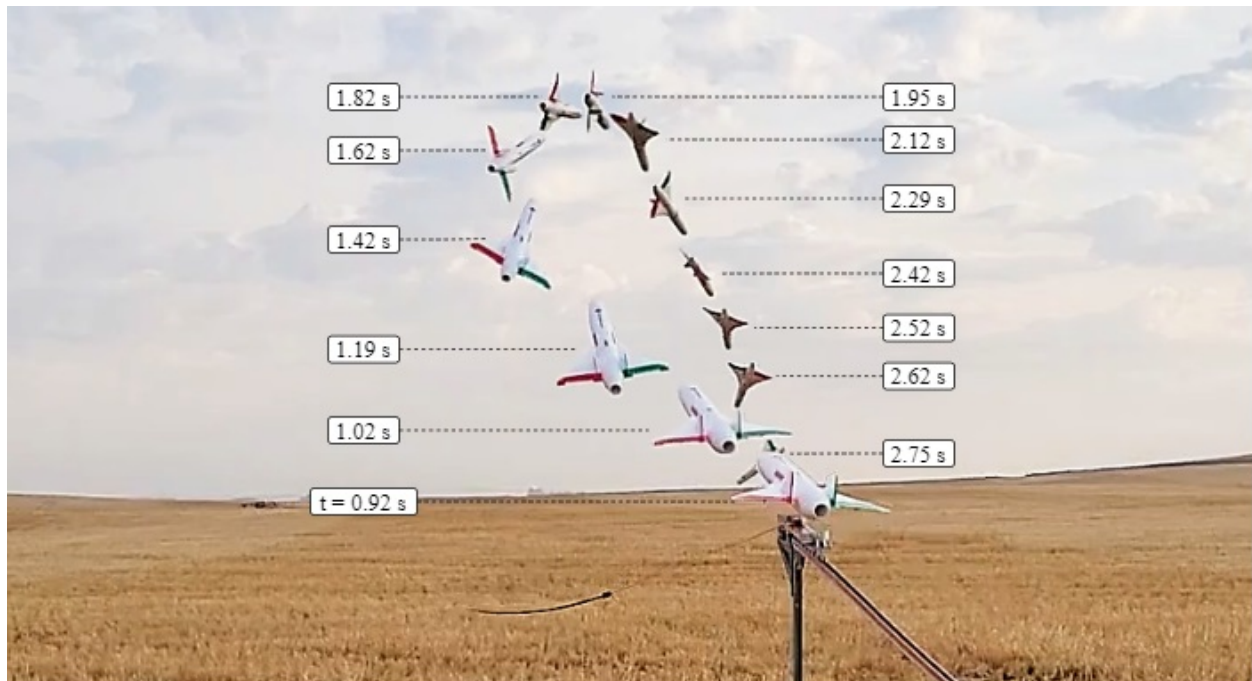


Figure 5.11: Aircraft trajectory during flight V2F1.

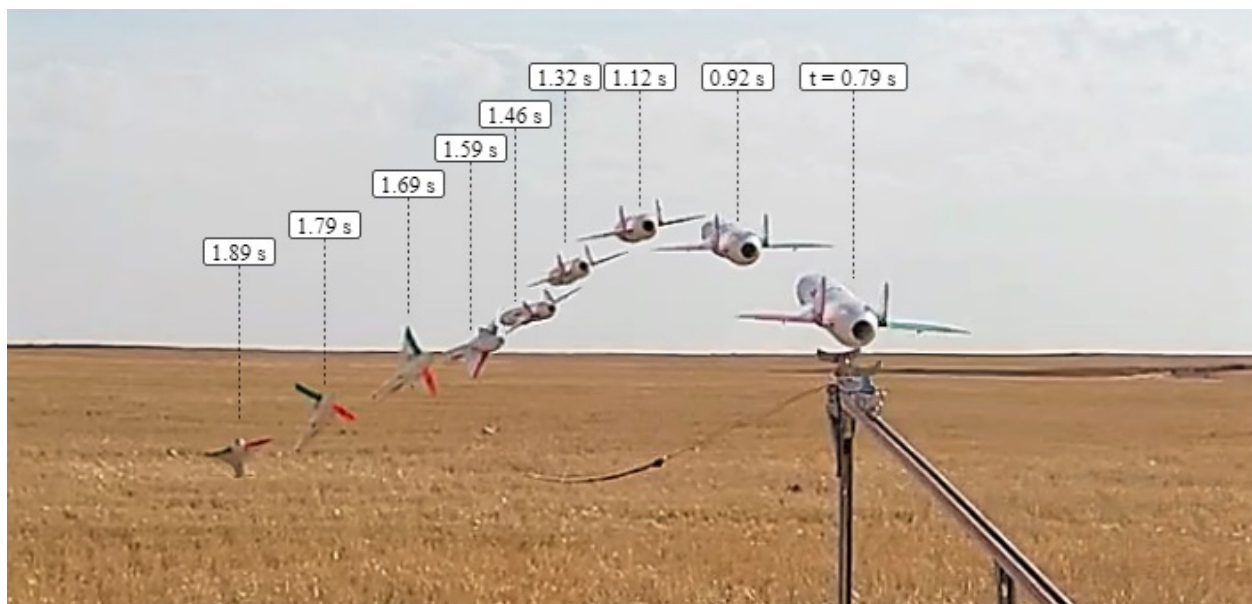


Figure 5.12: Aircraft trajectory during flight V2F2.

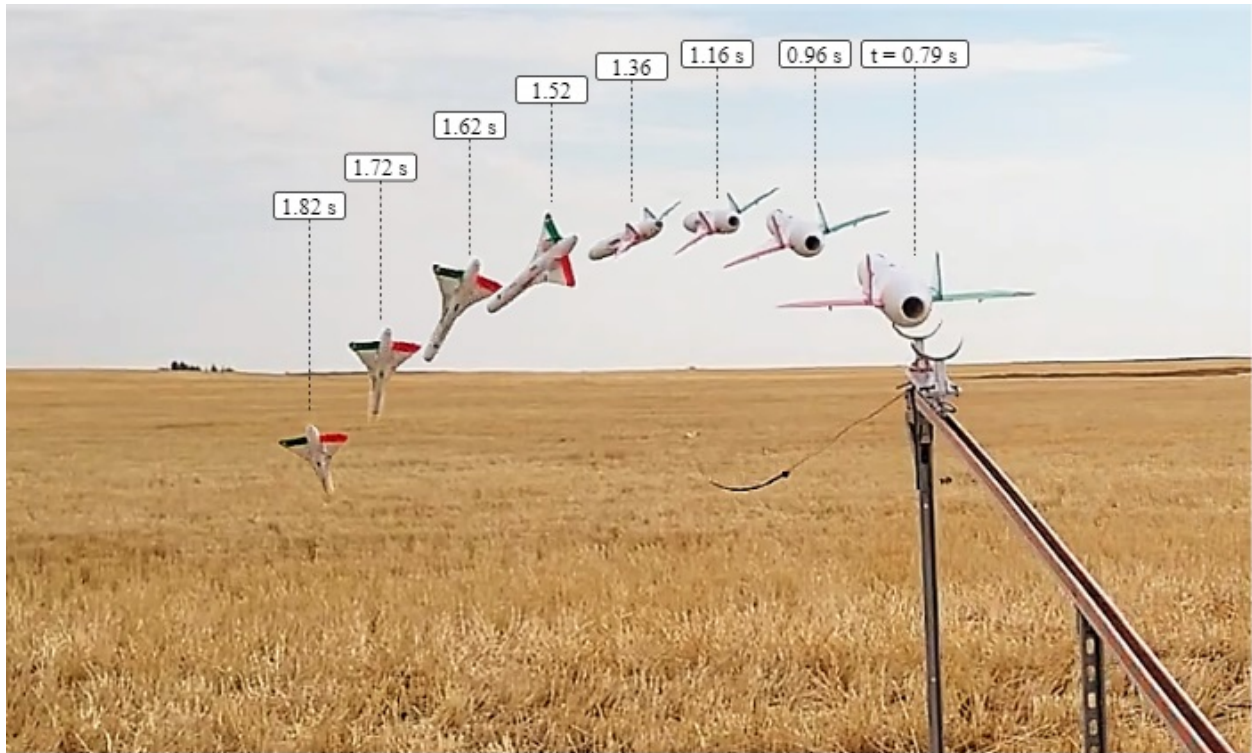


Figure 5.13: Aircraft trajectory during flight V2F3.

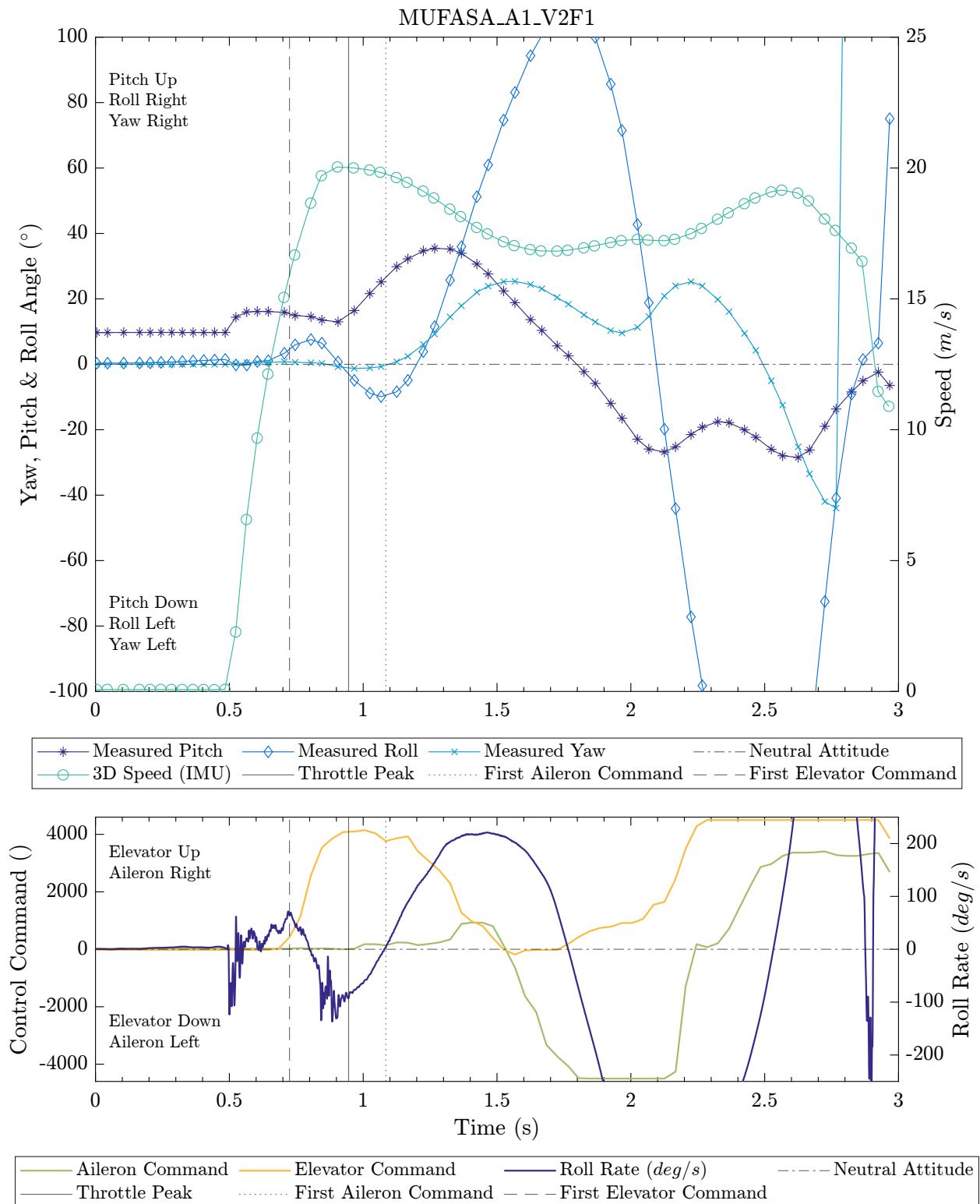


Figure 5.14: Analysis of various parameters on takeoff, flight V2-F1. Note the elevator-up command (nose-up) with the aircraft still on the launch rail.

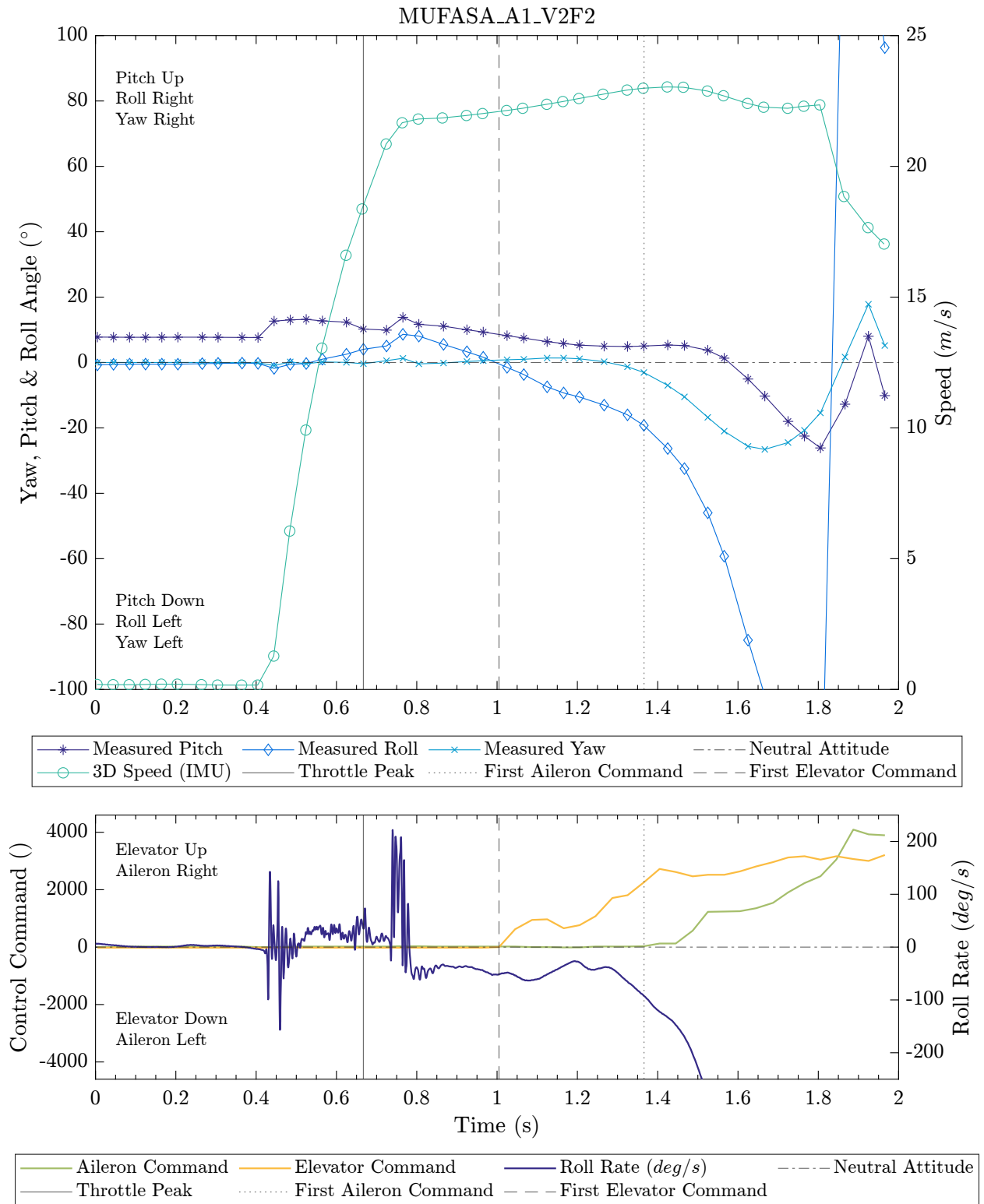


Figure 5.15: Analysis of various parameters on takeoff, flight V2-F2.



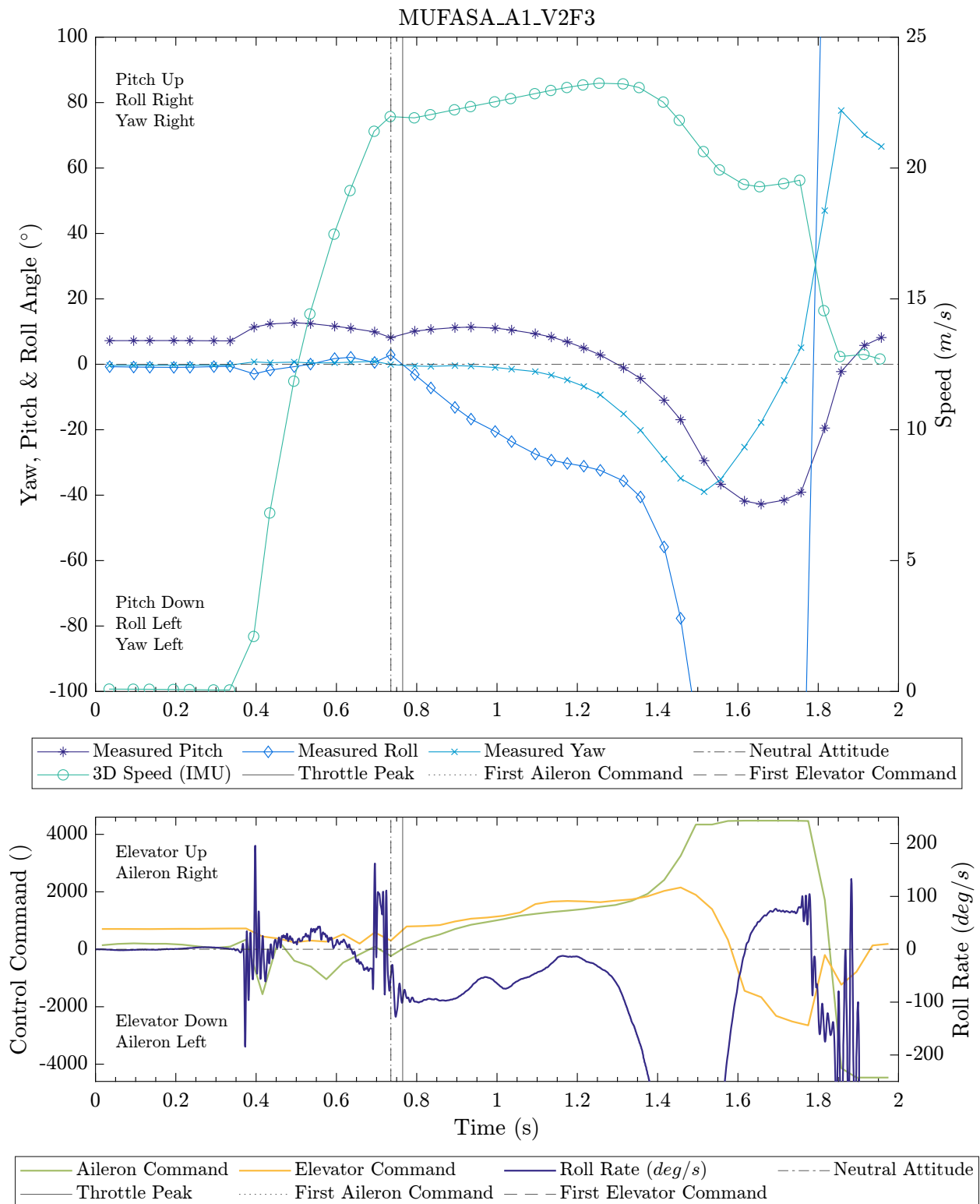


Figure 5.16: Analysis of various parameters on takeoff, flight V2-F3. Note that the vertical lines indicating the first elevator and aileron inputs are overlapping at the moment the aircraft leaves the launch rail.

## 5.4 Discussion

While testing of the aircraft did not result in a successful flight, valuable lessons were learned which will inform the ongoing efforts of the MUFASA project. The substantial data collected while the aircraft was in motion (during launch, powered forward flight, and uncontrolled descent) are enough to provide valuable insight into why the aircraft was uncontrollable and what can be done in the future to achieve stable flight.

The majority of the discussion presented here is focused on flights V1F2, V2F2 and V2F3 as each has a similarly level trajectory. These flights all share a common trait in the uncommanded roll left after leaving the launch rail. Despite short flight duration, the data collected in level flight with two versions of the aircraft are invaluable for comparison. First, an analysis of the takeoff speed and ability of each aircraft to accelerate is discussed. The takeoff attitude (orientation) of each is then analyzed to explore the cause and effect of the uncommanded roll left. Finally, the effectiveness of the vertical stabilizers and resulting lateral stability characteristics are explored.

### 5.4.1 Takeoff Speed

The speed of the aircraft off the launch rail is critical in ensuring that sufficient lift is produced to sustain flight. Simulations of each version of the aircraft were performed by Durante (2023) to determine the minimum control speed for each configuration. Minimum control speed is defined as the minimum speed at which the aircraft can maintain steady flight. Thrust level and control surface deflections determine the minimum forward velocity and corresponding AoA. The vertical component of thrust contributes to lift; because the EDF used for MUFASA A.1 provides less power than anticipated, thrust is the limiting factor. Simulations with increased thrust showed that a lower minimum speed was possible with a higher AoA. The minimum control speeds for V1 and V2 were determined to be 22 m/s and 19 m/s respectively, each at approximately  $10^\circ$  AoA using the listed takeoff weights for each version.

The reduction in minimum control speed from V1 to V2 is due to the reduced takeoff weight



and the increased wing area. While the changes made between versions did not result in a successful flight, the reduced weight did improve acceleration after launch and allowed the aircraft to reach a maximum speed of 23.1 m/s in flights V2F2 and V2F3, compared with 19.2 m/s in flight V1F2. These speeds are taken from the output of the extended Kalman filter (EKF) in the flight controller and correspond to ground speed. Airspeed in flight is not known as the airspeed probe was uncalibrated; calibration requires steady flight in circles to average out wind speeds and correlate airspeed with ground speed from GPS and EKF data.

Flight tests using V1 both left the launch rail below their minimum control speed and had insufficient excess thrust to accelerate before control was lost. Incident wind at approximately 5 m/s  $60^\circ$  from the nose brings the calculated airspeed to 21.7 m/s. Anderson (1999) suggests that liftoff speed be 10% faster than the stall speed. The V1 flights were effectively at the minimum control speed, however liftoff typically occurs at a higher speed to provide some margin for pilot error and measurement uncertainty. It is possible that V1 might have achieved sustained flight with sufficient thrust or a higher launch speed. V1 was calculated to be more laterally stable (see Section 5.4.3 and Durante (2023)) than V2 and showed less adverse yaw due to crosswind. V1 was also more able to counter crosswinds with the movable vertical stabilizers in place of the fixed fins on V2. Whether the control surfaces could have provided sufficient authority to overcome wind conditions and other flight uncertainties is difficult to determine and not in the scope of the present work.

Launch speeds for V2 flights were all above the reported minimum control speed of 19 m/s. During flight V2F2 with a 4.2 m/s headwind at  $17^\circ$  off the nose the maximum airspeed is calculated to be approximately 27 m/s, above the speed required for liftoff according to Anderson (1999). With this information it can be concluded that takeoff speed was not the limiting factor in the V2 flight attempts. The following analysis of takeoff attitude, primarily yaw due to crosswind and sideslip, provides insight into why the V2 flights were unsuccessful.

### 5.4.2 Takeoff Attitude

Analysis of the flight attempt data shows a consistent pattern of the aircraft aggressively rolling and yawing away from any crosswind component on takeoff. Flight V2F1 data are plotted in Fig. 5.14. A comparison between flights V2F2 and V2F3 is particularly revealing, plotted in Figs. 5.15 and 5.16 respectively. The trajectory of the aircraft and plots of the corresponding data are remarkably similar despite the difference in flight plan; V2F2 used MANUAL mode with the controls left untouched until the pilot needed to intervene, while V2F3 had STABILIZE mode active from the beginning of launch. In STABILIZE mode the flight computer attempts to maintain the wings and nose at level attitude. It has no control over throttle in this mode; throttle was maintained at maximum for all flights. Despite attempts to correct the adverse roll experienced, the aircraft continued to roll out of control in both cases.

From flight V1F1, it is clear that the aircraft has substantial pitch authority. During this flight the pilot commanded a significant nose-up attitude before the aircraft left the rail; at the moment of takeoff the elevator command was maximum deflection nose-up with 4.2% aileron command LWD. The aircraft responded to the aileron command with a roll to  $21.8^\circ$  LWD at 0.2 seconds after takeoff. The aggressive pitch-up command resulted in a rapid nose-up rotation from the  $10^\circ$  launch angle to a maximum of  $43.6^\circ$  approximately 0.75 seconds after takeoff. At this point the speed of the aircraft was 13.6 m/s, below the minimum control speed of 20 m/s. At the peak of the climb the roll rate exceeded  $220^\circ/\text{s}$  to the left. With little forward airspeed and minimal altitude, the pilot was unable to recover control. The response to roll inputs shortly after takeoff indicates that, when elevator-up command is present, the elevons have measurable roll authority.

Flight V2F1 also indicates that the aircraft has some level of roll authority with elevator-up deflection. On takeoff, when both elevons are deflected upwards, a small difference in deflection angle results in a roll response in the correct direction. Recall from Section 3.1.4 the large proportion of trailing edge occupied by the elevons; a disturbance of airflow due to elevon deflection will affect airflow over the entire wing. The elevons used for both roll and pitch control on this aircraft are analogous to a plain flap used as a high-lift device on other aircraft (Anderson, 1999). While

a flap has the benefit of increasing the maximum lift coefficient of a wing, it also decreases stall angle when deployed (see Fig. 5.17). The flap deflection downwards increases airfoil camber and increases the effective AoA. When a plain flap functioning as an elevon is deflected downward on a wing already near stall conditions it is likely that the flap will experience flow separation and vortex bursting (Maines et al., 2009). With a burst vortex, the effectiveness of the flap is near zero and the wing will stall and lose lift (Roskam and Lan, 1997). The loss of lift on the wing with the downward-deflected elevon causes a roll reversal and, in the case of MUFASA A.1, a roll out of control.

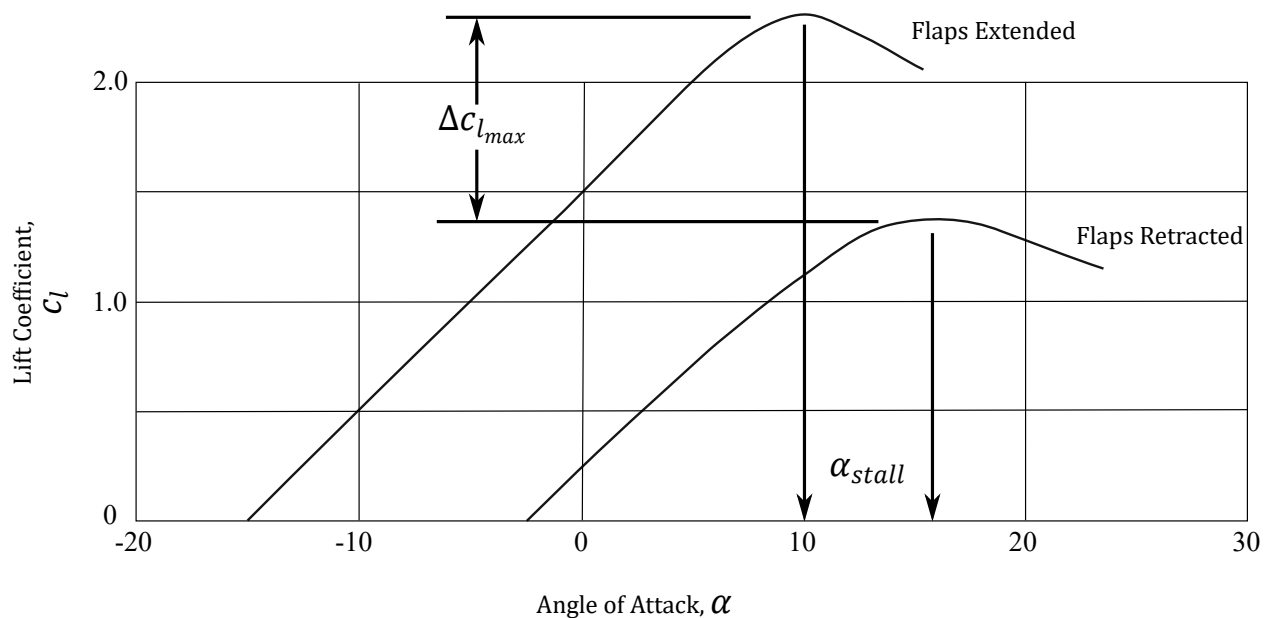


Figure 5.17: Lift curves of a NACA 6-series airfoil with sealed plain flap. Adapted from Roskam and Lan (1997).

The uncommanded roll to the left exacerbates the adverse yaw experienced by the aircraft, which in turn exacerbates the uncommanded roll. Circular plots in Figs. 5.18 to 5.20 describing flight V2F2 show the progression of aircraft yaw angle after takeoff. This sequence of yaw angles along with uncommanded roll indicate the severity of the yaw stability challenges with MUFASA A.1. A description of the sequence follows. The launch rail was oriented at a heading of approximately  $96^\circ$  ( $6^\circ$  south of east). As the aircraft leaves the launch rail the nose is pointing  $4.4^\circ$  to the



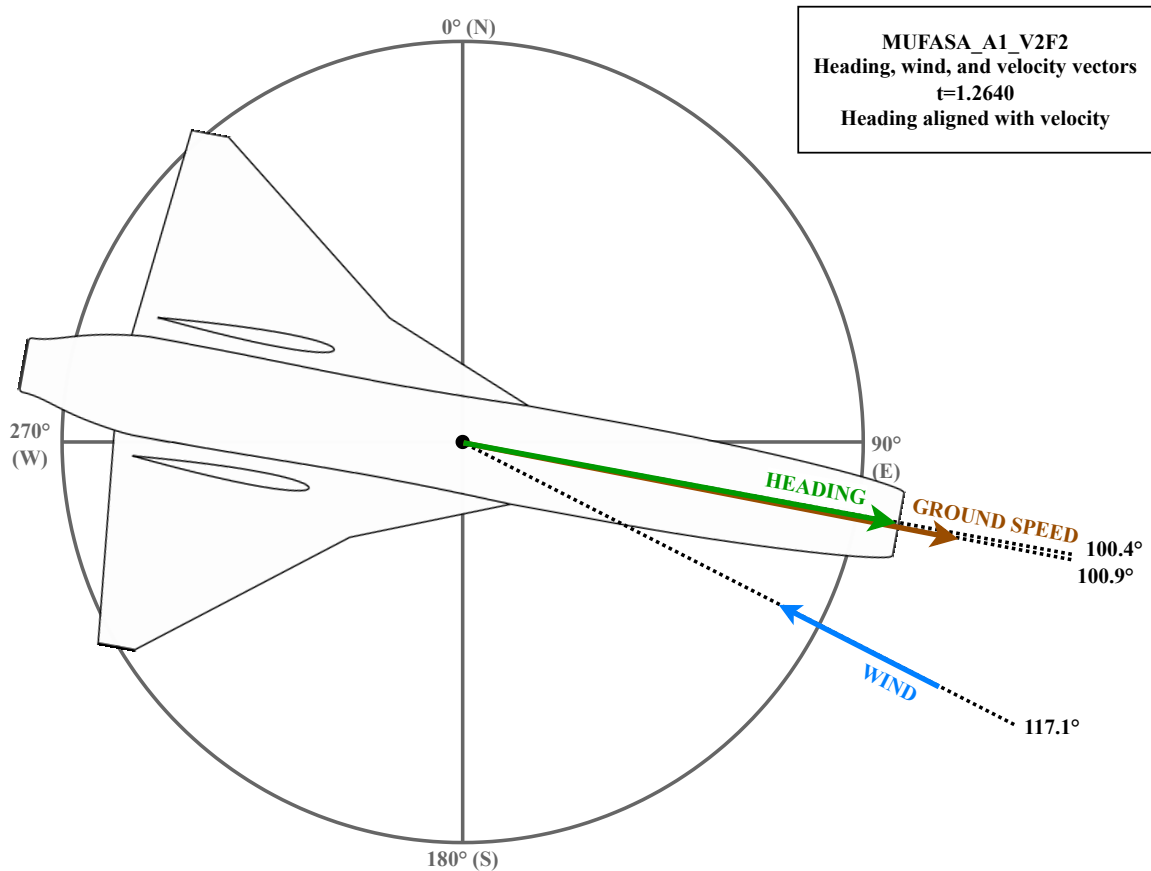


Figure 5.19: Velocity, heading, and wind direction vectors for V2F2 as the velocity direction and nose heading pass through alignment. Corresponding roll angle of  $-13.0^\circ$  (left wing down).

the aircraft is entering a spin (Weissman, 1973). Given sufficient altitude, recovery from a spin is normally possible (Nowak and Solies, 2000) and is indeed a training topic for pilots (Transport Canada, 2003). At less than five meters above ground there was no possibility of a spin recovery during the MUFASA flight attempts. A review of the video footage at this point shows the aircraft rolling until the wings are beyond perpendicular to the ground and the nose contacting the ground at 1.1 seconds after takeoff.

In contrast to V2-F1, flights V2-F2 and V2-F3 show effectively zero roll control authority. In each of these later flights there is a significant, uncommanded roll to the left which was unresponsive to roll inputs from the pilot. No elevator command was given, thus any roll-right command would place the left elevon below the centreline of the wing. At the same time, a crosswind coming

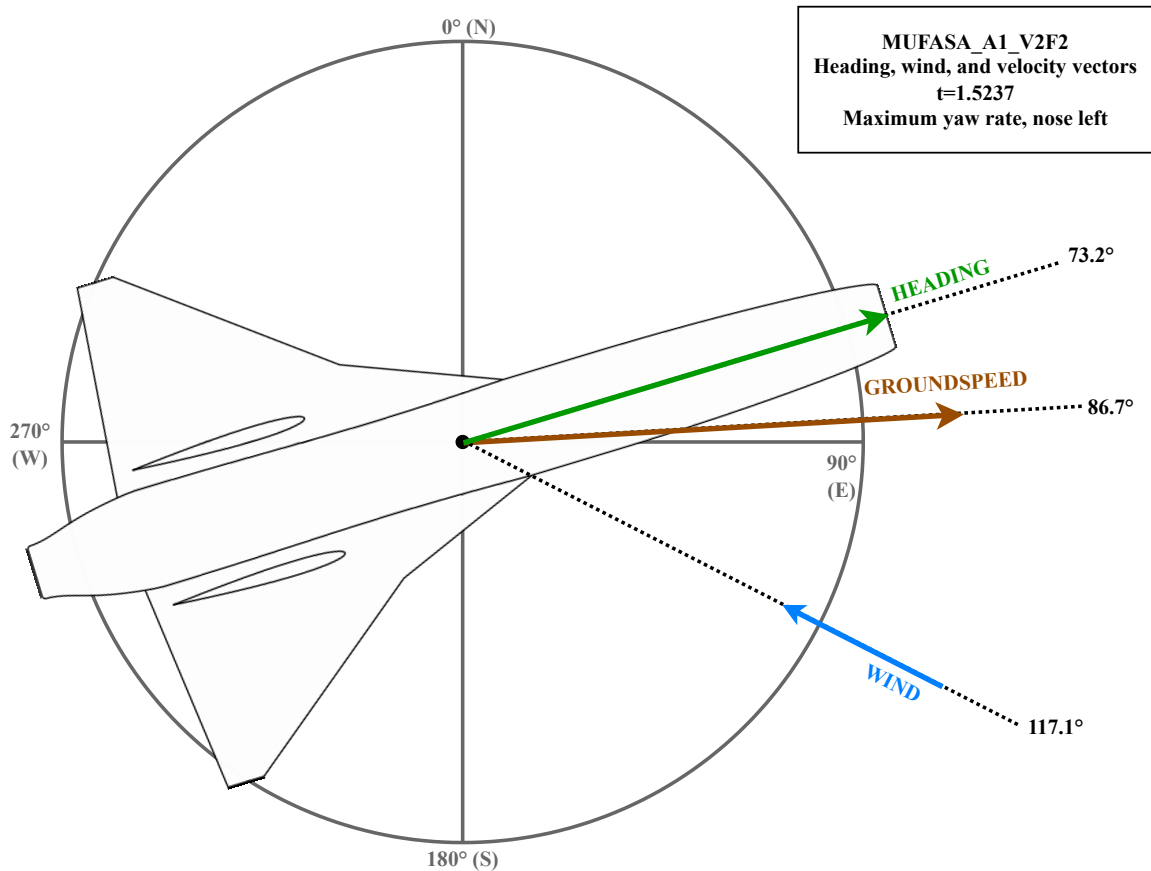


Figure 5.20: Velocity, heading, and wind direction vectors for V2F2 at moment of maximum yaw rate to the left. Corresponding roll angle of  $-46.0^\circ$  (left wing down).

from approximately  $20^\circ$  right of the nose provided additional airflow to the right wing and increasing lift on the right. Incident crosswind would have disrupted airflow over the left (downwind) wing, similar to a yawed cylinder (Pantelatos and Mathioulakis, 2004). Based on literature sources and comparing the fuselage diameter Reynolds number, the nose cone would not have experienced complete flow separation but would have significantly affected airflow over the downwind wing (Wetzel et al., 1998; Hoang et al., 1997). With strong airflow over the right wing and disrupted flow over the left, a lift imbalance existed creating a roll-left moment. At the same time, crosswind airflow over the vertical stabilizers incident from the right caused a rolling moment in the same direction due to their position above the centerline of the aircraft. Both the pilot and flight controller attempted to counter this roll with a roll-right aileron command. Deflecting the left elevon down

to counter the adverse roll was the only option available to an aircraft with no rudder control. This situation is precisely where US Navy pilots are instructed to use yaw inputs to correct roll as discussed in Section 2.2.1 (US Naval Air Command, 2004). By deflecting the left elevator downward the left wing experienced a further loss of lift and the roll became unrecoverable.

### **5.4.3 Lateral Stability & Vertical Tail Volume Coefficients**

The unsuccessful flight attempts described here led to the discovery that the MUFASA A.1 shape as-built was laterally unstable. The circular sideslip plots discussed in Section 5.4.2 show the nose of the aircraft yawing away from incident crosswind; the nose of a laterally stable aircraft would yaw into the wind. This indicates that the vertical tail surface area and moment arm were insufficient to counteract the adverse yaw due to crosswind and sideslip, contributing to a loss of control. Recall that vertical tail volume coefficient (VTVC), discussed in Section 3.1.3, is a predictor of lateral stability employed as a comparison to similar aircraft.

The VTVC calculated for MUFASA was within the suggested range (see Table 3.4) for a single-engined aircraft without extreme manoeuvrability requirements. By the measure of VTVC, MUFASA A.1 V1 has an appropriately sized tail and V2 has a tail slightly smaller than typical. Simulations performed by Durante (2023) initially indicated that both aircraft were laterally stable, albeit by a small margin in the case of V2. In the interest of preserving the high-speed design intent, the tail size was not increased for either aircraft. A comparison of conventional tail volume coefficients for various tailless delta-winged aircraft is shown in Fig. 5.21. A “tailless delta” aircraft has a vertical stabilizer but no horizontal tail separate from the wing itself.

Simulations were re-checked after flight test data indicated that both aircraft were laterally unstable. An error was found to have been made in the reference frame which reversed the sign of the relevant lateral stability coefficient. What the team thought was a stable aircraft was in reality unstable in yaw. While this was an unfortunate oversight, both simulation and flight data now contradict the VTVC prediction of a stable aircraft.

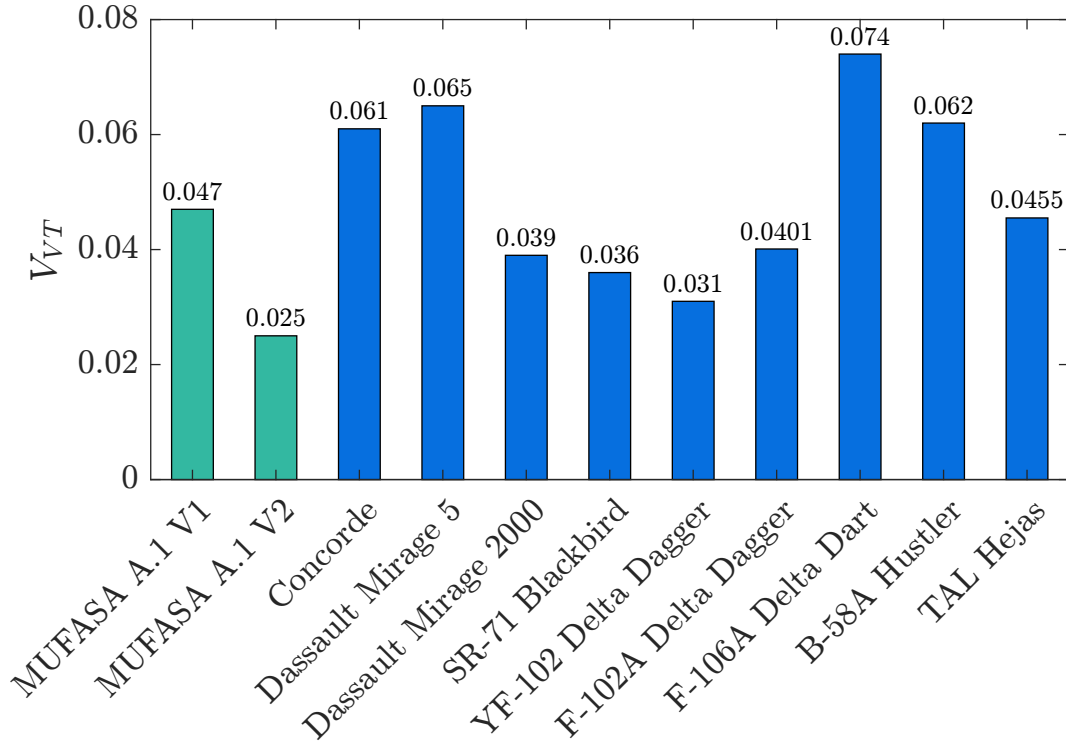


Figure 5.21: Calculated conventional tail volume coefficients based on (Eq. (3.7)).

### Fuselage-Normalized Vertical Tail Volume Coefficient

Accepting that the MUFASA aircraft were laterally unstable as-built indicates the possibility that conventional VTVC alone is insufficient as an early design tool for small-scale, high-speed configurations. Proposed here is a novel, fuselage-normalized VTVC intended to supplement the conventional VTVC. In place of the wingspan and wing area as in Eq. (3.7), the fuselage length and surface area are used to non-dimensionalize the tail size parameters (Eq. (5.1)). While V1 and V2 tails were within typical parameters based on conventional TVC, the tails are substantially undersized based on fuselage-normalized TVC. Figure 5.22 shows the result of calculations of  $V_{VT, fuse}$  for the same sample of tailless delta aircraft. A key consideration here is the relatively large fuselage area of MUFASA compared with larger aircraft of a similar configuration. If the wingspan of MUFASA were scaled up to match the Concorde jet (Rech and Leyman, 1997), its fuselage would be 1.7 times larger than that of the Concorde. This represents a substantial surface area ahead of the neutral point which is not accounted for by conventional VTVC. The fuselage-



normalized VTVC takes into account the larger fuselage area proportion of small-scale delta wings to improve early predictions of lateral stability.

$$V_{VT,fuse} = \frac{l_{VT}S_{VT}}{l_{fuse}S_{fuse}} \quad (5.1)$$

Similar to conventional VTVC in Eq. (3.7),  $l_{VT}$  and  $S_{VT}$  are the moment arm and surface area of the vertical tail while  $l_{fuse}$  and  $S_{fuse}$  are the fuselage length and surface area, respectively. Absent detailed data on actual fuselage areas, each aircraft was assumed to have a cylindrical fuselage for this simple calculation.

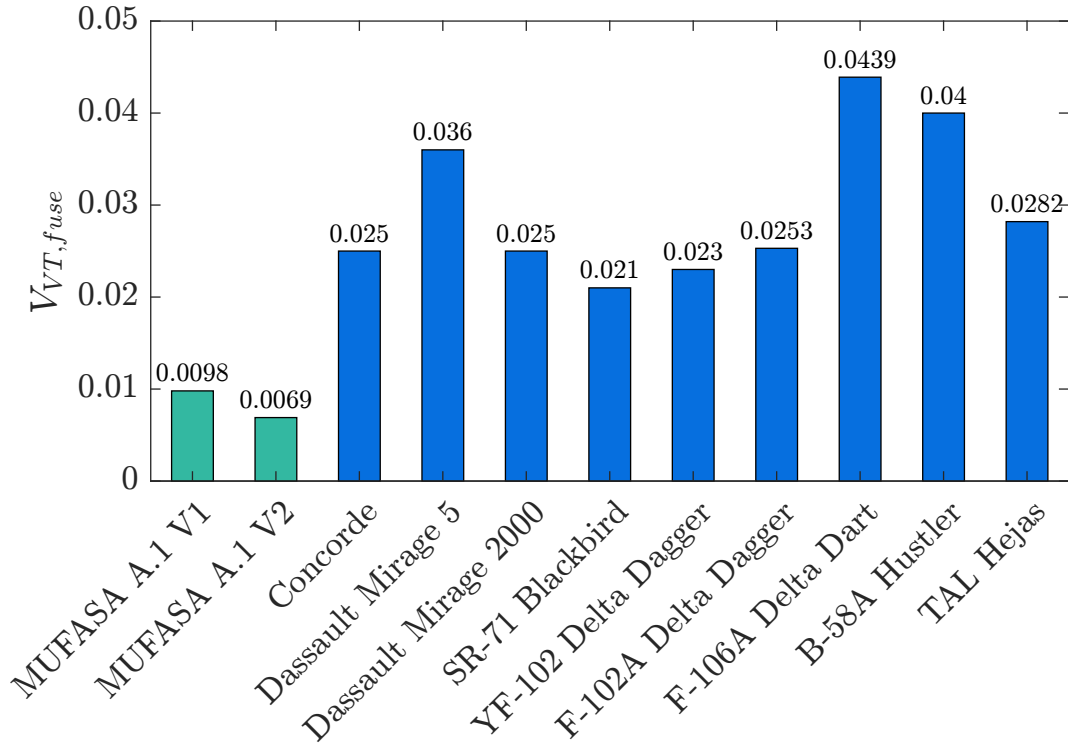


Figure 5.22: Calculated fuselage-normalized tail volume coefficients based on Eq. (5.1)).

While neither coefficient alone can fully predict lateral stability, fuselage-normalized TVC provides an additional early design parameter for comparison to existing aircraft. Had this parameter been used early in the design process for MUFASA A.1 the lack of stability might have been identified and corrected.

To begin establishing a baseline of acceptable values for fuselage-normalized TVC, its geometric mean with conventional TVC is calculated and shown in Fig. 5.24. Both versions of MUFASA A.1 fall below the 95% confidence interval for  $\sqrt{V_{VT}V_{VT,fuse}}$  based on the sample aircraft.

Two other aircraft in the sample fall below the 95% CI of the combined coefficients. Both the SR-71 Blackbird and the YF-102 Delta Dagger have values of 0.027, below the 95% CI of 0.0302. Both were subjected to extensive scrutiny before becoming production aircraft. The YF-102 underwent significant wind tunnel testing following early flight test issues with directional stability and roll coupling (Mendenhall, 1983). The vertical tail was enlarged and fuselage lengthened to improve lateral stability for the production F-102A model (Johnson and Boisseau, 1953; Boisseau, 1955). The F-102A produced with the enlarged vertical tail also included an aileron-rudder interconnect system to improve handling. The production version falls within the 95% CI of  $V_{VT,fuse}$ .

The SR-71 Blackbird has a value of  $\sqrt{V_{VT}V_{VT,fuse}}$  slightly below the 95% CI, similar to the YF-102. In early development the aircraft, then known as the YF-12, did not have a chine on the forebody of the fuselage. Rich (1974) explains in detail the positive effects that the chine had on lateral stability, in large part due to the reduction of flow separation and drag on the forebody which previously contributed to adverse yaw. An illustration of the effects of the chine on crossflow is shown in Fig. 5.23. In the lower diagrams in Fig. 5.23 the fuselage is illustrated with no chines. Rich explains that the addition of the chine elongates the fuselage cross-section and helps develop “strong vortex flow at the chine edges”, significantly improving the directional stability at nonzero AoA. Wind tunnel tests with and without the chine were repeated with and without vertical tails to ensure that the forebody effects were significant (Rich, 1974). The chine also served to move the neutral point forward, increasing the effective moment arm for the vertical tails to act on and further increasing lateral stability. A sophisticated stability augmentation system was also used on the SR-71 to assist the pilot in maintaining control (McMaster and Schenk, 1974). Each of these effects improves the stability of the SR-71 and is not accounted for in either vertical tail volume coefficient. Initial sizing coefficients are not intended to account for these effects, however this information explains how the SR-71 was able to maintain stable flight despite early indications of

marginal lateral stability.

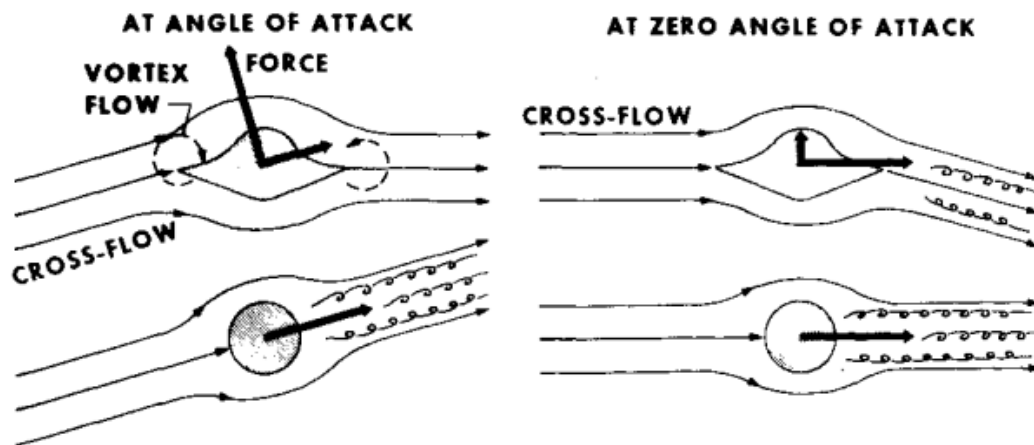


Figure 5.23: Illustration of chined forebody effects on crossflow for the SR-71, adapted from Rich (1974).

Some aircraft have significantly larger tail volume coefficients than the confidence interval would suggest is necessary. The Mirage 5, F-106A Delta Dart, and B-58A Hustler all fall above the upper 95% CI. This does not indicate an unstable aircraft. Rather, these aircraft have more inherent stability than others at the cost of a larger drag penalty. The more conservative tail sizing sacrifices top speed to improve directional stability characteristics.

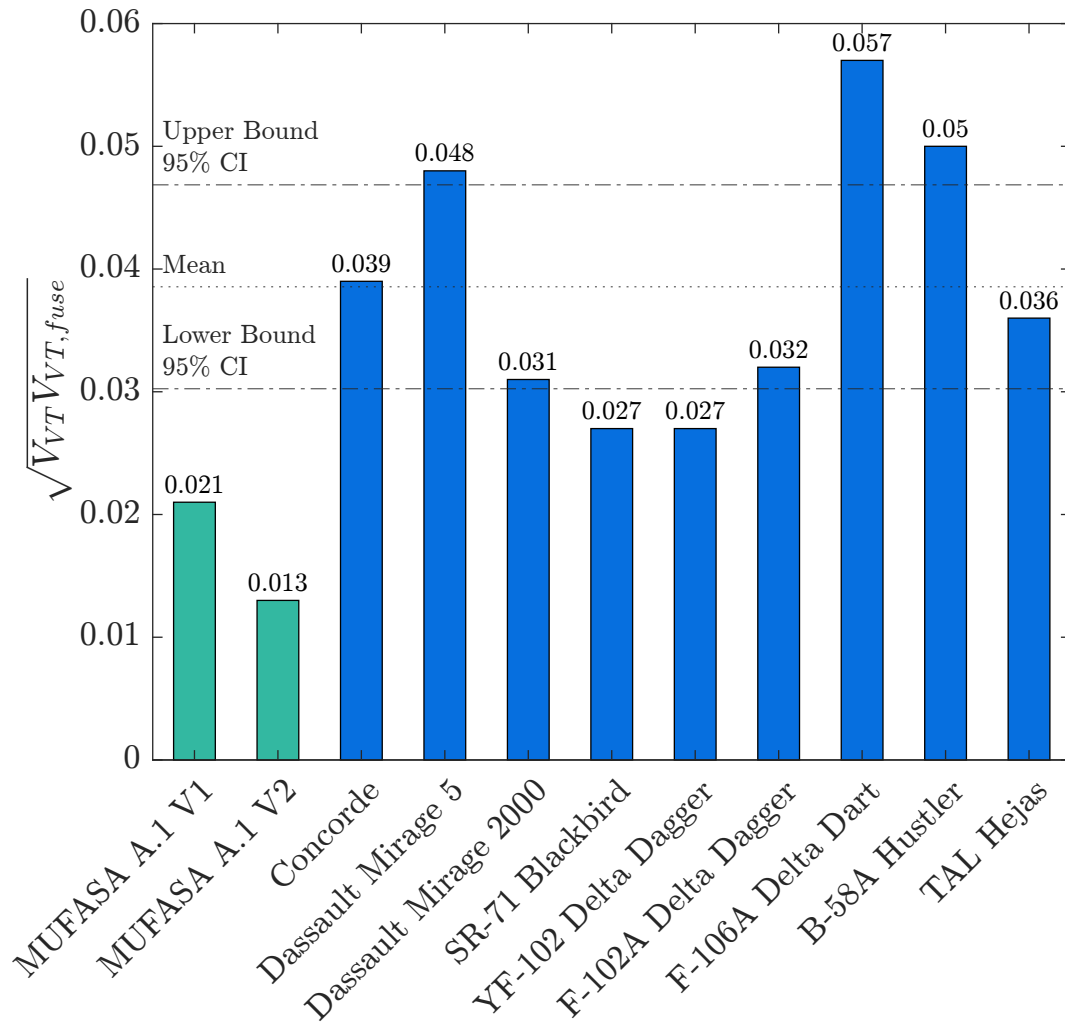


Figure 5.24: Geometric mean of conventional and fuselage-normalized tail volume coefficients for various tailless delta aircraft.

# Chapter 6

## Conclusions & Recommendations

A small-scale, high-speed uncrewed aerial vehicle (UAV) was designed, manufactured, and flight tested. Several established early-stage design guidelines intended for full-scale aircraft were assessed for applicability to the present configuration.

Analysis found that conventional tail sizing methods based on tail volume coefficient were insufficient in sizing the vertical tail for high-speed small-scale aircraft, contributing to lateral instability. While MUFASA A.1 had a proportionally-appropriate vertical tail for the wing span and area, the tail was vastly undersized relative to the fuselage area which is presented to any cross-wind or sideslip component. Comparison of MUFASA A.1 tail sizes showed a significant difference to full-scale aircraft of all configurations. It is recommended that future initial sizing work on small-scale high-speed (UAVs) include calculation of both established and fuselage-normalized tail volume coefficients as discussed in Section 5.4.

Empirical design methods for determining intake capture area on jet engines were unsuitable for an electric ducted fan using a pitot-style intake at the present scale. Losses due to capture area were much larger than initially expected and were partially alleviated when intake area was increased to match fan diameter. Further study is required to create methodologies for sizing EDF intakes and determine optimal design configurations incorporating NACA intakes, blow-in doors, or similar features.

## **6.1 Recommendations & Future Work**

Lessons learned in conducting the present research can provide helpful insight for future initiatives to further the field of small-scale, high-speed UAVs in general and the MUFASA project in particular. Experimental testing has provided the team with important guidance on the best ways to conduct further research and design activities.

### **6.1.1 Flight Testing Improvements**

The flight testing portion of the research was relatively smooth from an operations perspective thanks to careful planning and collaboration between individuals. Improvements can still be made to a number of aspects of testing days.

The launch rail was effective in consistently accelerating the plane and releasing it cleanly into the air. Unfortunately the design meant that it was time-consuming to re-orient the rail to adjust for changing wind conditions. For an aircraft so sensitive to crosswind components, launch orientation is critical. It would also be advantageous to use a launch rail capable of accelerating the aircraft to significantly faster than the minimum control speed. This allows more margin for error and significantly reduces the challenge of low speed control by allowing the launch cradle to stabilize the aircraft through the very low speed range. A rail which can be more readily moved to account for wind changes and launch at greater speeds would de-risk this portion of the flight sequence.

Given the flight testing record of MUFASA A.1, an aircraft with increased durability and/or improved modularity could significantly reduce the interval between flights and increase the number of crashes before a testing day is forced to end. An aircraft which can more readily survive a crash can be re-launched much more quickly than one requiring significant repairs. MUFASA A.1 was built for minimum weight and manufacturing complexity, however future versions may benefit from trading that simplicity for a somewhat heavier but significantly more durable airframe. Improving modularity by ensuring that fragile components such as wingtips, trailing edges, and verticals are easily replaceable will also help to accelerate the flight test process.

### **6.1.2 Aircraft Improvements**

Substantial improvements to the aerodynamic design are available for future implementation to improve performance and stability. The present work focused on the manufacture of an existing design with minimal refinements implemented between versions. Further design work incorporating additional stability study and aerodynamic performance predictions will increase the chances of success in future flights. Leveraging simulation data can be an important tool for fine-tuning of a design, however simulations should always be checked against known quantities and relations for validation.

The lateral stability of the aircraft could be significantly improved by reducing drag on the fuselage area presented to a crosswind. Implementing a chine-like feature on the forebody and blending the wings to the fuselage could provide a measurable improvement without significantly increasing drag from increased vertical tail area.

While thrust available to the aircraft in flight was able to show some acceleration, very little excess thrust was available which severely limited the ability of the aircraft to recover from an imperfect launch or compensate for adverse flight conditions. Increasing the available thrust at the expense of flight endurance appears an attractive option for achieving an initial successful flight.

The intake of the aircraft which incurred substantial thrust losses is an area with the potential for significant performance gains. Work to reduce these losses will improve the efficiency of the existing configuration and allow for either a decrease in mass budget allocated to the propulsion system or a notable increase in flight endurance. Any improvement in endurance time will substantially improve the rate of data collection for further study and thus the advancement of the project as a whole.

# References

- Abbott, I. H. and von Doenhoff, A. E. (1959). *Theory of Wing Sections\_ Including a Summary of Airfoil Data*. Dover Publications.
- Alonso, J. J. and Colonno, M. R. (2012). Multidisciplinary optimization with applications to sonic-boom minimization. *Annual Review of Fluid Mechanics*, 44(1):505–526. <https://www.annualreviews.org/doi/10.1146/annurev-fluid-120710-101133>.
- Altfeld, H.-H. (2016). *Commercial Aircraft Projects: Managing the Development of Highly Complex Products*. Routledge, first edition. <https://www.taylorfrancis.com/books/9781315572833>.
- Anderson, J. D. (1999). *Aircraft Performance and Design*. WCB/McGraw-Hill, Boston, second edition.
- Anderson, J. D. (2002). *The Airplane: A History of Its Technology*. American Institute of Aeronautics and Astronautics, Reston, VA.
- ArduPilot Dev Team (2020). ArduPilot documentation - EKF2 estimation system. ArduPilot. <https://github.com/ArduPilot/ardupilot/wiki/blob/09611d4ba8df4162a45e6b807e42bd3e1178c059/dev/source/docs/ekf2-estimation-system.rst>.
- ArduPilot Dev Team (2022). Complete Parameter List — Plane documentation. <https://ardupilot.org/plane/docs/parameters-Plane-stable-V4.1.7.html>.



- ArduPilot Dev Team (2023). ArduPilot Documentation — ArduPilot documentation. <https://ardupilot.org/ardupilot/index.html>.
- Barbosa, L. M. F., Maciel, F. M. O., and de Barros, J. E. M. (2014). Study of unmanned supersonic aircraft configuration. In *23rd SAE Brasil International Congress and Display*, pages 2014–36–0193. <https://www.sae.org/content/2014-36-0193/>.
- Barua, P., Sousa, T., and Scholz, D. (2013). Empennage statistics and sizing methods for dorsal fins.
- Bihrlé, W. and Meyer, R. C. (1976). F-14A high angle of attack characteristics. *Journal of Aircraft*, 13(8):576–583. <https://arc.aiaa.org/doi/10.2514/3.58690>.
- Blakey, S., Rye, L., and Wilson, C. W. (2011). Aviation gas turbine alternative fuels: A review. *Proceedings of the Combustion Institute*, 33(2):2863–2885. <https://linkinghub.elsevier.com/retrieve/pii/S1540748910003950>.
- Boisseau, P. C. (1955). Investigation in the langley free-flight tunnel of the low-speed stability and control characteristics of a 1/10-scale model simulating the convair f-102a airplane. <https://ntrs.nasa.gov/citations/20050029385>.
- Boom Supersonic (2022). Boom - XB-1. <https://boomsupersonic.com/>.
- Cai, G., Dias, J., and Seneviratne, L. (2014). A survey of small-scale unmanned aerial vehicles: Recent advances and future development trends. *Unmanned Systems*, 02(02):175–199. <https://www.worldscientific.com/doi/abs/10.1142/S2301385014300017>.
- Candel, S. (2004). Concorde and the future of supersonic transport. *Journal of Propulsion and Power*, 20(1):59–68. <https://arc.aiaa.org/doi/10.2514/1.9180>.
- Cantwell, B. (2013). Course notes AA200 - The NACA airfoil series. [https://web.stanford.edu/~cantwell/AA200\\_Course\\_Material/The%20NACA%20airfoil%20series.pdf](https://web.stanford.edu/~cantwell/AA200_Course_Material/The%20NACA%20airfoil%20series.pdf).

- Cashman, J. (2014). Crosswind guidelines. [http://leonardo-in-flight.nl/PDF/Boeing%20Crosswind\\_Guidelines.pdf](http://leonardo-in-flight.nl/PDF/Boeing%20Crosswind_Guidelines.pdf).
- Cessna (1972). Cessna 172L owner's manual. <https://www.manualslib.com/manual/1330192/Cessna-172-Skyhawk.html#manual>.
- Chawla, K. K. (2012). *Composite Materials*. Springer New York, New York, NY. <http://link.springer.com/10.1007/978-0-387-74365-3>.
- Chiba, K., Makino, Y., and Takatoya, T. (2008). Evolutionary-based multidisciplinary design exploration for silent supersonic technology demonstrator wing. *Journal of Aircraft*, 45(5):1481–1494. <https://arc.aiaa.org/doi/10.2514/1.33272>.
- Chiba, K., Makino, Y., and Takatoya, T. (2012). Design-informatics approach for intimate configuration of silent supersonic technology demonstrator. *Journal of Aircraft*, 49(5):1200–1211. <https://arc.aiaa.org/doi/10.2514/1.C031116>.
- Ciliberti, D., Della Vecchia, P., Nicolosi, F., and De Marco, A. (2017). Aircraft directional stability and vertical tail design: A review of semi-empirical methods. *Progress in Aerospace Sciences*, 95:140–172. <https://linkinghub.elsevier.com/retrieve/pii/S0376042117301598>.
- Cole, H. H. (1974). Design, integration, and testing of the F-15. In *Aerospace Engineering and Manufacturing Meeting*, page 20. <https://www.sae.org/content/740843/>.
- Colgren, R. and Loschke, R. (2008). Effective design of highly maneuverable tailless aircraft. *Journal of Aircraft*, 45(4):1441–1449. <https://arc.aiaa.org/doi/10.2514/1.32083>.
- Common Sense RC (2017). Basic lithium polymer (LiPo) battery instructions. [https://commonsenserc.com/product\\_instructions/lectronpro\\_instructions\\_v7\\_august\\_2017.pdf](https://commonsenserc.com/product_instructions/lectronpro_instructions_v7_august_2017.pdf).

- Cook, M. V. and de Castro, H. V. (2004). The longitudinal flying qualities of a blended-wing-body civil transport aircraft. *The Aeronautical Journal*, 108(1080):75–84. [https://www.cambridge.org/core/product/identifier/S0001924000005029/type/journal\\_article](https://www.cambridge.org/core/product/identifier/S0001924000005029/type/journal_article).
- Crosby, F. (2020). *The World Encyclopedia of Fighter Aircraft: An Illustrated History from the Early Planes of World War i to the Supersonic Jets of Today*. Lorenz Books.
- Dalman, B. (2021). Conceptual design methods for small-scale supersonic uncrewed aerial vehicles. Master’s thesis, Schulich School of Engineering. <https://prism.ucalgary.ca/handle/1880/113956>.
- Dalman, B., Korobenko, A., Ziade, P., Ramirez-Serrano, A., and Johansen, C. T. (2021). Validation and verification of a conceptual design tool for evaluating small-scale, supersonic, unmanned aerial vehicles. In *AIAA Aviation Forum 2021*, Virtual event. American Institute of Aeronautics and Astronautics. <https://arc.aiaa.org/doi/10.2514/6.2021-2415>.
- Drela, M. (1989). XFOIL: An analysis and design system for low reynolds number airfoils. In Brebbia, C. A., Orszag, S. A., Seinfeld, J. H., Spanos, P., Cakmak, A. S., Silvester, P., Desai, C. S., Pinder, G., McCrory, R., Yip, S., Leckie, F. A., Ponter, A. R. S., Holz, K.-P., Bathe, K.-J., Connor, J., Wunderlich, W., Argyris, J., and Mueller, T. J., editors, *Low Reynolds Number Aerodynamics*, volume 54, pages 1–12. Springer Berlin Heidelberg, Berlin, Heidelberg. [http://link.springer.com/10.1007/978-3-642-84010-4\\_1](http://link.springer.com/10.1007/978-3-642-84010-4_1).
- Dudek, P. (2013). FDM 3D printing technology in manufacturing composite elements. *Archives of Metallurgy and Materials*, 58(4):1415–1418. <http://journals.pan.pl/dlibra/publication/102133/edition/88150/content>.
- Durante, B. (2023). Flying and handling qualities of small-scale supersonic uncrewed aerial vehicles. Master’s thesis, University of Calgary, Calgary, Canada.

- Durante, B. J., Gair, S. R., Ramirez-Serrano, A., Morton, C., and Johansen, C. T. (2022). Development and controllability evaluation of a small-scale supersonic UAV. In *AIAA AVIATION 2022 Forum*, Chicago, IL & Virtual. American Institute of Aeronautics and Astronautics. <https://arc.aiaa.org/doi/10.2514/6.2022-3792>.
- Earnshaw, P. B. and Lawford, J. A. (1964). Low-speed wind-tunnel experiments on a series of sharp-edged delta wings. Technical Report R&M 3424, Ministry of Aviation. <https://reports.aerade.cranfield.ac.uk/bitstream/handle/1826.2/4008/arc-rm-3424.pdf?sequence=1&isAllowed=y>.
- EASA (2021). EASEA CS-25 Large Aeroplanes. <https://www.easa.europa.eu/en/document-library/certification-specifications/group/cs-25-large-aeroplanes>.
- Eckstrom, C. V. and Peele, E. L. (1974). Flight assessment of a large supersonic drone aircraft for research use. *NASA-TM-X-3259*.
- Etele, J. (2006). Overview of wind gust modelling with application to autonomous low-level UAV control.
- Etkin, B. and Reid, L. D. (1996). *Dynamics of Flight: Stability and Control*, volume 12. John Wiley & Sons, Inc., 3rd edition. <http://physicstoday.scitation.org/doi/10.1063/1.3060977>.
- FAA (2022). 14 CFR Part 25 – Airworthiness Standards: Transport Category Airplanes. <https://www.ecfr.gov/current/title-14/chapter-I/subchapter-C/part-25>.
- Franke, U. E. (2015). The global diffusion of unmanned aerial vehicles (UAVs), or ‘drones’. In Aaronson, M., Rauxloh, R., Aslam, W., Dyson, T., Barrinha, A., and Alison, L., editors, *Precision Strike Warfare and International Intervention: Strategic, Ethico-Legal, and Decisional Implications*, Routledge Global Security Studies, pages 52–72. Routledge, London.

- Gabaldo, M., Barros, J. E., Guerra, M. D., and Oliveira, E. (2016). Aerothermodynamic simulation model for new hypersonic propulsion: Rocket Ignited Supersonic Combustion Ram Jet. In *AIAA SPACE 2016*, Long Beach, California. American Institute of Aeronautics and Astronautics. <http://arc.aiaa.org/doi/10.2514/6.2016-5323>.
- Gabaldo, M., Barros, O. R., and Barros, J. E. M. (2017). Technical and economic feasibility analysis of a two stage reusable satellite launcher using RISC RAM jet engines. In *26th SAE BRASIL International Congress and Display*, pages 2017–36–0150. <https://www.sae.org/content/2017-36-0150/>.
- Gair, S., Baker, J., Cristini, P., Foret, A., Hinh, K., and Schulz, J. (2019). Interim design report - SSUAV capstone design project. Technical report, University of Calgary, Calgary.
- Gair, S., Baker, J., Cristini, P., Foret, A., Hinh, K., and Schulz, J. (2020). Final design report - SSUAV capstone design project. Technical report, University of Calgary, Calgary.
- Gera, J., Wilson, R., Enevoldson, E., and Nguyen, L. (1981). Flight test experience with high-alpha control system techniques on the F-14 airplane. In *1st Flight Test Conference*, Las Vegas, NV, U.S.A. American Institute of Aeronautics and Astronautics. <https://arc.aiaa.org/doi/10.2514/6.1981-2505>.
- Gerhart, P. M., Gerhart, A. L., and Hochstein, J. I. (2016). *Munson, Young and Okiishi's Fundamentals of Fluid Mechanics*. John Wiley & Sons Inc, Hoboken, eighth edition edition.
- Goldsmith, L. and Seddon, J. M. (1993). *Practical Intake Aerodynamic Design*. Blackwell scientific, London Edinburgh Boston [etc.].
- Goodman, A. (2014). Conceptual aerodynamic design of delta-type tailless unmanned aircraft. *International Journal of Unmanned Systems Engineering*, 2(2):1–15. <http://www.ijuseng.com/#/ijuseng-2-s2-1-15-2014/4583842647>.

- Gote, G., Kamble, P., Hodgir, R., Mittal, Y., and Karunakaran, K. P. (2022). Mathematical modeling of surface roughness in polystyrene foam machining. *The International Journal of Advanced Manufacturing Technology*, 120(11-12):7461–7475. <https://link.springer.com/10.1007/s00170-022-09229-6>.
- Greenwell, D. I. and Wood, N. J. (1994). Roll moment characteristics of asymmetric tangential leading-edge blowing on a delta wing. *Journal of Aircraft*, 31(1):161–168. <https://arc.aiaa.org/doi/10.2514/3.46469>.
- Greitzer, E. M. (1980). Review—axial compressor stall phenomena. *Journal of Fluids Engineering*, 102(2):134–151. <https://asmedigitalcollection.asme.org/fluidsengineering/article/102/2/134/409206/ReviewAxial-Compressor-Stall-Phenomena>.
- Gudmundsson, S. (2022a). The anatomy of the tail. In *General Aviation Aircraft Design*, pages 481–516. Elsevier. <https://linkinghub.elsevier.com/retrieve/pii/B9780128184653000112>.
- Gudmundsson, S. (2022b). The anatomy of the wing. In *General Aviation Aircraft Design*, pages 321–413. Elsevier. <https://linkinghub.elsevier.com/retrieve/pii/B9780128184653000094>.
- Gudmundsson, S. (2022c). Thrust modeling for propellers. In *General Aviation Aircraft Design*, pages 597–656. Elsevier. <https://linkinghub.elsevier.com/retrieve/pii/B978012818465300015X>.
- Guessasma, S., Belhabib, S., and Nouri, H. (2019). Printability and tensile performance of 3d printed polyethylene terephthalate glycol using fused deposition modelling. *Polymers*, 11(7):1220. <https://www.mdpi.com/2073-4360/11/7/1220>.
- Gursul, I. (1994). Unsteady flow phenomena over delta wings at high angle of attack. *AIAA Journal*, 32(2):225–231. <https://arc.aiaa.org/doi/10.2514/3.11976>.

- Gursul, I. (2004). Recent developments in delta wing aerodynamics. *The Aeronautical Journal*, 108(1087):437–452. [https://www.cambridge.org/core/product/identifier/S0001924000000269/type/journal\\_article](https://www.cambridge.org/core/product/identifier/S0001924000000269/type/journal_article).
- Hassanalian, M. and Abdelkefi, A. (2017). Classifications, applications, and design challenges of drones: A review. *Progress in Aerospace Sciences*, 91:99–131. <https://linkinghub.elsevier.com/retrieve/pii/S0376042116301348>.
- Henne, P. A. (2005). Case for small supersonic civil aircraft. *Journal of Aircraft*, 42(3):765–774. <https://arc.aiaa.org/doi/10.2514/1.5119>.
- Hoang, N., Rediniotis, O., and Telionis, D. (1997). Symmetric and asymmetric separation patterns over a hemisphere cylinder at low reynolds numbers and high incidences. *Journal of Fluids and Structures*, 11(7):793–817. <https://linkinghub.elsevier.com/retrieve/pii/S0889974697901067>.
- Hoerner, S. F. (1985). *Fluid Dynamic Lift - Practical Information on Aerodynamic and Hydrodynamic Lift*. Hoerner Fluid Dynamics, second edition.
- Holladay, J., Abdullah, Z., and Heyne, J. (2020). Sustainable aviation fuel: Review of technical pathways. Technical Report DOE/EE–2041, 1660415, 8292, US Department of Energy. <https://www.osti.gov/servlets/purl/1660415/>.
- Holybro (2021). Holybro Durandal — PX4 User Guide. [https://docs.px4.io/main/en/flight\\_controller/durandal.html](https://docs.px4.io/main/en/flight_controller/durandal.html).
- Honda, M. and Yoshida, K. (2012). D-SEND project for low sonic boom design technology. In *International Congress of the Aeronautical Sciences*.
- Hummel, D. (2004). Effects of boundary layer formation on the vortical flow above slender delta wings. In *Enhancement of NATO Military Flight Vehicle Performance by Management of Interacting Boundary Layer Transition and Separation*, page 22, Prague, Czech Republic. NATO.

- Imfeld, W. F. (1974). Development program for the F-15 inlet. *J. AIRCRAFT*, page 6.
- Ito, Y. and Nakahashi, K. (2002). Unstructured hybrid grid generation based on isotropic tetrahedral grids. In *40th AIAA Aerospace Sciences Meeting & Exhibit*, Reno,NV,U.S.A. American Institute of Aeronautics and Astronautics. <http://arc.aiaa.org/doi/10.2514/6.2002-861>.
- Iwamiya, T. (2002). A computational study on unmanned scaled supersonic experimental airplane. In *32nd AIAA Fluid Dynamics Conference and Exhibit*, St. Louis, Missouri. American Institute of Aeronautics and Astronautics. <http://arc.aiaa.org/doi/10.2514/6.2002-2841>.
- Jenkinson, L., Simpkin, P., and Rhodes, D. (1999). *Civil Jet Aircraft Design*. American Institute of Aeronautics and Astronautics, Inc., Washington, DC. <https://arc.aiaa.org/doi/book/10.2514/4.473500>.
- Johnson, J. L. and Boisseau, P. C. (1953). Investigation of the low-speed stability and control characteristics of a 1/10-scale model of the convair YF-102 airplane in the langley free-flight tunnel. <https://ntrs.nasa.gov/citations/20050029408>.
- Jose Angel, D. D. L. P., Hector, P. M., Miguel, T. C., and de Lourdes, M. S. M. (2013). Microstructure characterization of low density EPS. *Applied Mechanics and Materials*, 420:167–176. <https://www.scientific.net/AMM.420.167>.
- Kalpakjian, S. and Schmid, S. R. (2009). *Manufacturing Engineering and Technology*. Pearson, sixth edition.
- Kawaguchi, J., Ninomiya, T., and Suzuki, H. (2012). Guidance and control for D-SEND#2. *International Congress of the Aeronautical Sciences*.
- Kawaguchi, J., Suzuki, H., Ninomiya, T., and Tomita, H. (2017). Post-flight evaluation of the guidance and control for D-SEND#2 2nd drop test. In *AIAA Atmospheric Flight Mechanics*



- Conference*, Grapevine, Texas. American Institute of Aeronautics and Astronautics. <https://arc.aiaa.org/doi/10.2514/6.2017-0939>.
- Kelley, W. W. and Enevoldson, E. K. (1981). Limited evaluation of an F-14A airplane utilizing an aileron-rudder interconnect control system in the landing configuration. Technical Report NASA-TM-81972, NASA, Langley Research Center. <https://ntrs.nasa.gov/api/citations/19820005275/downloads/19820005275.pdf>.
- Kobayashi, T., Simon, D. L., and Litt, J. S. (2005). Application of a constant gain extended Kalman filter for in-flight estimation of aircraft engine performance parameters. In *Volume 1: Turbo Expo 2005*, pages 617–628, Reno, Nevada, USA. ASMEDC. <https://asmedigitalcollection.asme.org/GT/proceedings/GT2005/46997/617/363558>.
- Kroo, I. (1994). Tailless aircraft design—recent experiences. In Fung, K.-Y., editor, *Symposium on Aerodynamics and Aeroacoustics*, pages 207–229, Tucson, Arizona. WORLD SCIENTIFIC. <http://www.worldscientific.com/doi/abs/10.1142/9789814534482>.
- Krüß, H. W. (2016). Criteria for crosswind variations during approach and touchdown at airports. In *54th AIAA Aerospace Sciences Meeting*, pages 167–187, San Diego, California, USA. American Institute of Aeronautics and Astronautics. [https://doi.org/10.1007/978-3-319-21127-5\\_10](https://doi.org/10.1007/978-3-319-21127-5_10).
- Langston, S. (2015). *Low-Speed Stability and Control of Exploratory Tailless Long-Range Supersonic Configurations*. PhD thesis, University of Washington.
- Langston, S., Nelson, C. P., and Livne, E. (2016). Low-speed stability and control of a reduced scale long-range supersonic configuration with reduced-size or no vertical tail. In *AIAA Atmospheric Flight Mechanics Conference*, San Diego, California, USA. American Institute of Aeronautics and Astronautics. <https://arc.aiaa.org/doi/10.2514/6.2016-1036>.

- Livne, E., Valasek, J., Starkey, R., and Strganac, T. (2017). Integrated research/education university aircraft design program development: Final report. Technical report, Defense Technical Information Center, Fort Belvoir, VA. <http://www.dtic.mil/docs/citations/AD1031586>.
- Lorinz, D. J. (1980). Flow visualization study of the F-14 fighter aircraft configuration. <https://ntrs.nasa.gov/api/citations/19800024842/downloads/19800024842.pdf>.
- Loschke, R. (2003). Development of the F-117 flight control system. In *AIAA Guidance, Navigation, and Control Conference and Exhibit*, Austin, Texas. American Institute of Aeronautics and Astronautics. <https://arc.aiaa.org/doi/10.2514/6.2003-5762>.
- Luckring, J. (2010). A survey of factors affecting blunt-leading-edge separation for swept and semi-slender wings. In *28th AIAA Applied Aerodynamics Conference*, Chicago, Illinois. American Institute of Aeronautics and Astronautics. <https://arc.aiaa.org/doi/10.2514/6.2010-4820>.
- Luckring, J. M. (2002). Reynolds number and leading-edge bluntness effects on a 65deg delta wing. In *40th AIAA Aerospace Sciences Meeting and Exhibit*, Reno, Nevada. AIAA.
- Machida, S., Yoshida, K., and Ohnuki, T. (2007). Supersonic flight testing of unmanned experimental airplane for next-generation sst. In *45th AIAA Aerospace Sciences Meeting and Exhibit*, Reno, Nevada. American Institute of Aeronautics and Astronautics. <http://arc.aiaa.org/doi/10.2514/6.2007-854>.
- Maglieri, D. J., Bobbin, P. J., Plotkin, K. J., Shepard, K. P., Coen, P. G., and Richwine, D. M. (2014). *Sonic Boom: Six Decades of Research*. NASA/SP-2014-622. NASA. <https://ntrs.nasa.gov/citations/20150006843>.
- Magn, L. and Barbosa, F. (2013). Study of unmanned supersonic aircraft configuration. In *22nd SAE Brasil International Congress and Display*, page 12, Sao Paulo, Brasil.

- Maines, B., Smith, B., Merrill, D., Saddoughi, S., and Gonzalez, H. (2009). Synthetic jet flow separation control for thin wing fighter aircraft. In *47th AIAA Aerospace Sciences Meeting Including The New Horizons Forum and Aerospace Exposition*, Orlando, Florida. American Institute of Aeronautics and Astronautics. <https://arc.aiaa.org/doi/10.2514/6.2009-885>.
- Malloy, D. J., Webb, A. T., and Kidman, D. S. (2002). F-22/f119 propulsion system ground and flight test analysis using modeling and simulation techniques. In *Volume 1: Turbo Expo 2002*, pages 1–8, Amsterdam, The Netherlands. ASMEDC. <https://asmedigitalcollection.asme.org/GT/proceedings/GT2002/36061/1/295624>.
- Matsui, N. (1996). Sensorless pm brushless dc motor drives. *IEEE Transactions on Industrial Electronics*, 43(2):300–308. <http://ieeexplore.ieee.org/document/491354/>.
- Mavriplis, N., Ting, K.-Y., Moustafa, A., Hill, C., Soltani, R., Nelson, C. P., and Livne, E. (2022). Supersonic configurations at low speeds (SCALOS): Test / simulation correlation studies. In *AIAA SCITECH 2022 Forum*, San Diego, CA & Virtual. American Institute of Aeronautics and Astronautics. <https://arc.aiaa.org/doi/10.2514/6.2022-1801>.
- McMaster, J. R. and Schenk, F. L. (1974). Development of the F-12 aircraft flight control system. *Journal of Aircraft*, 11(4):225–231. <https://arc.aiaa.org/doi/10.2514/3.59224>.
- Megson, T. H. G. (2007). *Aircraft Structures for Engineering Students*. Elsevier Aerospace Engineering Series. Butterworth-Heinemann, Oxford ; Burlington, MA, 4th ed edition.
- Mendenhall, C. A. (1983). *Delta Wings: Convair's High-Speed Planes of the Fifties & Sixties*. Motorbooks International, Osceola, Wis.
- Minato, R., Oota, T., Fukutomi, K., Tanatsugu, N., Mizobata, K., Kojima, T., and Hiroaki, K. (2007). Development of counter rotating axial fan turbojet engine for supersonic unmanned

- plane. In *43rd AIAA/ASME/SAE/ASEE Joint Propulsion Conference & Exhibit*, Cincinnati, OH. American Institute of Aeronautics and Astronautics. <http://arc.aiaa.org/doi/abs/10.2514/6.2007-5023>.
- Mitikiri, Y. and Mohseni, K. (2018). Modelling and Control of a miniature, low-aspect-ratio, fixed-delta-wing, rudderless aircraft. In *2018 AIAA Guidance, Navigation, and Control Conference*, Kissimmee, Florida. American Institute of Aeronautics and Astronautics. <https://arc.aiaa.org/doi/10.2514/6.2018-0876>.
- Mizobata, K., Minato, R., Fukiba, K., Higashino, K., and Tanatsugu, N. (2011). Development of a Small-scale Supersonic Flight Experiment Vehicle as a Flying Test Bed. In *17th AIAA International Space Planes and Hypersonic Systems and Technologies Conference*, San Francisco, California. American Institute of Aeronautics and Astronautics. <http://arc.aiaa.org/doi/10.2514/6.2011-2289>.
- Mizobata, K., Minato, R., Higuchi, K., Ueba, M., Takagi, S., Nakata, D., Higashino, K., and Tanatsugu, N. (2014). Development of a small-scale supersonic flight experiment vehicle as a flying test bed for future space transportation research. *Transactions of the Japan Society for Aeronautical and Space Sciences, Aerospace Technology Japan*, 12(ists29):Po\_3\_1–Po\_3\_10. [http://jlc.jst.go.jp/DN/JST.JSTAGE/tastj/12.Po\\_3\\_1?lang=en&from=CrossRef&type=abstract](http://jlc.jst.go.jp/DN/JST.JSTAGE/tastj/12.Po_3_1?lang=en&from=CrossRef&type=abstract).
- Mohamed, A., Massey, K., Watkins, S., and Clothier, R. (2014). The attitude control of fixed-wing MAVS in turbulent environments. *Progress in Aerospace Sciences*, 66:37–48. <https://linkinghub.elsevier.com/retrieve/pii/S0376042113000912>.
- Morelli, E. A. (2012). Flight test maneuvers for efficient aerodynamic modeling. *Journal of Aircraft*, 49(6):1857–1867. <https://arc.aiaa.org/doi/10.2514/1.C031699>.
- Mueller, T. J. and DeLaurier, J. D. (2003). Aerodynamics of small vehicles. *Annual Re-*

*view of Fluid Mechanics*, 35(1):89–111. <https://www.annualreviews.org/doi/10.1146/annurev.fluid.35.101101.161102>.

Nelson, C. P., Ting, K.-Y., Mavriplis, N., Soltani, R., and Livne, E. (2022). Supersonic configurations at low speeds (SCALOS): Project background and progress at university of washington. In *AIAA SCITECH 2022 Forum*, San Diego, CA & Virtual. American Institute of Aeronautics and Astronautics. <https://arc.aiaa.org/doi/10.2514/6.2022-1803>.

Nelson, R. C. (1998). *Flight Stability and Automatic Control*. WCB/McGraw Hill, Boston, Mass, 2nd ed edition.

Newman, B. A. and Swaim, R. L. (1986). Classical flight dynamics of a variable forward-sweep-wing aircraft. *Journal of Guidance, Control, and Dynamics*, 9(3):352–356. <https://arc.aiaa.org/doi/10.2514/3.20113>.

Ngo, T. D., Kashani, A., Imbalzano, G., Nguyen, K. T., and Hui, D. (2018). Additive manufacturing (3D printing): A review of materials, methods, applications and challenges. *Composites Part B: Engineering*, 143:172–196. <https://linkinghub.elsevier.com/retrieve/pii/S1359836817342944>.

Nicolosi, F., Ciliberti, D., Della Vecchia, P., Corcione, S., and Cusati, V. (2017). A comprehensive review of vertical tail design. *Aircraft Engineering and Aerospace Technology*, 89(4):547–557. <https://www.emerald.com/insight/content/doi/10.1108/AEAT-11-2016-0213/full/html>.

Ninomiya, T., Suzuki, H., and Kawaguchi, J. (2016). Evaluation of guidance and control system of D-SEND#2. *IFAC-PapersOnLine*, 49(17):106–111. <https://linkinghub.elsevier.com/retrieve/pii/S2405896316314914>.

Ninomiya, T., Suzuki, H., and Kawaguchi, J. (2018). Dynamic inversion controller design for balloon-launched supersonic aircraft. *Transactions of the Japan society for aeronauti-*

- cal and space sciences*, 61(6):248–257. [https://www.jstage.jst.go.jp/article/tjsass/61/6/61\\_T-17-77/\\_article](https://www.jstage.jst.go.jp/article/tjsass/61/6/61_T-17-77/_article).
- Nowak, D. K. and Solies, U. P. (2000). Wind-tunnel tests of a high lift generation and stall/spin recovery system. *Journal of Aircraft*, 37(3):383–389. <https://arc.aiaa.org/doi/10.2514/2.2637>.
- Ohnuki, T., Hirako, K., and Sakata, K. (2006). National experimental supersonic transport project. In *25th International Congress of the Aeronautical Sciences*, page 6.
- Olabisi, O. and Adewale, K., editors (2016). *Handbook of Thermoplastics*. CRC Press, Taylor & Francis Group, Boca Raton, second edition edition.
- Pantelatos, D. and Mathioulakis, D. (2004). Experimental flow study over a blunt-nosed axisymmetric body at incidence. *Journal of Fluids and Structures*, 19(8):1103–1115. <https://linkinghub.elsevier.com/retrieve/pii/S0889974604001112>.
- Pearson, H. A. and Aiken, W. S. (1944). Charts for the determination of wing torsional stiffness required for specified rolling characteristics or aileron reversal speed. Technical Report NACA-TR-799, NACA.
- Pfnur, S., Pfluger, J., and Breitsamter, C. (2020). Analysis of vortex flow phenomena on generic delta wing planforms at subsonic speeds. In Dillmann, A., Heller, G., Krämer, E., Wagner, C., Tropea, C., and Jakirlić, S., editors, *New Results in Numerical and Experimental Fluid Mechanics XII*, volume 142 of *Notes on Numerical Fluid Mechanics and Multidisciplinary Design*, pages 328–337. <http://link.springer.com/10.1007/978-3-030-25253-3>.
- Plastifab (2019). PlastiSpan 40 Insulation Material Property Data Sheet. <https://www.plastifab.com/downloads/pibs/plastifab/PIB%20248%20-%20PlastiSpan%2040%20Insulation%20Material%20Property%20Data%20Sheet-1.pdf>.

- Polhamus, E. C. (1986). Vortex lift research: Early contributions and some current challenges. In *Vortex Flow Aerodynamics, Vol. I*, NASA Langley Research Center. NASA. <https://ntrs.nasa.gov/api/citations/19860017719/downloads/19860017719.pdf>.
- Prudente, D. (2005). *Theoretical and Experimental Study of Airfoils at Low Reynolds Numbers*. Graduate Work, Instituto Tecnológico de Aeronáutica, São José dos Campos.
- Prudente, D. and Cavalieri, A. (2007). Tail and control surface sizing for uavs. In *25th AIAA Applied Aerodynamics Conference*, Miami, Florida. American Institute of Aeronautics and Astronautics. <https://arc.aiaa.org/doi/10.2514/6.2007-4557>.
- Ramian, J., Ramian, J., and Dziob, D. (2021). Thermal deformations of thermoplast during 3d printing: Warping in the case of abs. *Materials*, 14(22):7070. <https://www.mdpi.com/1996-1944/14/22/7070>.
- Raymer, D. P. (2018). *Aircraft Design: A Conceptual Approach*. AIAA Education Series. American Institute of Aeronautics and Astronautics, Inc, Reston, VA, sixth edition.
- Rech, J. and Leyman, C. S. (1997). *A Case Study by Aerospatiale and British Aerospace on the Concorde*. American Institute of Aeronautics and Astronautics, Reston, Va.
- Ribeiro, M. I. (2004). Kalman and extended Kalman filters: Concept, derivation and properties. Technical report, Technical University of Lisbon.
- Rich, B. R. (1974). F-12 series aircraft aerodynamic and thermodynamic design in retrospect. *Journal of Aircraft*, 11(7):401–406. <https://arc.aiaa.org/doi/10.2514/3.60356>.
- Rodrigue, J.-P. (2020). *The Geography of Transport Systems*. Routledge, Fifth edition. — Abingdon, Oxon ; New York, NY : Routledge, 2020., fifth edition. <https://www.taylorfrancis.com/books/9781000061468>.
- Roskam, J. (1998). *Airplane Flight Dynamics and Automatic Flight Controls: Part I*, volume 1. DARcorporation.

- Roskam, J. and Lan, C.-T. E. (1997). *Airplane Aerodynamics and Performance*. DARcorporation, Lawrence, Kansas.
- Runyan, R., Rynd, Jr., J., and Seely, J. (1992). Thrust stand design principles. In *17th Aerospace Ground Testing Conference*, Nashville, TN, U.S.A. American Institute of Aeronautics and Astronautics. <https://arc.aiaa.org/doi/10.2514/6.1992-3976>.
- Ryan, T. and Hubbard, D. (2016). 3-D printing hazards: Literature review & preliminary hazard assessment. *Professional Safety*, 61(06):56–62.
- Sakata, K. (1998). Supersonic research program in NAL, Japan. *1st CFD Workshop for Supersonic Transport Design, 1998*.
- Sakata, K. (2002). Supersonic experimental airplane (nexst) for next generation sst technology: Development and flight test plan for the unmanned scaled supersonic glider. In *40th AIAA Aerospace Sciences Meeting & Exhibit*, Reno, NV, U.S.A. American Institute of Aeronautics and Astronautics. <http://arc.aiaa.org/doi/10.2514/6.2002-527>.
- Salameh, Z. M. and Kim, B. G. (2009). Advanced lithium polymer batteries. In *2009 IEEE Power & Energy Society General Meeting*, pages 1–5, Calgary, Canada. IEEE. <http://ieeexplore.ieee.org/document/5275404/>.
- Sams, H. (1975). F-15 propulsion system design and development. In *1975 Aircraft Systems and Technology Meeting*, Los Angeles, California. AIAA.
- Schlichting, H. and Truckenbrodt, E. (1979). *Aerodynamics of the Airplane*. McGraw-Hill, New York.
- Seddon, J. and Goldsmith, E. L., editors (1999). *Intake Aerodynamics*. AIAA Education Series. American Institute of Aeronautics and Astronautics, Reston, Va, 2nd ed. / rev. by e.l. goldsmith edition.



- Selig, M. S., editor (1995). *Summary of Low Speed Airfoil Data*. SoarTech Publications, Virginia Beach, Va.
- Selig, M. S. and Guglielmo, J. J. (1997). High-lift low reynolds number airfoil design. *Journal of Aircraft*, 34(1):72–79. <https://arc.aiaa.org/doi/10.2514/2.2137>.
- Smith, R. E. (1996). Marrying airframes and engines in ground test facilities - An evolutionary revolution. *Journal of Aircraft*, 33(4):649–679. <https://arc.aiaa.org/doi/10.2514/3.47001>.
- Sobron, A., Lundström, D., and Krus, P. (2021). A review of current research in subscale flight testing and analysis of its main practical challenges. *Aerospace*, 8(3):74. <https://www.mdpi.com/2226-4310/8/3/74>.
- Specht, M. (2022). Experimental studies on the relationship between hdop and position error in the GPS system. *Metrol. Meas. Syst.*, 29(1).
- SpexDrone (2023). Skywalker X8 (Black) Fixed-Wing UAS / UAV Airframe Kit. <https://spexdrone.com/products/skywalker-x8-black-xf-1108b>.
- Stansbury, R. S., Rigby, K., Clifford, J., and Rudolph, D. (2015). An alternative UAS classification and analysis approach for integration into the national airspace system. In *AIAA Infotech @ Aerospace*, Kissimmee, Florida. American Institute of Aeronautics and Astronautics. <https://arc.aiaa.org/doi/10.2514/6.2015-1197>.
- Stenfelt, G. and Ringertz, U. (2009). Lateral stability and control of a tailless aircraft configuration. *Journal of Aircraft*, 46(6):2161–2164. <https://arc.aiaa.org/doi/10.2514/1.41092>.
- Stöcker, C., Bennett, R., Nex, F., Gerke, M., and Zevenbergen, J. (2017). Review of the current state of uav regulations. *Remote Sensing*, 9(5):459. <http://www.mdpi.com/2072-4292/9/5/459>.

- Sun, Y. and Smith, H. (2017). Review and prospect of supersonic business jet design. *Progress in Aerospace Sciences*, 90:12–38. <https://linkinghub.elsevier.com/retrieve/pii/S0376042116301002>.
- Surber, L. and Robinson, C. (1983). Survey of inlet development for supersonic aircraft. In *19th Joint Propulsion Conference*, Seattle, WA, U.S.A. American Institute of Aeronautics and Astronautics. <http://arc.aiaa.org/doi/10.2514/6.1983-1164>.
- TDK InvenSense (2021). InvenSense ICM-20689 datasheet. <https://invensense.tdk.com/wp-content/uploads/2021/03/DS-000143-ICM-20689-TYP-v1.1.pdf>.
- Tempelmeyer, K. E. and Osborne, R. S. (1955). Aerodynamic characteristics of a 0.04956-scale model of the Convair F-102A airplane at transonic speeds. <https://ntrs.nasa.gov/citations/20050029389>.
- The Boeing Company (2019). Type certificate data sheet - Boeing 737.
- Thompson, M. O. (2003). *At the Edge of Space: The X-15 Flight Program*. Smithsonian Books, Washington [D.C.].
- Ting, K.-Y., Mavriplis, N., Soltani, R., Nelson, C. P., and Livne, E. (2022). Supersonic configurations at low speeds (SCALOS): Model geometry and aerodynamic results. In *AIAA SCITECH 2022 Forum*, San Diego, CA & Virtual. American Institute of Aeronautics and Astronautics. <https://arc.aiaa.org/doi/10.2514/6.2022-1800>.
- Transport Canada (2003). Private and commercial pilot training - stall and spin awareness. Guidance Notes TP13747, 2nd edition, Transport Canada. <https://tc.canada.ca/sites/default/files/migrated/tp13747e.pdf>.
- Truckenbrodt, E. (1954). Experimentelle und theoretische Untersuchungen an symmetrisch

angeströmten Pfeil- und Deltaflügeln. *Deutsche Forschungsanstalt für Luft- und Raumfahrt e.V.*, 2:184–201.

Turbines-RC (2021). EDF Ducted Fan JP Hobby 70mm + 4-6s Motor 2250Kv (CCW). <https://www.turbines-rc.com/en/jp-hobby/1025-edf-ducted-fan-jp-hobby-70mm-4-6s-2250kv-motor-ccw.html>.

UAV Systems International (2022). Skywalker X8 Ready To Fly Drone v2.2 - Specifications. <https://uavsystemsinternational.com/products/skywalker-ready-to-fly-drone>.

Ueba, M., Kamata, T., Nakajima, S., and Maeda, Y. (2021). Verification of fully autonomous flight from takeoff to landing of a low-speed model airplane with application to a small unmanned supersonic airplane. *Transactions of the Japan Society for Aeronautical and Space Sciences, Aerospace Technology Japan*, 19(5):667–675. [https://www.jstage.jst.go.jp/article/tastj/19/5/19\\_19.667/\\_article](https://www.jstage.jst.go.jp/article/tastj/19/5/19_19.667/_article).

US Joint Chiefs of Staff (2019). Joint Air Operations - Joint Publication 3-30.

US Naval Air Command (2004). F-14D NATOPS flight manual - navy model. <https://info.publicintelligence.net/F14AAD-1.pdf>.

Walter, S. and Starkey, R. (2012a). GOJETT: A supersonic unmanned aerial flight system. In *50th AIAA Aerospace Sciences Meeting Including the New Horizons Forum and Aerospace Exposition*, Nashville, Tennessee. American Institute of Aeronautics and Astronautics. <http://arc.aiaa.org/doi/10.2514/6.2012-22>.

Walter, S. and Starkey, R. (2012b). Gojett: Design and optimization of a supersonic unmanned aerial flight system. In *12th AIAA Aviation Technology, Integration, and Operations (ATIO) Conference and 14th AIAA/ISSMO Multidisciplinary Analysis and Optimization Conference*, Indianapolis, Indiana. American Institute of Aeronautics and Astronautics. <http://arc.aiaa.org/doi/10.2514/6.2012-5531>.

- Weissman, R. (1973). Preliminary criteria for predicting departure characteristics/ spin susceptibility of fighter-type aircraft. *Journal of Aircraft*, 10(4):214–219. <https://arc.aiaa.org/doi/10.2514/3.60216>.
- Weit, C. J., Wen, J., Zaidi, T. A., and Mavris, D. N. (2021). Estimating supersonic commercial aircraft market and resulting CO2 emissions using public movement data. *CEAS Aeronautical Journal*, 12(1):191–203. <http://link.springer.com/10.1007/s13272-020-00486-3>.
- Wetzel, T. G., Simpson, R. L., and Chesnakas, C. J. (1998). Measurement of three-dimensional crossflow separation. *AIAA Journal*, 36(4). <https://arc.aiaa.org/doi/pdf/10.2514/2.429>.
- White, M. D. and Innis, R. C. (1959). A flight investigation of the low-speed handling qualities of a tailless delta-wing fighter airplane. <https://ntrs.nasa.gov/citations/19980232080>.
- Wienke, F. (2011). *Implementation of a Flight Dynamics Model and Inner Loop Control System for the GOJETT Aircraft*. PhD thesis, Technical University Munich.
- Wilson, S. J., Johansen, C. T., and Mravcak, V. (2015). Performance analysis of the atlantis intake system. In *53rd AIAA Aerospace Sciences Meeting*, Kissimmee, Florida. American Institute of Aeronautics and Astronautics. <http://arc.aiaa.org/doi/10.2514/6.2015-0639>.
- Wojnowski, W., Marć, M., Kalinowska, K., Kosmela, P., and Zabiegała, B. (2022). Emission profiles of volatiles during 3D printing with ABS, ASA, nylon, and PETG polymer filaments. *Molecules*, 27(12):3814. <https://www.mdpi.com/1420-3049/27/12/3814>.
- Yamazaki, Y., Mizobata, K., and Higashino, K. (2019). Drag reduction on the basis of the area rule of the small-scale supersonic flight experiment vehicle being developed at muroran

institute of technology. *Transactions of the japan society for aeronautical and space sciences, aerospace technology japan*, 17(2):127–133. [https://www.jstage.jst.go.jp/article/tastj/17/2/17\\_17.127/\\_article](https://www.jstage.jst.go.jp/article/tastj/17/2/17_17.127/_article).

Yates, A. H. (1952). Notes on the mean aerodynamic chord and the mean aerodynamic centre of a wing. *The Journal of the Royal Aeronautical Society*, 56(498):461–474. [https://www.cambridge.org/core/product/identifier/S0368393100129311/type/journal\\_article](https://www.cambridge.org/core/product/identifier/S0368393100129311/type/journal_article).

Yoshida, K. (2009). Supersonic drag reduction technology in the scaled supersonic experimental airplane project by JAXA. *Progress in Aerospace Sciences*, 45(4-5):124–146. <https://linkinghub.elsevier.com/retrieve/pii/S0376042109000177>.

Yoshida, K., Yoshikazu, M., and Shimbo, Y. (2002). An experimental study on unmanned scaled supersonic experimental airplane. In *32nd AIAA Fluid Dynamics Conference and Exhibit*, St. Louis, Missouri. American Institute of Aeronautics and Astronautics. <http://arc.aiaa.org/doi/10.2514/6.2002-2842>.

Zhang, T. and Barakos, G. (2020). Review on ducted fans for compound rotorcraft. *The Aeronautical Journal*, 124(1277):941–974. [https://www.cambridge.org/core/product/identifier/S0001924019001647/type/journal\\_article](https://www.cambridge.org/core/product/identifier/S0001924019001647/type/journal_article).

# Appendix A

## Launch Rail - Description & Operation

The launch rail used to accelerate MUFASA A.1 for takeoff was custom designed and built by the author for the purpose. The requirements of the rail are as follows:

- Reliably accelerate the aircraft to 22 m/s for takeoff
- Portable using a pickup truck
- Can be set-up by at most 2 people in a minimum of time
- Durable enough for repeated use over a series of launches in a single day
- Minimal cost and complexity to reduce design effort and maintain budget

Commercially-available launch rail options were explored early in the project. While effective and reliable, this option was prohibitively expensive. A custom-built option was the only option. To minimize distraction from the main project of fabricating the aircraft, the design was reduced to the simplest possible form. The portability constraint was deemed the least flexible, setting a hard limit on the packed size of the launch rail.

The completed design consists of a 6-metre-long section of strut channel with removable supports for positioning and transport. Purchased roller bearings, normally used to install a door in a

track made of strut channel, are used to permit movement of the cradle along the channel. The cradle is a custom-built aluminium carriage providing the interface between the rail and the aircraft. A Y-shaped yoke supports each end of the aircraft, with the nose yoke engaging to a hook on the airframe to accelerate and smoothly release the plane on launch. Acceleration force is provided by a twinned bungee cord approximately 23 m long and pre-tensioned with a cam-buckle strap. A hand-crank winch draws the cradle to the tensioned position. The winch is connected to the cradle through a load cell to provide tension measurements. A quick-release buckle connects the load cell to the cradle and facilitates release under tension.

Figures A.1 and A.2 show the launch cradle with the aircraft in place and with the yokes folded after takeoff, respectively. Both yokes fold under the momentum of the cradle stopping as it contacts the bump stop to allow the aircraft to take off unimpeded. Both yokes rotate on bushings with preload friction adjustable using bolt tension. Some friction is required on the front yoke to prevent the yoke rebounding on release and impacting the tail of the aircraft.

Figure A.3 shows a schematic of the launch rail configuration used for flight testing. The setup procedure is as follows:

1. Determine launch orientation and location.
2. Secure launch rail in place with ground stakes and sand bags. Install cradle followed by guide pulley/bump stop assembly.
3. With cradle at takeoff end of rail, measure 125 feet in takeoff direction and secure bungee anchor with ground stakes and sand bags.
4. Attach bungee cord to static rope and cam-lock buckle as shown in Fig. A.3. Attach pre-tensioning webbing to bungee anchor.
5. Attach launch cradle to winch as shown in Fig. A.3 Detail and turn load cell on with no tension.
6. Apply slight tension to the winch such that the cradle is not in contact with the bump stop.
7. Set bungee pre-tension to 270 N by pulling the free end of the pre-tensioning webbing

through the cam buckle.

8. Record the pre-tension value and the cradle position on the rail using the measuring tape attached to the side of the rail.
9. Crank the winch to bring the cradle to the rear of the launch rail and record tension and position as above.
10. Position the aircraft on the yokes, ensuring that the fuselage hook is engaged with the front yoke.

At this point the launch rail is ready for release. As knots tighten with use, the flight log has fields for recording both "final" and "release" tensions. Final tension is recorded after cranking the winch, and release tension is recorded immediately prior to release.

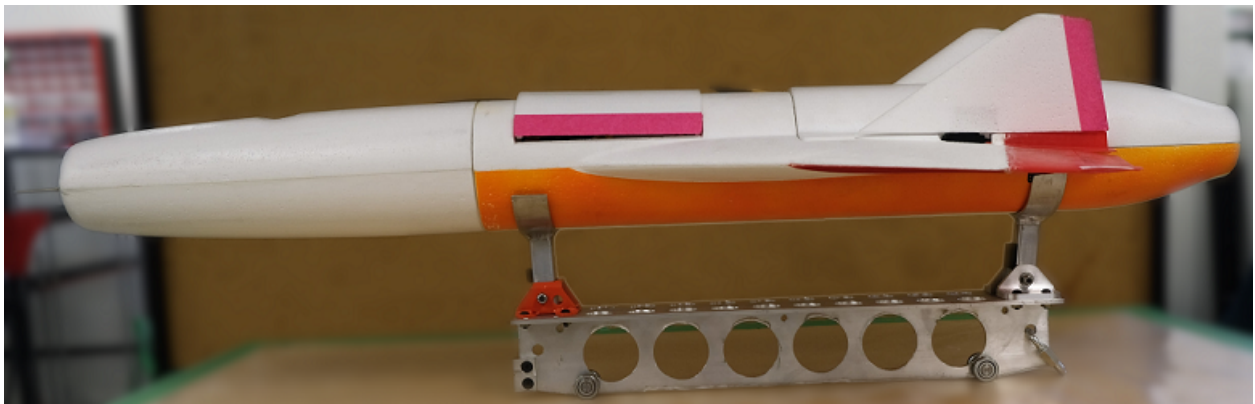


Figure A.1: Launch cradle with airframe resting on yokes. Note that the airframe hook to interface with the forward yoke is not pictured here.

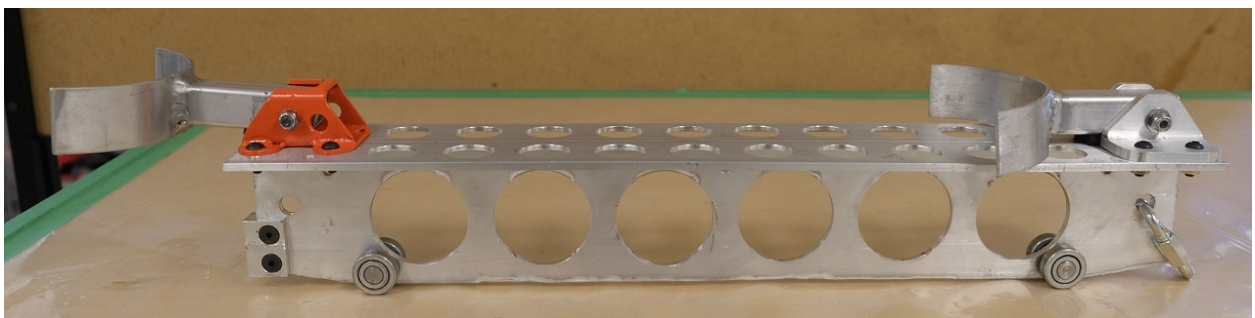


Figure A.2: Bare launch cradle with yokes folded down (after-takeoff condition).



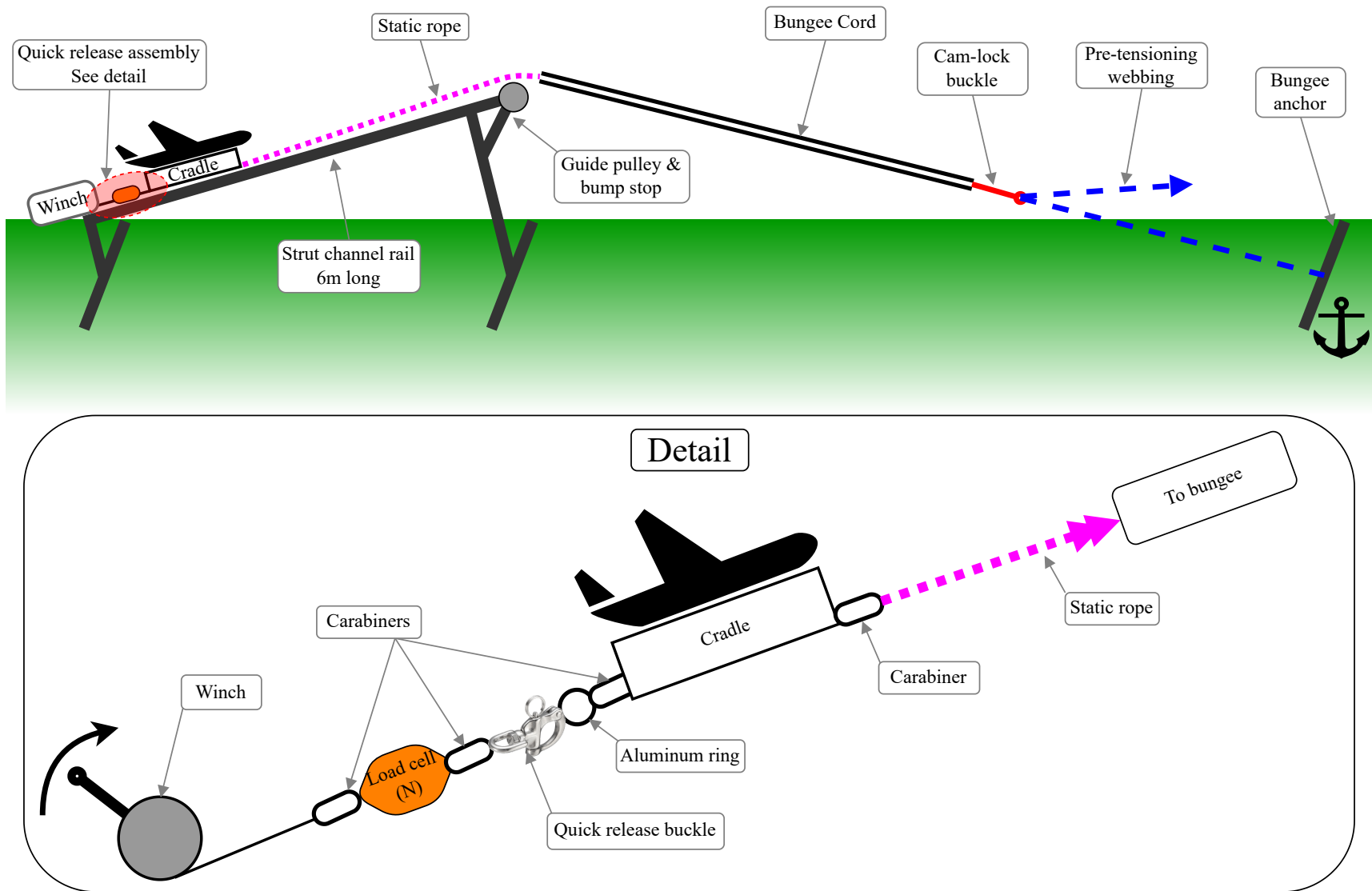


Figure A.3: Diagram of launch rail configuration.

## A.1 Validation Testing

Following fabrication, the launch rail underwent thorough validation testing. This testing proved the reliability and repeatability of the rail by successive launches of a basic analogue for the aircraft itself. A 3-inch-diameter cardboard tube with 3D printed adapters to replicate the fuselage diameter was inexpensive and suitably similar to the aircraft. An appropriate weight was placed inside the tube and secured in place to replicate the planned centre of gravity of the aircraft. Mimicking the weight, balance, and shape of the aircraft facilitated testing of the speed performance, hook interface reliability, and support yoke stability aspects of the design.

Speed performance was evaluated by the use of high-speed video recordings. A series of video frames, like those shown in Fig. A.4, recorded at a known frame rate permits speed calculations. The launch rail was painted with coloured sections 80 mm long as a reference scale. These sections are visible in Fig. A.4 as orange rectangles. The speeds measured at the takeoff-point on the launch rail were consistently calculated to be within 5% of the 21 m/s target speed using the final design of the launch rail and cradle.

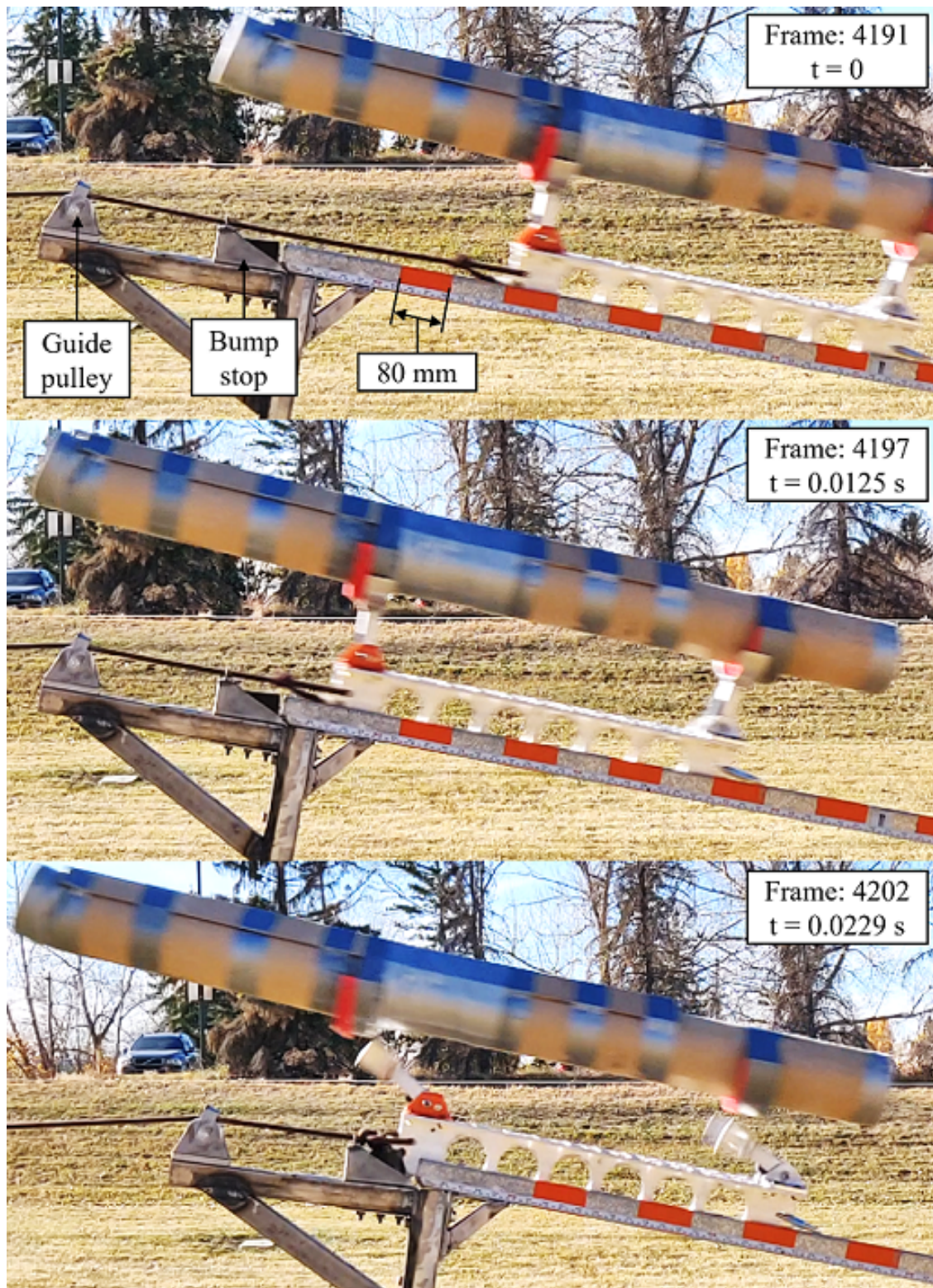


Figure A.4: Video frames from a launch rail test. Orange painted sections 80 mm long serve as a scale facilitating speed measurement using video frame rate.